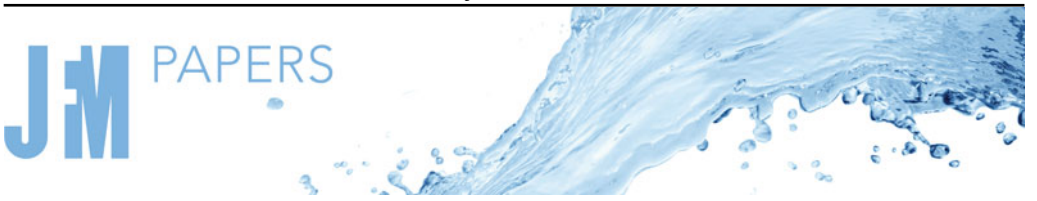
J. Fluid Mech. (2025), *vol.* 1019, A59, doi:10.1017/jfm.2025.10616



Turbulent amplification mechanism and inter-component energy transfer in strong and weak shock-wave turbulence boundary layer interaction

Xin Zhang[1], **Mingze Han**[1], **Denggao Tang**[1], **Feng Qu**[2] **and Chao Yan**[1]

[1]School of Aeronautic Science and Engineering, Beihang University, Beijing 100191, PR China

[2]School of Aeronautics, Northwestern Polytechnical University, Xi'an 710072, PR China

Corresponding author: Chao Yan, yanchao@buaa.edu.cn

(Received 29 March 2025; revised 10 July 2025; accepted 17 August 2025)

Turbulence amplification is crucial in shock-wave/turbulent boundary layer interaction (SWTBLI). To examine the impact of interaction intensity on turbulence amplification and inter-component energy transfer, direct numerical simulations of impinging oblique shock reflections at strong (37°) and weak (33.2°) incident angles are conducted. The results indicate that strong interaction generates a larger permanent separation zone, featuring the unique 'oblique platform' in Reynolds stress peaks and 'secondary turbulence amplification' downstream. Reynolds stress budget and spanwise spectral analyses reveal that $\widetilde{u''u''}$ and $-\widetilde{u''v''}$ amplify primarily by production terms. u'', v'' and w'' represent the streamwise, wall-normal and spanwise velocity fluctuations. At the investigated Reynolds number, deceleration effect dominates the initial amplification of $\widetilde{u''u''}$, influencing multi-scale wall-bounded turbulence structures, while shear effect remains active along the shear layer and may primarily affects streaky structures. The initial amplification of $-\widetilde{u''v''}$ is driven by the adverse pressure gradient, which reshapes the velocity profile and affects the wall-normal velocity. The primary energy for $\widetilde{v''v''}$ and $\widetilde{w''w''}$ amplification originates from $\widetilde{u''u''}$ via the pressure-strain term. The delayed amplification of $\widetilde{v''v''}$ is influenced by its production term and energy redistribution, with $\widetilde{w''w''}$ exhibiting higher spectral consistency with $\widetilde{u''u''}$ and receiving more energy. In strong interaction, the 'oblique platform' serves as a stable dissipation region, formed by increased separation–incident shock distance, characterised by progressively concentrated stress spectra and the transition to large-scale streaks. The downstream 'secondary amplification' process resembles the initial amplification near the separation shock foot, driven by intermittent compression waves that strengthen shear instabilities and the

© The Author(s), 2025. Published by Cambridge University Press.

https://doi.org/10.1017/jfm.2025.10616 Published online by Cambridge University Press

deceleration effect. These findings detail the streamwise stress evolution, providing a more comprehensive turbulence amplification mechanism in SWTBLI.

Key words: wave-turbulence interactions, shock waves, compressible turbulence

1. Introduction

Shock-wave/turbulent boundary layer interaction (SWTBLI) is a common phenomenon in compressible flows, first identified by Ferri in the 1940s (Gadd *et al.* 1954; Dolling 2001). Decades of research have revealed that SWTBLI occurs in many typical flow scenarios, including impinging oblique shock reflections (OSWTBLI), compression corner interactions and conical shock interactions (Gaitonde 2015; Sabnis & Babinsky 2023; Zuo & Pirozzoli 2024). In practical supersonic aircraft, SWTBLI appears in various regions, such as the external junctions between the wing and fuselage (Xiang *et al.* 2018) and the internal interactions within inlets (Wu *et al.* 2024). The SWTBLI has been extensively studied due to its complex flow structures and mechanisms, including increased pressure and temperature, flow separation, shock-wave unsteadiness, separation bubble dynamics, detached shear layer/mixing layer instabilities and the amplification and evolution of turbulence (Babinsky & Harvey 2011). These phenomena are intricately coupled rather than occurring independently. Consequently, SWTBLI significantly impacts aerodynamic efficiency (Longo 2003), introduces challenges related to low-frequency shock motion and high structural loads (Délery & Dussauge 2009) and necessitates enhanced thermal protection technology (Hung, Greenschlag & Scottoline 1977) for transonic and supersonic aircraft design. The intricate flow phenomena associated with SWTBLI have driven extensive exploration of its physical mechanisms. A deeper understanding of SWTBLI can facilitate the development of active and passive control strategies to improve aerodynamic performance (Dolling 2001; Gaitonde 2015; Huang *et al.* 2020; Sabnis & Babinsky 2023).

Turbulence amplification is a significant flow phenomenon in SWTBLI. The interaction between shock waves and turbulent boundary layers is often accompanied by a strong adverse pressure gradient (APG), which can lead to either intermittent or permanent flow separation, depending on its intensity. Separation bubbles can induce flow deflection, with a reflected separation shock typically forming upstream of the separation zone and a reattachment shock appearing downstream in cases of strong interaction. Turbulence amplification often originates near the separation shock foot, where a gradually rising shear layer (also referred to as the mixing layer) develops. In both the interaction region and downstream, the local turbulence peak generally coincides with the height of the shear layer. Thus, turbulence amplification is likely influenced by the low-frequency motion of the shock and separation bubble (Smits & Muck 1987), the instability of shear/mixing layers (Selig *et al.* 1989), the curvature effects caused by concave streamlines (Andreopoulos, Agui & Briassulis 2000), direct inviscid amplification (Smits & Muck 1987) or a combination of these mechanisms.

To investigate the key mechanisms driving turbulence amplification in SWTBLI, Smits & Muck (1987) conducted experiments on compression corners with varying intensities at three angles under Mach 2.9. They concluded that, in weak interactions, turbulence amplification is primarily driven by direct inviscid amplification, with potential contributions from APG, concave curvature and compressive strain rates. In strong interactions, however, the unsteady motion of the shock became the dominant factor. Adams (1998) was the first to apply direct numerical simulations (DNS) to compression corner interactions, confirming similar amplification rates to those observed by Smits &

https://doi.org/10.1017/jfm.2025.10616 Published online by Cambridge University Press

Muck (1987) in subsequent research, despite using lower Reynolds numbers. Their analysis further revealed that pressure dilatation played a minor role, limited to a small region near the shock foot, thus excluding compressibility effects (Adams 2000). Pirozzoli & Grasso (2006) conducted the first DNS study of OSWTBLI with mild separation at a free-stream Mach number of 2.3 and an incident shock angle of 33.2°. The streamline deflection in this case is extremely slight, reducing the influence of curvature effects. Their study found that while turbulent kinetic energy (TKE) and shear stress amplification exhibited distinct behaviours, both peaked within the detached shear layer, suggesting that turbulence amplification may be primarily related to shear layer formation. Moreover, vortex structures propagating downstream within the shear layer were found to generate large-scale, low-frequency unsteadiness. The numerical set-up from Pirozzoli & Grasso (2006) has since become a reference for many subsequent OSWTBLI studies (Aubard, Gloerfelt & Robinet 2013; Tong *et al.* 2022*c*).

Priebe, Wu & Martín (2009) compared DNS results for OSWTBLI at Mach 2.9 with those for compression corner interactions under similar flow conditions and shock intensities from Wu & Martin (2007). They observed that turbulence amplification was weaker in OSWTBLI due to the absence of significant streamline deflection, confirming the role of curvature effects in turbulence amplification. This also demonstrated that OSWTBLI can mitigate curvature influences, providing a better framework for exploring other mechanisms influencing turbulence amplification. Furthermore, they observed turbulence peaks far from the wall, aligning with the mean sonic line. Similarly, Pirozzoli, Bernardini & Grasso (2010) found in transonic flow that turbulence amplification was consistent with the midline of the shear layer, although streamwise Reynolds stress amplification was weaker than other components, reducing turbulence anisotropy. Expanding on this, Pirozzoli & Bernardini (2011*a*) decomposed the TKE budget in the interaction zone and identified that the TKE production term also peaked at the midline of the shear layer. Experimental studies further supported these findings. Dupont *et al.* (2008) employed particle image velocimetry to analyse OSWTBLI at Mach 2.3, revealing that turbulence amplification originated near the wall downstream of the reflected shock foot. They identified Kelvin–Helmholtz (K–H) instability through reverse flow and inflectional velocity profiles, which led to the emergence of large-scale convective vortices. Subsequent research by Dupont, Piponniau & Dussauge (2019) showed that the spatial growth rates of the shear layer in OSWTBLI at two different deflection angles matched those of a typical mixing layer, with this consistency persisting at higher Mach numbers (Helm, Martín & Williams 2021). These studies highlight the critical role of shear effects in turbulence amplification.

Fang *et al.* (2020) extended the DNS simulation of Pirozzoli & Grasso (2006) with mild separation and found that turbulence amplification begins at the separation shock foot, where the detached free shear layer has not yet fully developed. A detailed decomposition of the TKE production term revealed that, while the peak production associated with mean shear remained strongly correlated with the shear layer, the continuous deceleration effect induced by the compression waves at the separation shock foot played a more dominant role in turbulence amplification upstream of the incident shock. This conclusion, which emphasises the role of deceleration in the initial stages of turbulence amplification, was further validated by Shi & Yan (2023) and Kang & Lee (2024) in compression corners.

Recent studies have also explored the impact of Reynolds number on turbulence amplification. At high Reynolds numbers, shocks penetrate deeper into the boundary layer, generating larger-amplitude pressure fluctuations within the interaction region (Dolling & Murphy 1983). In contrast, at low Reynolds numbers, shocks are more diffuse and farther from the wall, reducing the peak of pressure fluctuations but increasing the intermittency

https://doi.org/10.1017/jfm.2025.10616 Published online by Cambridge University Press

of wall pressure signals, which leads to larger separation zones (Ringuette, Wu & Martín 2008). Building on low Reynolds number research such as Fang *et al.* (2020), Laguarda *et al.* (2024) employed large-eddy simulations to study OSWTBLI at higher Reynolds numbers. Their findings revealed that, at high Reynolds numbers, the TKE peak shifted further downstream of the separation shock foot and farther from the wall. This behaviour was attributed to enhanced streamwise pressure transport, which was caused by the stronger influence of the reflected shock motion on the wall at high Reynolds numbers.

The leading factors driving turbulence amplification, whether involving streamwise-normal stress through deceleration or pressure transport, or shear stress influenced by shear effects and K–H instability, primarily affect individual stress components in the initial stage. Therefore, the subsequent energy transfer between these components requires further exploration. Investigating this inter-component energy transfer is crucial for understanding self-sustaining cycles in turbulence (Gungor, Maciel & Gungor 2022), which are closely related to turbulence production and pressure strain (Panton 2001; Cho, Hwang & Choi 2018). Consequently, self-sustaining mechanisms play a critical role in the production and evolution of turbulence. Fully developed wall-bounded turbulent boundary layers (TBL) exhibit abundant hairpin vortices (Robinson 1991) and streaky velocity structures, first identified by Kline & Runstadler (1959), with an inner-scaled spanwise wavelength (λ_z^+) of approximately 100 (Kline *et al.* 1967). In the near-wall region, turbulent structures are characterised by small-scale features. The self-sustaining mechanism here involves streamwise vortices forming due to streak breakdown, which then generate streaks through momentum advection (Hamilton, Kim & Waleffe 1995; Schoppa & Hussain 2002; Lee & Moser 2019). Subsequently, larger-scale streaks have also been observed in the logarithmic and outer layers, leading to a more comprehensive self-sustaining mechanism (Hwang & Cossu 2010, 2011). Therefore, streak instability is one of the important mechanisms in self-sustaining cycles (Jiménez & Pinelli 1999; Panton 2001) and is also related to turbulence production (Kim, Kline & Reynolds 1971).

However, under APG conditions, streak intensity weakens (Skote & Henningson 2002), their spacing becomes irregular and increases by over four times compared with the zero pressure gradient (ZPG) case (Lee & Sung 2009). In separation zones, streaks may completely disappear (Rahgozar & Maciel 2012). These differences in flow states lead to distinct self-sustaining mechanisms under APG, such as the inflectional instability in near-separated flows discovered by Elsberry *et al.* (2000). Furthermore, APG alters energy transfer between stress components. By comparing the production and pressure-strain spectra of stress components under APG and ZPG conditions, Gungor *et al.* (2022) found that, in large-defect APG cases, spectral peaks shifted farther from the wall and appeared at larger scales. reflecting the enhanced dominance of turbulent activity in the outer layer as the velocity defect increases.

The SWTBLI problem also involves pronounced APG effects. Tong *et al.* (2017) conducted DNS simulations of compression corners with varying turning angles, revealing that, for small turning angles, TKE budgets resembled those of canonical wall turbulence. However, for larger turning angles, a strong turbulence transport term emerged in the outer layer, coupled with the destruction of streak structures, likely caused by the shear layer above the separation bubble altering the transport mechanism. Similarly, Fang *et al.* (2020) observed that, during the initial turbulence amplification stage, elongated streaks, streamwise vortices and Reynolds stress anisotropy remained well preserved. However, after the shear layer detached, although near-wall streaks vanished, streaky structures persisted along the shear layer and increased in scale with the appearance of large-scale vortices. Through spectral analysis of normal stress components in OSWTBLI, Yu *et al.* (2022) demonstrated that APG-induced increases in streamwise velocity

https://doi.org/10.1017/jfm.2025.10616 Published online by Cambridge University Press

fluctuations contribute to the formation of large-scale streaks. Similar to the self-sustaining mechanism in canonical turbulence, these amplified velocity fluctuations transfer energy to other components via the pressure-strain term, leading to the development of large-scale streamwise vortices downstream of the streaks.

Previous research on turbulence amplification mechanisms and energy transfer between stress components has primarily focused on cases with mild separation. However, in stronger SWTBLI, larger-scale permanent separation zones often emerge, accompanied by more pronounced shock oscillations. Additionally, a secondary turbulence amplification occurs near the reattachment region, as observed by Pasquariello, Hickel & Adams (2017) for OSWTBLI at high Mach numbers and Kang & Lee (2024) for compression corners with large turning angles. To further explore energy transfer between stress components, identify the factors influencing the differences in amplification order of these components and compare turbulence amplification mechanisms in strong and weak OSWTBLI, this study conducts DNS simulations for two distinct incident angles.

The remaining contents of this study are organised as follows: § 2 introduces the DNS algorithm, computational configurations for both strong and weak interactions and validation of simulation accuracy. Section 3 compares the averaged results of strong and weak interactions, highlighting the formation of a permanent, larger-scale separation zone in the strong interaction. Additionally, the streamwise evolution of the stress component peaks in strong interactions reveals unique turbulence amplification features, including the 'slope platform' region and the 'secondary amplification' phenomenon. The mechanisms responsible for these differences are discussed in § 4 through stress budget decomposition, and the dominant terms and amplification factors of each component are also identified. Section 5 explores inter-component energy transfer from a spectral perspective, discussing the distinct influences of deceleration and shear effects on mean energy and scale range. The relationship between the formation of consistent large-scale streaks and the 'slope platform' region is also investigated. Finally, a more complete turbulence amplification mechanism and key conclusions are summarised in § 6.

2. Numerical set-up

This section outlines the numerical methods and DNS simulation configurations for SWTBLI, along with a validation of the simulation accuracy.

2.1. *Governing equations and calculation schemes*

The numerical simulations are based on the three-dimensional Navier–Stokes equations, non-dimensionalised using free-stream variables, as expressed in (2.1)

$$\frac{\partial Q}{\partial t}+\frac{\partial f_c}{\partial x}+\frac{\partial g_c}{\partial y}+\frac{\partial h_c}{\partial z}-\frac{1}{Re_\infty}\left(\frac{\partial f_v}{\partial x}+\frac{\partial g_v}{\partial y}+\frac{\partial h_v}{\partial z}\right)=0, \tag{2.1}$$

among them, the convective and viscous fluxes in the x-direction can be expressed as (2.2)

$$f_c=\begin{pmatrix}\rho u\\ \rho uu+p\\ \rho uv\\ \rho uw\\ (\rho e+p)u\end{pmatrix},\quad f_v=\begin{pmatrix}0\\ \tau_{11}\\ \tau_{12}\\ \tau_{13}\\ u\tau_{11}+v\tau_{12}+w\tau_{13}-q_1\end{pmatrix}, \tag{2.2}$$

https://doi.org/10.1017/jfm.2025.10616 Published online by Cambridge University Press

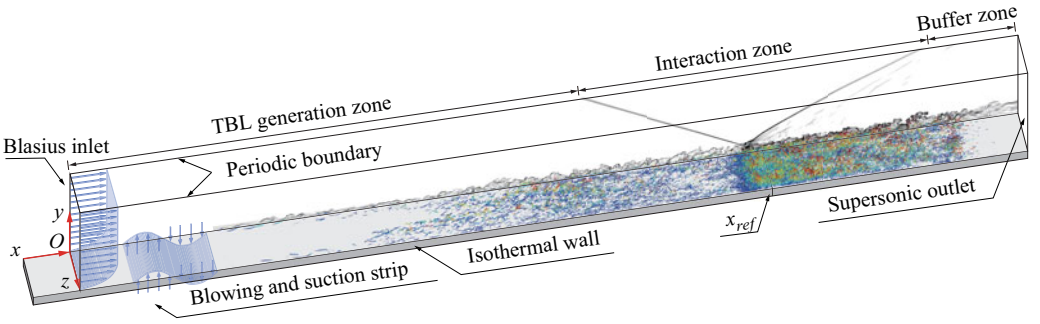


Figure 1. Schematic of computational domain and boundary conditions for SWTBLI simulations. The iso-surface is the second invariant of velocity gradient $Q = 10$ and coloured by the wall-normal height.

where

$$\tau_{ij} = \mu\left(\frac{\partial u_i}{\partial x_j} + \frac{\partial u_j}{\partial x_i}\right) - \frac{2}{3}\mu\frac{\partial u_k}{\partial x_k}\delta_{ij}, \quad q_i = -\frac{\mu}{(\gamma-1)Re_\infty Ma_\infty^2 Pr}\frac{\partial T}{\partial x_i},$$

$$e = \frac{T}{\gamma(\gamma-1)Ma_\infty^2} + \frac{u^2+v^2+w^2}{2}, \quad p = \frac{\rho T}{\gamma Ma_\infty^2}, \quad \mu = \frac{1+T_s/T_\infty}{T+T_s/T_\infty}T^{3/2}. \tag{2.3}$$

Variables in (2.1)–(2.3) with the subscript '∞' denote free-stream values, while those without subscripts, such as densityρ, streamwise velocity u, wall-normal velocity v, spanwise velocity w, pressure p and temperature T are dimensionless quantities obtained by normalisation with free-stream parameters. Moreover, γ is the specific heat capacity ratio, δ_{ij} represents the Kronecker δ, and Ma, Re, Pr denote the Mach number, Reynolds number and Prandtl number, respectively.

This study employs the open-source finite-difference DNS solver, OpenCFD-SC2.0, developed by Li *et al.* (2008, 2010), which is tailored for structured three-dimensional curvilinear grids. Known for its ease of deployment and clear program structure, the solver has demonstrated high computational accuracy and robustness across various benchmarks, including OSWTBLI (Tong *et al.* 2022*b*,*c*), compression corners (Zhu *et al.* 2016; Tong *et al.* 2017) and supersonic plate turbulent boundary layers (Liang & Li 2013; Tong *et al.* 2022*a*). For numerical discretisation, convective fluxes are split using the local Lax–Friedrichs method and reconstructed with the high-order TENO6-SA scheme (Zhang *et al.* 2024), which incorporates the piecewise spectral optimisation method to achieve a broader resolved bandwidth with equivalent accuracy and grid resolution. This provides potential advantages for simulating multi-scale turbulence. Viscous fluxes are discretised using the sixth-order central difference scheme, while time integration is performed with the classic third-order Runge–Kutta method.

2.2. *Simulation conditions and configurations*

The computational domain for simulating the OSWTBLI problem, as illustrated in figure 1, has sizes of $[L_x \times L_y \times L_z] = [100 \times 10 \times 4]$ mm. The front boundary at $x = 0$ mm is defined as a laminar boundary layer inlet with $Ma_\infty = 2.25$, derived from the Blasius solution at a distance of 127 mm from the leading edge of the plate. Detailed free-stream parameters are listed in table 1. The rear boundary is a supersonic outlet, while the side boundaries are periodic. The bottom boundary is an isothermal wall with $T_w = 1.9T_\infty$, closely approximating the temperature of an adiabatic wall under the

https://doi.org/10.1017/jfm.2025.10616 Published online by Cambridge University Press

Ma_∞	Re_∞ (mm^{-1})	T_∞ (K)	Pr	γ	R (J kg^{-1} K^{-1})
2.25	2.5×10^4	169.44	0.72	1.4	287

Table 1. Free-stream conditions: Mach number, unit Reynolds number, temperature, Prandtl number, specific heat capacity ratio and specific gas constant.

current flow conditions. The subscript w denotes the variable at the wall. To generate a canonical turbulent boundary layer (TBL), this study adopts the transition-inducing method based on blowing and suction, as referenced in Pirozzoli, Grasso & Gatski (2004). A synthetic jet band is implemented at $x = x_a \sim x_b = 7.5 \sim 20.2$ mm from the leading edge, with wall-normal velocity disturbances determined by (2.4)

$$\begin{aligned} v(x, y=0, z, t) &= A f(x) g(z) h(t), \quad x_a \leqslant x \leqslant x_b \\ f(x) &= \frac{4}{\sqrt{27}} \sin(\theta)[1 - \cos(\theta)], \quad \theta = 2\pi \frac{x - x_a}{x_b - x_a} \\ g(z) &= \sum_{l=1}^{l_{max}} \frac{0.8^{l-1}}{g_0} \sin\left(2\pi l \frac{z}{L_z} + \phi_l\right), \quad g_0 = \sum_{l=1}^{l_{max}} 0.8^{l-1} \\ h(t) &= \sum_{m=1}^{m_{max}} \frac{0.8^{m-1}}{h_0} \sin(m\beta t + \phi_m), \quad h_0 = \sum_{m=1}^{m_{max}} 0.8^{m-1}. \end{aligned} \tag{2.4}$$

Here, l_{max} and m_{max} are set to 10 and 5, respectively, while ϕ_l and ϕ_m are random numbers in the range $[0, 2\pi]$. The amplitude A is assigned a larger value of 0.1 to accelerate transition. Under these settings, canonical turbulent structures fully develop at $x > 55$ mm after approximately 100 dimensionless time units. Consequently, this study selects $x = x_{ref} = 70$ mm as the nominal shock impingement point and reference station. For simplicity, the dimensionless coordinates $[x_0 \times y_0 \times z_0]$ are defined as $[(x - x_{ref}) \times y \times z]$/mm. Other flow variables are non-dimensionalised using the boundary layer thickness δ_0, friction velocity u_τ, wall kinematic viscosity ν_w and wall density ρ_w at x_{ref}, facilitating their representation in either outer or inner scales. To examine variations in SWTBLI with different interaction intensities, two incident shock angles are considered. For the weak interaction, the incident shock angle is set to 33.2°, which corresponds to a classic OSWTBLI simulation that has been extensively analysed. For the strong interaction, the incident shock angle is increased to 37°. As shown in figure 1, the incident shock and the reflected separation shock divide the upper boundary into three regions. The boundary conditions for these regions significantly influence the shock position and intensity. The regions upstream of the incident shock and downstream of the reflected shock are set as penetrating boundary conditions, consistent with the standard turbulent boundary layer simulations without an incident shock. In the intermediate region, post-shock conditions are precisely specified based on the oblique shock relations for the two incident angles, allowing the flow to adaptively generate the correct shock pattern.

All simulations employed a consistent grid resolution of $[3500 \times 300 \times 350]$, with finer grids allocated to the interaction zone for improved accuracy. Specifically, in the streamwise direction, 900 progressively refined grids cover the turbulent boundary layer generation region ($x = 0{-}55$ mm), 2500 uniform grids are utilised in the interaction region ($x = 55{-}85$ mm) and 100 progressively coarser grids are applied in the downstream buffer zone ($x = 85{-}100$ mm). The transitions between these regions are uniformly smoothed to avoid discontinuities. Additionally, wall-normal grids are arranged based on (2.5), with

https://doi.org/10.1017/jfm.2025.10616 Published online by Cambridge University Press

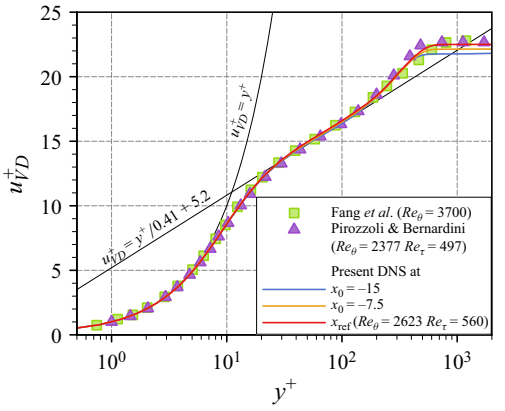


Figure 2. Comparison of the van Driest transformed mean velocity u^+_{VD} profiles at different streamwise stations and similar simulations (Fang *et al.* 2020; Pirozzoli & Bernardini 2011*b*).

more points concentrated near the wall to capture boundary layer structures

$$y_j = L_y \left\{ 1 - \frac{\tanh\left[\kappa(1 - j/N_y)\right]}{\tanh \kappa} \right\}, \quad j = 0, 1, \cdots, N_y, \quad \kappa = 3. \tag{2.5}$$

Spanwise grids are uniformly distributed. Under these configurations, the grid scales within the interaction region reach $[\Delta x^+ \times \Delta y^+_w \times \Delta z^+] = [4.65 \times 0.39 \times 4.43]$, which are comparable to those in recent DNS studies (Bernardini *et al.* 2023; Yu *et al.* 2023). The superscript $+$ denotes a variable normalised in wall units.

2.3. *Validation*

To verify the accuracy of the simulation results, figure 2 presents the van Driest transformed velocity (u_{VD}) at different streamwise stations, measured after turbulence has fully developed and in the absence of the incident oblique shock, as defined in (2.6)

$$u^+_{VD} = \frac{1}{u_\tau} \int_0^{\overline{u}} \sqrt{\frac{\overline{\rho}}{\overline{\rho}_w}} \mathrm{d}\overline{u}. \tag{2.6}$$

In this study, $-$ and $\sim$ represent the Reynolds average and Favre (density-weighted) average, respectively. The corresponding fluctuation variables are denoted as $'$ and $''$, respectively. Unless otherwise specified, all mean results in this study are averaged over both time and the spanwise direction.

The calculated profiles in figure 2 clearly conform to the classical law of the wall in the viscous sublayer ($y^+ < 5$) and logarithmic region ($30 < y^+ < 100$) and exhibit excellent agreement with recent DNS simulations under similar flow conditions (Fang *et al.* 2020; Pirozzoli & Bernardini 2011*b*), confirming that the flow has transitioned into fully developed turbulence for $x_0 \geqslant -15$. In addition, the density-scaled Reynolds stress components, $(\overline{\rho}/\overline{\rho}_w)\widetilde{u''u''}$, $(\overline{\rho}/\overline{\rho}_w)\widetilde{v''v''}$, $(\overline{\rho}/\overline{\rho}_w)\widetilde{w''w''}$ and $(\overline{\rho}/\overline{\rho}_w)\widetilde{u''v''}$ at the reference station are compared with the incompressible DNS data by Wu & Moin (2010), and the results are shown in figure 3(*a*). These results also demonstrate satisfactory consistency, verifying the correctness of the simulation results.

The spanwise two-point correlations of velocity fluctuations at various heights at x_{ref} are presented in (2.7). The two-point correlation for velocity fluctuation u'_i is defined as

https://doi.org/10.1017/jfm.2025.10616 Published online by Cambridge University Press

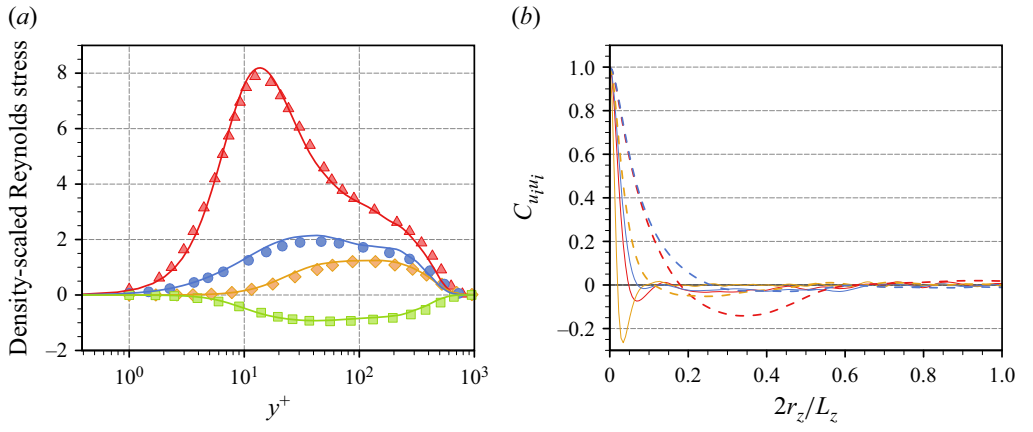


Figure 3. (*a*) Density-scaled Reynolds stresses: $(\overline{\rho}/\overline{\rho}_w)\widetilde{u''u''}$ (—), $(\overline{\rho}/\overline{\rho}_w)\widetilde{v''v''}$ (—), $(\overline{\rho}/\overline{\rho}_w)\widetilde{w''w''}$ (—) and $(\overline{\rho}/\overline{\rho}_w)\widetilde{u''v''}$ (—). Lines are present results at x_{ref}, symbols are incompressible DNS results from Wu & Moin (2010). (*b*) Spanwise two-point correlations: C_{uu} (- - -), C_{vv} (- - -), C_{ww} (- - -). The results at $y^+ = 10$ and 100 are denoted as thin solid and thick dashed lines, respectively.

follows:

$$C_{u_iu_i}(x, y, r_z) = \frac{\overline{u_i'(x, y, z)u_i'(x, y, z + r_z)}}{\overline{u_i'(x, y, z)u_i'(x, y, z)}}, \quad r_z \in [0, L_z/2]. \tag{2.7}$$

Figure 3(*b*) illustrates that all two-point correlations decrease as the spanwise interval increases, with slower decay at higher wall-normal heights. Nevertheless, as the spanwise interval r_z approaches $L_z/2$, all correlations approach zero, confirming that the spanwise domain length designed in this study is sufficient and appropriate.

3. Flow structures and turbulence amplification differences in strong and weak interactions

Following the validation of the numerical algorithm, this section compares the flow structures and turbulence amplification processes in strong and weak interactions using averaged flow fields.

3.1. *Time-averaged flow field and separation scale comparison*

For a free-stream Mach number of approximately 2.25, an oblique shock with a 33.2° incident angle generates a mild and intermittent separation bubble. This computational set-up is a classical benchmark for studying OSWTBLI, first analysed via DNS by Pirozzoli & Grasso (2006) and later reproduced in numerous numerical studies (Fang *et al.* 2020; Tong *et al.* 2022*b*,*c*). To further explore the impact of phenomena such as larger-scale separation bubbles and increased unsteadiness associated with stronger incident shocks on the turbulence amplification mechanisms in SWTBLI, this study introduces a stronger oblique shock with an incident angle of $\beta = 37°$. Figure 4 presents the mean wall skin-friction coefficient (C_f) and the mean wall pressure coefficient (C_p) for the two incident angles, as defined in (3.1)

$$C_f = \frac{2\,(\mu\partial\overline{u}/\partial y)_w}{\rho_\infty u_\infty^2}, \quad C_p = \frac{\overline{p}_w}{p_\infty}. \tag{3.1}$$

https://doi.org/10.1017/jfm.2025.10616 Published online by Cambridge University Press

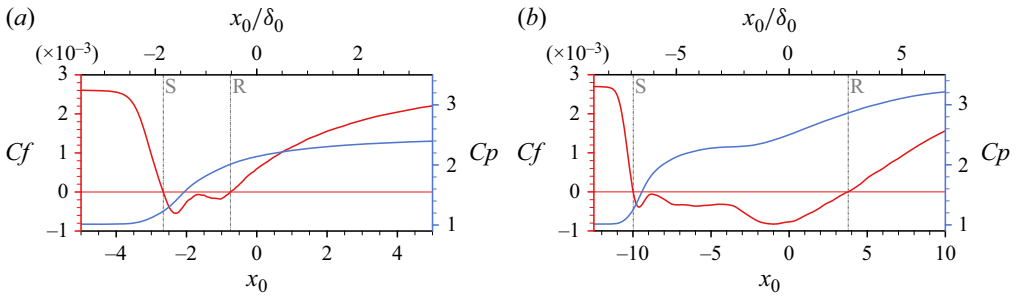


Figure 4. Streamwise distributions of mean wall skin-friction coefficient (C_f) and the mean wall pressure coefficient (C_p) under weak (a) and strong (b) interactions.

Although variations in computational conditions, such as the boundary layer thickness at the nominal impingement location, Reynolds number (Laguarda *et al.* 2024) and the wall-to-recovery temperature ratio (Bernardini *et al.* 2016), may lead to differences in C_f, the overall shape of the C_f curve for weak interaction shown in figure 4(a) remains similar to the results from Vyas, Yoder & Gaitonde (2019) and Fang *et al.* (2020). It exhibits a distinctive 'W'-shaped profile in the separation zone, a trend likely influenced by the behaviour observed at lower Reynolds numbers, as reported in Laguarda *et al.* (2024).

Comparing the C_f curves for strong and weak interactions reveals distinct differences. In the weak interaction case, the separation zone is smaller, and the maximum negative C_f occurs downstream of the separation point (S). In contrast, the strong interaction exhibits an enlarged separation zone and a deformed 'W'-shaped C_f. While the first half of the 'W' remains similar to that in the weak interaction, the second half is significantly extended. Additionally, a C_f plateau emerges in the region $x_0 \approx -7.5$ to -3.7, with the maximum negative C_f appearing further downstream, closer to the reattachment point (R). Some characteristics of C_f in strong interaction are consistent with the $Ma_\infty = 2.0$, $\beta = 40°$ case at low Reynolds numbers in Laguarda *et al.* (2024) and the $Ma_\infty = 2.3$, $\beta = 36.9\,°$ case in Gross, Little & Fasel (2022). Moreover, in the strong interaction, C_p exhibits a plateau near the region where the C_f plateau occurs, suggesting the presence of large-scale separation bubbles and the formation of reattachment compression waves. Conversely, under weak interaction, C_p increases smoothly in the streamwise direction near the reference station.

To provide a clearer comparison of the differences in separation bubbles between strong and weak interactions, figure 5 presents the numerical schlieren visualised using the mean density gradient magnitude in the interaction regions, along with the sonic line and the mean streamline near the separation zone.

The numerical schlieren in figure 5 clearly indicate that the primary flow structures in both cases share common features, including the incident shock, reflected separation shock, expansion waves behind the incident shock foot and the detached free shear layer originating from the separation shock foot. However, notable differences arise due to variations in the separation bubble characteristics. The C_f and C_p curves in figure 4 imply that a complete separation bubble forms under strong interaction, with a streamwise length of approximately 12 mm and a wall-normal height of around 1.4 mm. In contrast, the separation bubble in the weak interaction case is significantly less distinct. The local zoomed-in view reveals that its streamwise length is approximately 1.8 mm, while its wall-normal height is much smaller, measuring around 0.036 mm.

Regardless of the separation bubble size, the deceleration and upward deflection of the mean flow at the initial separation stage remain generally consistent. Consequently, the compression waves tend to converge around $y_0 = 1$, forming the separation shock in both

https://doi.org/10.1017/jfm.2025.10616 Published online by Cambridge University Press

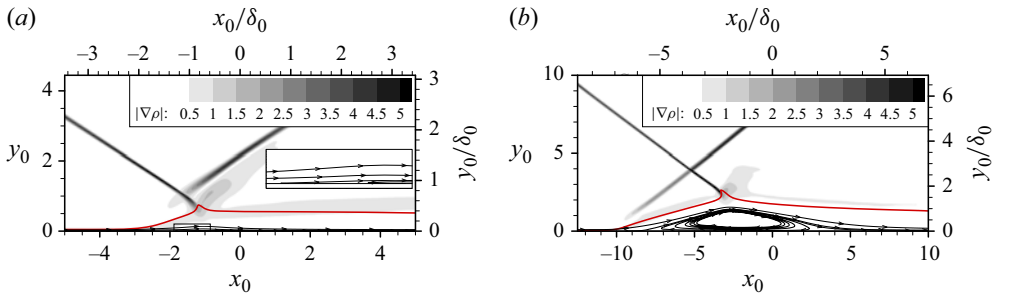


Figure 5. Contours of mean density gradient magnitude fields under weak (*a*) and strong (*b*) interactions together with sonic line (— line).

cases. In addition, the incident shock foot is typically positioned above the top of the separation bubble, while the separation shock foot is located upstream of the separation point. A larger separation bubble, as displayed in the strong interaction case, significantly increases the height of the incident shock foot and extends the distance between the foot of the separation and the incident shocks. This explains the phenomenon observed in figure 5, where the separation shock in strong interaction forms further upstream of the shock intersection point, whereas in weak interaction, the separation shock is generated closer to the intersection point.

Furthermore, the larger separation zone observed in the strong interaction indicates the presence of a more extensive subsonic region. Although the overall shape of the sonic line is similar at both incident angles, its position in strong interaction is significantly elevated, further confirming the existence of a larger subsonic region. A comparison between the schlieren contour and the sonic line reveals that the position of the detached free shear layer, as indicated by the density gradient magnitude, aligns well with the sonic line in both interactions. However, notable differences emerge downstream of the interaction region. Under weak interaction, the height of the free shear layer steadily increases, while under strong interaction, its height gradually decreases. The impact of these differences in the mean flow field on turbulence amplification will be discussed comprehensively in subsequent sections.

3.2. *Amplification process of turbulence kinetic energy and Reynolds stresses*

The previous subsection highlighted significant differences in the scale and shape of the separation bubble under strong and weak interactions, as observed through numerical schlieren, C_f, and C_p plots. These variations are expected to influence the TKE amplification mechanism, necessitating further exploration. To this end, figure 6 presents the mean TKE contours for different incident angles, accompanied by the zero-velocity streamline and dividing streamline to clearly indicate the separation bubble boundaries. The definition of TKE is provided in (3.2)

$$\mathrm{TKE} = K = \frac{1}{2}\left(\widetilde{u''u''} + \widetilde{v''v''} + \widetilde{w''w''}\right). \tag{3.2}$$

As shown in figure 6, the TKE peak reaches its maximum near the separation shock foot in both cases, with weaker amplification observed downstream of the incident shock foot. According to Fang *et al.* (2020), downstream TKE amplification is predominantly influenced by shear effects, whereas upstream amplification, though also affected by shear, is primarily governed by stronger flow deceleration. Differences in separation bubble structures lead to distinct TKE distribution patterns. Figure 6 indicates that the amplified

https://doi.org/10.1017/jfm.2025.10616 Published online by Cambridge University Press

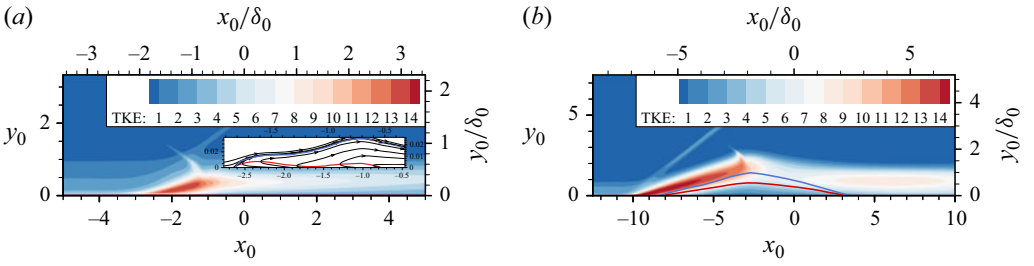


Figure 6. Contours of mean TKE fields under weak (a) and strong (b) interactions together with zero-velocity streamline (— line) and dividing streamline (— line).

TKE is consistently located above the dividing streamline. In the strong interaction, the local TKE peak appears to be elevated due to the increased wall-normal height of the separation bubble, resulting in a rise-and-fall pattern in the wall-normal direction as the flow evolves. Furthermore, the strong interaction exhibits a 'secondary amplification' of TKE with reduced intensity in the downstream recovery region, which is not observed in the weak interaction.

To better understand the TKE amplification process and identify its dominant factors, figure 7 presents the mean results of three normal stress components ($\widetilde{u''u''}$, $\widetilde{v''v''}$, $\widetilde{w''w''}$) and the shear stress component $-\widetilde{u''v''}$ for both interaction cases.

The results in figure 7(a,b) highlight that $\widetilde{u''u''}$, the dominant contributor to TKE in most regions of this SWTBLI problem, exhibits a similar evolution trend to that of TKE, with significant amplification occurring downstream of the separation shock. However, $\widetilde{v''v''}$ follows a different pattern. After being amplified near the separation shock foot, $\widetilde{v''v''}$ does not weaken significantly near the incident shock foot but instead dissipates gradually as the flow evolves. The two wall-parallel components, $\widetilde{w''w''}$ and $\widetilde{u''u''}$, exhibit similar streamwise evolution trends. While $\widetilde{w''w''}$ also amplifies near the separation shock, its amplification is less intense than that of $\widetilde{u''u''}$, and it weakens downstream of the incident shock. The shear stress component, $-\widetilde{u''v''}$, behaves differently from the normal stress components. Its local peak between the separation shock foot and the incident shock foot is closer to the wall. This behaviour aligns with the results of Fang *et al.* (2020) and may be related to the distinct amplification mechanisms of shear and normal stresses. For weak interaction, the intensity of $-\widetilde{u''v''}$ remains comparable upstream and downstream of the incident shock foot. In contrast, under strong interaction, the detached free shear layer downstream of the incident shock foot experiences a significant increase in $-\widetilde{u''v''}$, indicating a 'secondary amplification.' Similarly, all normal stresses under the strong interaction also exhibit 'secondary amplification' downstream of the incident shock. This phenomenon is absent in the weak interaction but resembles the initial amplification near the separation shock.

To provide a clearer comparison of stress amplification peak intensities and heights, figure 8 presents the streamwise evolution of local peak values, peak heights and amplification factors for various stress components. The amplification factor is normalised using the stress peaks of canonical turbulent boundary layers prior to turbulence amplification, as defined in (3.3)

$$\varphi_\alpha(x_0) = \frac{\Lambda_\alpha(x_0)}{\Lambda_\alpha(x_s)}, \tag{3.3}$$

https://doi.org/10.1017/jfm.2025.10616 Published online by Cambridge University Press

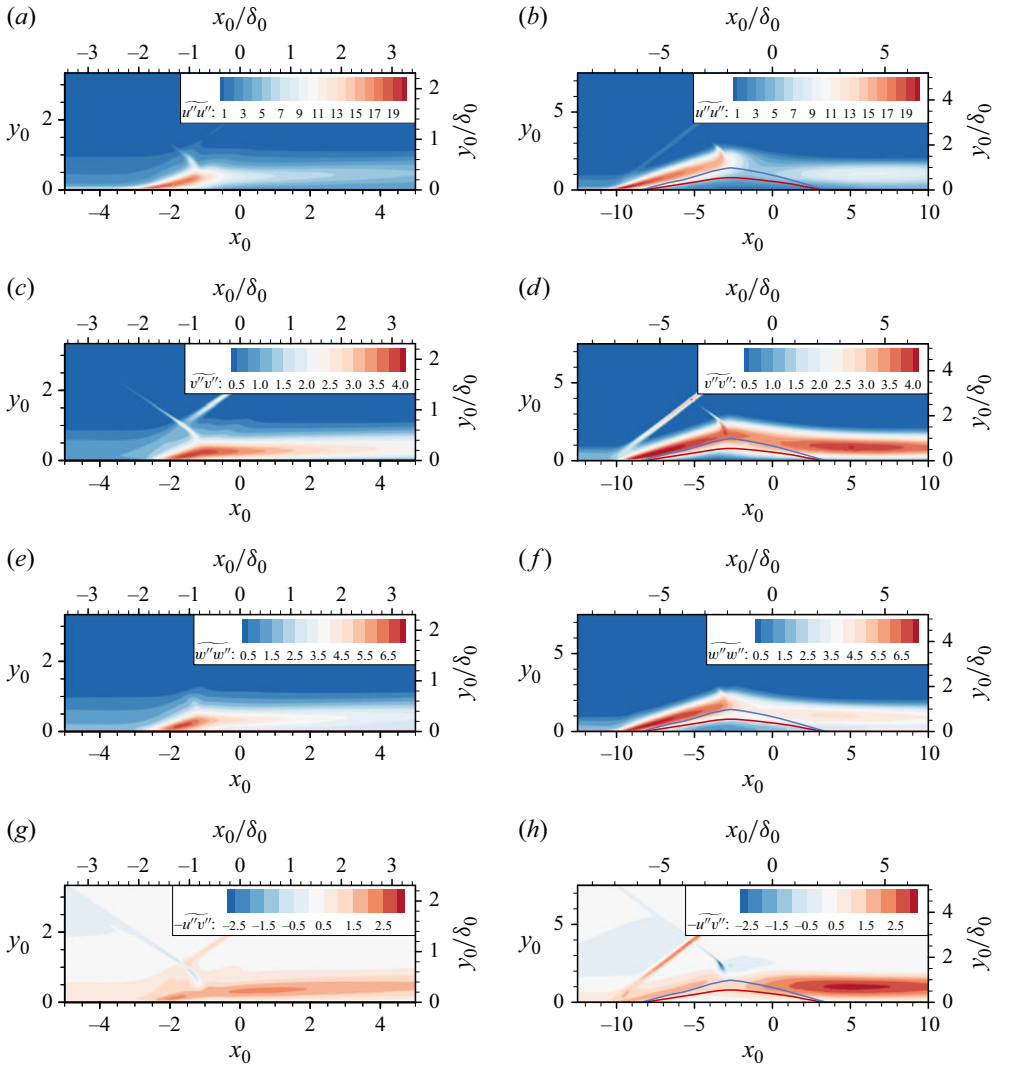


Figure 7. Contours of mean Reynolds stresses $\widetilde{u''u''}$ (*a*,*b*), $\widetilde{v''v''}$ (*c*,*d*), $\widetilde{w''w''}$ (*e*,*f*) and $-\widetilde{u''v''}$ (*g*,*h*) under weak (*a*,*c*,*e*,*g*) and strong (*b*,*d*,*f*,*h*) interactions together with zero-velocity streamline (— line) and dividing streamline (— line).

where, α represents the TKE or any Reynolds stress component, Λ denotes the local peak values at a given streamwise station x_0 and the undisturbed station, x_s, is set to $x_0 = -5$ and -12.5 for weak and strong interactions, respectively.

The streamwise evolution of local peaks reflects the proportional contribution of each stress component, while the amplification factor provides a direct comparison of the extent of amplification relative with free-stream conditions. Notably, the stress peak plots exclude the influence of shocks to facilitate a more accurate analysis of turbulence development trends and amplification mechanisms.

The streamwise evolution of peaks and amplification factors of Reynolds stresses and TKE, as depicted in figure 8, indicates that, despite significant differences in shock intensity and separation bubble structures between strong and weak interactions, the

https://doi.org/10.1017/jfm.2025.10616 Published online by Cambridge University Press

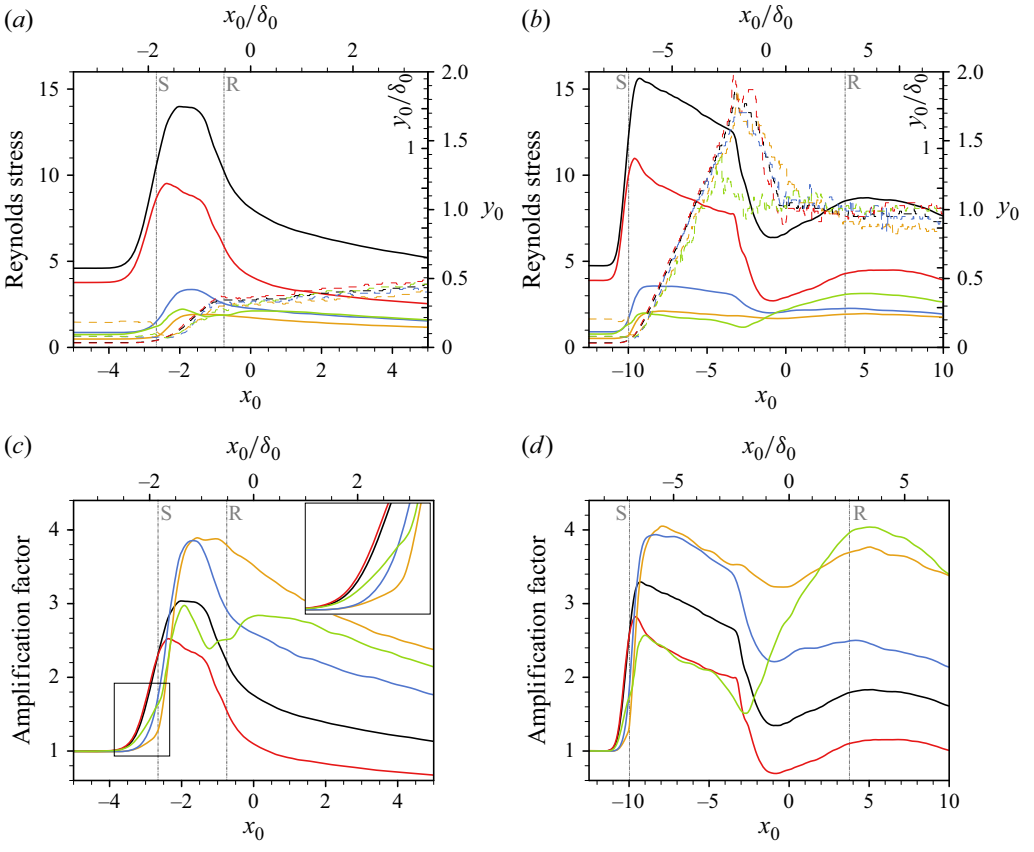


Figure 8. Streamwise evolutions of peak values (solid line) (*a*,*b*), peak heights (dashed line) (*a*,*b*) and amplification factors (solid line) (*c*,*d*) for TKE (black) and Reynolds stresses $\widetilde{u''u''}/2$ (—), $\widetilde{v''v''}/2$ (—), $\widetilde{w''w''}/2$ (—), $-\widetilde{u''v''}$ (—) under weak (*a*,*c*) and strong (*b*,*d*) interactions.

maximum peak values and amplification factors for each stress component during the initial amplification remain comparable. This suggests that shock intensity does not significantly enhance turbulence amplification, implying that the direct effect of shocks is not the primary mechanism driving turbulence amplification in SWTBLI. Moreover, regardless of interaction strength, the peaks of $\widetilde{u''u''}$ and TKE have similar streamwise evolution trends, even though their specific values differ, reaffirming the dominant role of $\widetilde{u''u''}$ in the TKE amplification process. Furthermore, as shown in the enlarged view, both strong and weak interactions exhibit the same initial amplification order for normal stresses: $\widetilde{u''u''}$, $\widetilde{w''w''}$ and $\widetilde{v''v''}$, with $\widetilde{u''u''}$ amplification beginning even upstream of the separation shock foot, as reported by Yu *et al.* (2022). For shear stress $-\widetilde{u''v''}$, initial amplification begins alongside $\widetilde{u''u''}$ but at a slower rate. However, as $\widetilde{v''v''}$ amplification progresses, the $-\widetilde{u''v''}$ amplification rate significantly accelerates, eventually matching the growth of other components.

The differences between strong and weak interactions are also evident. In the weak interaction case, both $\widetilde{u''u''}$ and $\widetilde{w''w''}$ exhibit significant amplification near the separation shock foot, followed by rapid decay upon crossing the incident shock foot, forming distinct amplification peaks that collectively shape the TKE peak. Meanwhile, $\widetilde{v''v''}$ undergoes

https://doi.org/10.1017/jfm.2025.10616 Published online by Cambridge University Press

notable amplification downstream of the separation shock foot but decays more gradually, resulting in a flatter peak. The shear stress $-\widetilde{u''v''}$ amplifies after the separation shock foot, with its decay upstream and subsequent increase downstream of the incident shock foot forming distinct double peaks in the amplification factor plot. Under strong interaction, $\widetilde{u''u''}$ rapidly amplifies near the separation shock foot. However, as discussed in § 3.1, the distance between the separation shock foot and the incident shock foot is larger in the strong interaction. Within this region, $\widetilde{u''u''}$ exhibits an approximately uniform decay rate, forming a 'slope platform' in the amplification factor plot. Near the incident shock foot, $\widetilde{u''u''}$ experiences a rapid stepped decay, followed by a weaker 'secondary amplification.' For $\widetilde{w''w''}$, the second-largest normal stress component contributing to TKE, no sharp amplification peak is observed near $x_0 = -9.6$ as seen in $\widetilde{u''u''}$. However, it still exhibits a 'slope platform' upstream of the incident shock foot, a stepped decay near the incident shock foot and a 'secondary amplification' downstream. In contrast, $\widetilde{v''v''}$, the smallest contributor to TKE, exhibits relatively minor variations in its local peak values along the streamwise direction. However, its amplification factor follows a pattern similar to $\widetilde{w''w''}$, except for the absence of a stepped decay process. The shear stress $-\widetilde{u''v''}$ also amplifies and forms a 'slope platform' downstream of the separation shock foot. Unlike the normal stresses, $-\widetilde{u''v''}$ displays a more pronounced 'secondary amplification' downstream of the incident shock foot, with its second peak significantly exceeding the first.

The streamwise evolution of peak heights also exhibits distinctions between strong and weak interactions. As illustrated in figure 8(*a*,*b*), the peak heights of stress components are significantly higher under strong interaction than weak interaction after amplification. However, within the same interaction, the streamwise evolution of peak heights across different stress components remains similar, with their peak positions generally aligning with the corresponding free shear layer. In the turbulent amplification region upstream of the incident shock, peak heights of all stress components gradually increase. Regardless of interaction strength, at the same streamwise station, $\widetilde{u''u''}$ consistently exhibits the highest peak position, while $\widetilde{v''v''}$ and $\widetilde{w''w''}$ maintain similar peak positions. This behaviour may be attributed to the earliest amplification of $\widetilde{u''u''}$. The TKE, as the sum of the three normal stresses, reaches a peak height slightly lower than that of $\widetilde{u''u''}$. In the downstream recovery region, the streamwise evolution of peak heights differs notably between strong and weak interactions. For weak interaction, peak heights continue to increase, whereas in strong interaction, a significant decrease occurs upstream of the reattachment point before $x_0 \approx 0$, followed by a slight downward trend further downstream.

In summary, turbulence amplification differs significantly between strong and weak interactions. In weak interaction, all normal stresses exhibit a single peak amplification, except for $-\widetilde{u''v''}$, which displays a double peak. In contrast, strong interaction features both a 'slope platform' and 'secondary amplification' for all stress components, with the boundaries of the 'slope platform' closely corresponding to the C_f and C_p plateaus. The unique amplification mechanisms observed in strong interaction, along with differences in the initial amplification sequence of stress components, will be further investigated in subsequent sections.

4. Turbulence amplification mechanism and budget decomposition

The previous section compared the mean results of strong and weak interactions, revealing the unique 'slope platform' and 'secondary amplification' phenomena in the streamwise

https://doi.org/10.1017/jfm.2025.10616 Published online by Cambridge University Press

evolution of Reynolds stress peaks under strong interaction. Regardless of interaction strength, the shear stress $-\widetilde{u''v''}$ consistently exhibited double peaks. Additionally, during the initial amplification stage, the dominant TKE component, $\widetilde{u''u''}$, amplified first. In contrast, $\widetilde{v''v''}$ amplified downstream of $\widetilde{w''w''}$ and near the separation shock foot, without undergoing a stepped decay process at the incident shock foot. This section examines the underlying mechanisms driving these amplification phenomena through a detailed analysis of the budget terms for each stress component.

4.1. *Budgets of turbulent kinetic energy and Reynolds stresses*

The TKE budgets provide a comprehensive view of energy production, transfer and dissipation, providing deeper insight into turbulence mechanisms (Yu *et al.* 2022). Additionally, analysing TKE budgets offers guidance for improving Reynolds-averaged Navier–Stokes models (Pirozzoli & Bernardini 2011*a*). Using the continuity and momentum equations, an unaveraged transport equation for Reynolds stresses can be derived, as presented in (4.1), with a detailed derivation available in Clark (2020)

$$\begin{aligned}\frac{\partial \rho u_i'' u_j''}{\partial t} =& -\frac{\partial \rho \widetilde{u}_k u_i'' u_j''}{\partial x_k} - \frac{\partial \rho u_k'' u_i'' u_j''}{\partial x_k} - \left(\frac{\partial p' u_j''}{\partial x_i} + \frac{\partial p' u_i''}{\partial x_j}\right) + \left(\frac{\partial u_i'' \tau_{jk}'}{\partial x_k} + \frac{\partial u_j'' \tau_{ik}'}{\partial x_k}\right) \\ & - \rho u_k'' \left(u_j'' \frac{\partial \widetilde{u}_i}{\partial x_k} + u_i'' \frac{\partial \widetilde{u}_j}{\partial x_k}\right) + p' \left(\frac{\partial u_j''}{\partial x_i} + \frac{\partial u_i''}{\partial x_j}\right) + \left(u_i'' \frac{\partial \overline{\tau}_{jk}}{\partial x_k} + u_j'' \frac{\partial \overline{\tau}_{ik}}{\partial x_k}\right) \\ & - \left(u_i'' \frac{\partial \overline{p}}{\partial x_j} + u_j'' \frac{\partial \overline{p}}{\partial x_i}\right) - \left(\tau_{ik}' \frac{\partial u_j''}{\partial x_k} + \tau_{jk}' \frac{\partial u_i''}{\partial x_k}\right). \end{aligned} \tag{4.1}$$

When $i = j$ and all terms are Reynolds averaged, the TKE transport equation is obtained, as shown in (4.2)

$$\begin{aligned}\frac{\partial \overline{\rho} K}{\partial t} =& \underbrace{-\frac{\partial \overline{\rho} \widetilde{u}_k K}{\partial x_k}}_{C_K} \underbrace{-\frac{\partial}{\partial x_k}\left(\frac{1}{2}\overline{\rho u_i'' u_i'' u_k''}\right)}_{DT_K} \underbrace{-\frac{\partial \overline{p' u_i''}}{\partial x_i}}_{Dp_K} + \underbrace{\frac{\partial \overline{u_i'' \tau_{ik}'}}{\partial x_k}}_{DV_K} \\ & \underbrace{-\overline{\rho u_i'' u_k''} \frac{\partial \widetilde{u}_i}{\partial x_k}}_{P_K} + \underbrace{\overline{p' \frac{\partial u_i''}{\partial x_i}}}_{\Pi_K} + \underbrace{\overline{u_i''}\left(\frac{\partial \overline{\tau}_{ik}}{\partial x_k} - \frac{\partial \overline{p}}{\partial x_i}\right)}_{M_K} \underbrace{-\overline{\tau_{ik}' \frac{\partial u_i''}{\partial x_k}}}_{\varepsilon_K}. \end{aligned} \tag{4.2}$$

Among these terms, C_K represents the convective term, DT_K the turbulent diffusion term, Dp_K the pressure diffusion term, DV_K the viscous diffusion term, P_K the production term, Π_K the pressure-strain term, M_K the mass flux term and ε_K the dissipation term.

The TKE budgets at the reference point are presented in figure 9, exhibiting high consistency with the results in Fang *et al.* (2020). In the near-wall region, the balance of TKE is primarily between viscous diffusion and dissipation, while in the logarithmic region, TKE is predominantly produced by P_K, transported to the near-wall region by diffusion terms and dissipated by ε_K. These results confirm that a canonical turbulent boundary layer is successfully established through blowing and suction, validating the accuracy of this study. A minor net gain in the total sum of budget terms near the P_K peak is observed, likely due to flow non-equilibrium. This phenomenon, also reported by Vyas *et al.* (2019), was attributed to the delayed energy redistribution following P_K amplification, leading to increased anisotropy and a net gain in the budgets.

https://doi.org/10.1017/jfm.2025.10616 Published online by Cambridge University Press

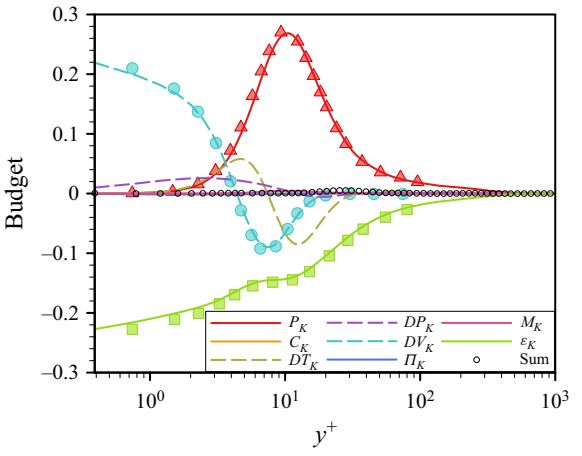


Figure 9. Comparison of TKE budget profiles. Lines are present results at x_{ref}, symbols are DNS results from Fang *et al.* (2020).

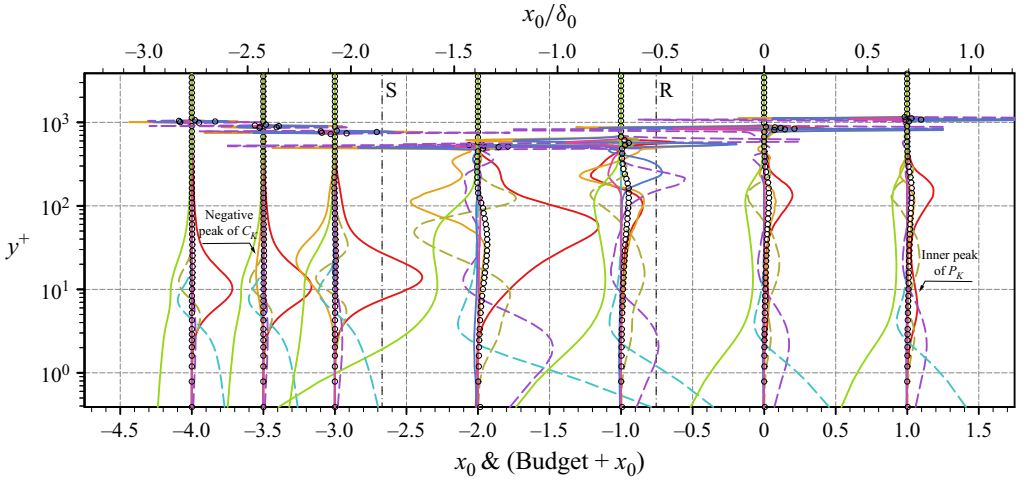


Figure 10. Streamwise evolution of TKE budget at different stations under the weak interaction. For the line legend, see figure 9.

4.2. *Streamwise evolution of budget terms in weak SWTBLI*

To systematically analyse the energy transfer and evolution of TKE budget terms in the SWTBLI, the TKE budgets at different streamwise stations under weak interaction are first presented in figure 10. Note that the horizontal axis represents both the streamwise position x_0 and the dimensionless budget values added to corresponding x_0.

The streamwise evolution of the TKE budget in figure 10 for weak interaction reveals that in the undisturbed upstream region at $x_0 = -4$, all budget terms conform to the behaviour of canonical turbulent boundary layers. At $x_0 = -3.5$, upstream of the separation shock foot, a negative peak in the convective term C_K emerges, balanced by an increase in the production term P_K. As previously discussed in the streamwise evolution of the TKE peak, figure 10 also highlights the initial TKE amplification occurring upstream of the separation shock foot. The C_K term represents energy transported by the mean flow (Yu *et al.* 2022), while P_K serves as the primary TKE production term. This indicates that, even without significant turbulence amplification due to shocks,

https://doi.org/10.1017/jfm.2025.10616 Published online by Cambridge University Press

upstream-propagating disturbances below the sonic line lead to slight flow deceleration upstream of the separation point. The energy from mean flow deceleration is absorbed by P_K as the initial energy source for TKE amplification, consistent with the conclusions of Fang *et al.* (2020). At $x_0 = -3$, near the separation shock foot, intensified mean flow deceleration increases the negative C_K peak, which shifts farther from the wall. Simultaneously, P_K amplifies significantly, indicating stronger turbulence production that corresponds to rapid TKE growth in figure 8(*c*). To balance the increased P_K, energy is transferred both toward the wall and outward through the turbulent diffusion term DT_K. Within the interaction region at $x_0 = -2$, while the overall budget balance remains unchanged, wall-normal budget profiles deviate significantly from those of canonical turbulence. Both the viscous diffusion term DV_K and dissipation term ε_K are amplified near the wall at approximately $y^+ < 4$ and remain balanced. The P_K peak reaches its maximum across the flow field and moves farther from the wall, matching the TKE peak height evolution in figure 8(*a*). Downstream of the incident shock foot at $x_0 = -1$ to 0, budget term profiles remain qualitatively similar to those at $x_0 = -2$, but the intensity of all terms, particularly P_K, decreases significantly. The appearance of positive C_K near the P_K peak suggests that post-shock expansion acceleration weakens P_K. At a further downstream station, $x_0 = 1$, all budget terms remain largely unchanged, and P_K exhibits an inner peak at $y^+ \approx 7$, signalling the re-establishment of the turbulent boundary layer.

Summarising the streamwise evolution of the TKE budget, a clear correlation is observed between TKE amplification and the production term P_K. The initial turbulence amplification appears to be driven by energy extracted from the mean flow by the P_K term, with this process occurring upstream of the separation shock.

The TKE budgets alone cannot explain the differences in the streamwise amplification order of various normal and shear stresses or the disparities in the peak evolution trends of each stress component. To further investigate the interrelations between these stresses and their streamwise evolution, the transport equations for $\widetilde{u''u''}$, $\widetilde{v''v''}$, $\widetilde{w''w''}$ and $-\widetilde{u''v''}$ are derived by specifying the subscript ij as 11, 22, 33 and 12 in (4.1) and applying Reynolds averaging. The resulting budget plots for these four stress components in weak interactions are presented in figures 11–14.

The budget plots of the normal stress components depicted in figures 11–13 reveal that the dominant component $\widetilde{u''u''}$ follows a streamwise evolution pattern similar to TKE across all streamwise stations, except for the pressure-strain term. The pressure-strain term Π_K, which exists only in compressible flows, governs energy exchange between kinetic and internal energy. Given that the SWTBLI in this study includes extensive subsonic regions and exhibits significant compressibility effects only near shocks, Π_K is nearly zero in the TKE budgets shown in figure 10. Consequently, the pressure-strain terms Π_{11}, Π_{22} and Π_{33} primarily describe inter-component energy transfer (Yu *et al.* 2022).

Figure 11 illustrates that the Π_{11} term in the $\widetilde{u''u''}$ budgets is predominantly negative in the outer peak for approximately $y^+ > 7$, with its peak position nearly coinciding with P_{11}. The intensity of Π_{11} appears to be influenced by the strength of P_{11}. Notably, a significant production term is observed only in the $\widetilde{u''u''}$ component, indicating that TKE production originates from $\widetilde{u''u''}$ and is subsequently redistributed to other components via the pressure-strain term. At $x_0 = -3$, upstream of the separation shock foot, Π_{11} activity is negligible in the near-wall region for the $\widetilde{u''u''}$ component. However, within the interaction region at $x_0 = -2$ and the downstream recovery region, positive Π_{11} values emerge near the wall, signifying a significant change in energy redistribution, where energy transfer from other components to $\widetilde{u''u''}$ becomes more pronounced in the near-wall region.

https://doi.org/10.1017/jfm.2025.10616 Published online by Cambridge University Press

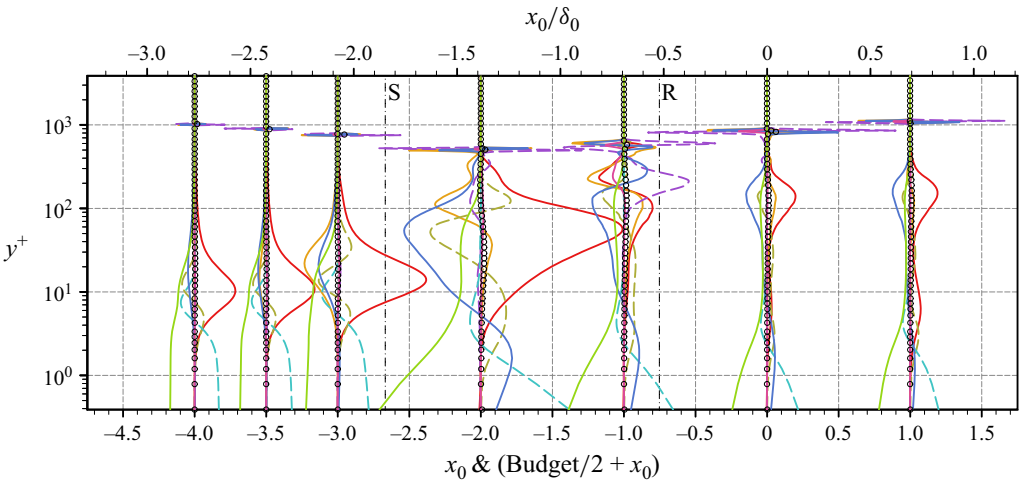


Figure 11. Streamwise evolution of $\widetilde{u''u''}$ budget at different stations under the weak interaction. For the line legend, see figure 9.

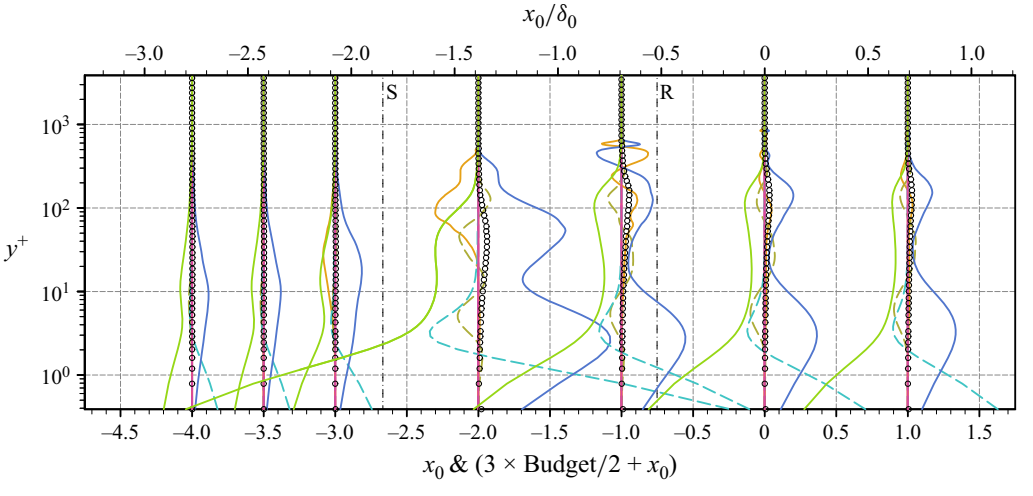


Figure 12. Streamwise evolution of $\widetilde{w''w''}$ budget at different stations under the weak interaction. For the line legend, see figure 9.

As illustrated in figure 12, the wall-parallel component $\widetilde{w''w''}$ exhibits behaviour similar to $\widetilde{u''u''}$ in the viscous diffusion term DV and dissipation term ε, where DV_{33} and ε_{33} achieve an approximate energy balance near the wall. However, in the outer peak where $y^+ > 7$, $\widetilde{w''w''}$ lacks energy production from the P_{33} term and primarily relies on energy transfers from $\widetilde{u''u''}$. In contrast to $\widetilde{u''u''}$, in the undisturbed region at $x_0 = -4$, the Π_{33} term for $\widetilde{w''w''}$ shows noticeable positive values in the near-wall region. After entering the interaction region at $x_0 = -2$, downstream of the separation shock foot, the Π_{33} term increases further in the inner region at $y^+ < 4$, forming a double peak. As the flow develops downstream, energy in all budget terms decreases, but the double peak of Π_{33} remains visible at $x_0 = 1$. These observations imply that in the undisturbed region,

https://doi.org/10.1017/jfm.2025.10616 Published online by Cambridge University Press

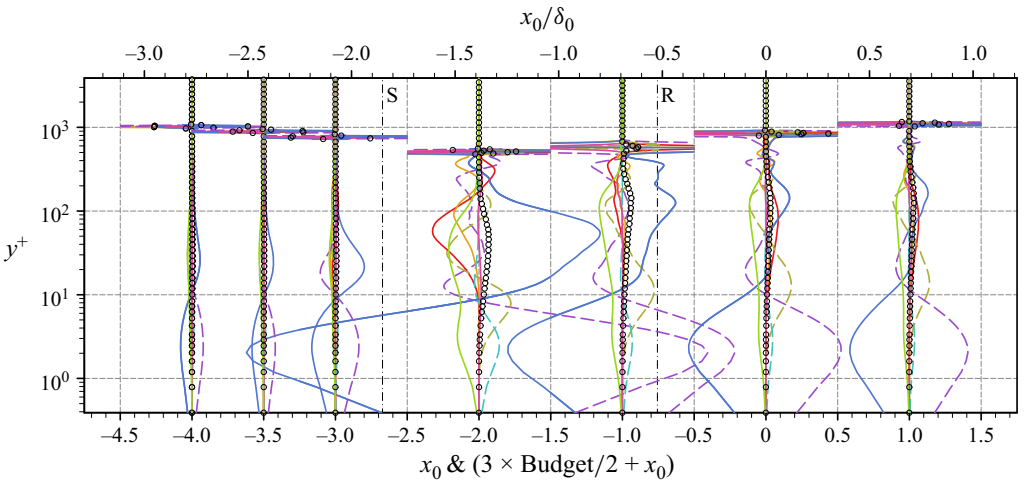


Figure 13. Streamwise evolution of $\widetilde{v''v''}$ budget at different stations under the weak interaction. For the line legend, see figure 9.

the $\widetilde{v''v''}$ component primarily transfers energy to $\widetilde{w''w''}$ in the inner region. However, downstream of the separation shock foot, $\widetilde{v''v''}$ simultaneously transfers energy to both $\widetilde{u''u''}$ and $\widetilde{w''w''}$ with greater intensity. In the outer region for approximately $y^+ > 9$, the main energy source for $\widetilde{w''w''}$ is $\widetilde{u''u''}$ component, and these distinct energy sources contribute to the double-peak pattern observed in Π_{33} for $\widetilde{w''w''}$.

The wall-normal $\widetilde{v''v''}$ component behaves differently compared with the wall-parallel components, as highlighted in figure 13. Two distinct energy transfer processes in the outer and inner peaks are evident throughout the flow evolution. In the outer peak for approximately $y^+ > 10$, energy transferred from $\widetilde{u''u''}$ generates Π_{22}, with some energy dissipated by the dissipation term ε_{22} and the rest transported to the inner region via the pressure diffusion Dp_{22} and turbulent diffusion DT_{22} terms. In the inner region, energy is primarily balanced by positive contributions from Dp_{22} and negative contributions from Π_{22}, where the negative Π_{22} indicates energy transferred from $\widetilde{v''v''}$ to $\widetilde{u''u''}$ and $\widetilde{w''w''}$. This energy transfer was also observed by Gungor *et al.* (2022) in DNS studies of APG turbulent boundary layers and may be attributed to the 'splatting effect' caused by the wall obstructing normal velocity (Moin & Kim 1982; Mansour, Kim & Moin 1988), which leads to energy redistribution to other components. The $\widetilde{v''v''}$ budget terms also amplify considerably after the separation shock foot and gradually decay downstream. At $x_0 = -3$ to -2, near the separation shock foot, a negative P_{22} is observed at the peak position of Π_{22}, while a positive P_{22} peak appears downstream at $x_0 = 0$. These changes are likely due to flow deflection caused by the detached shear layer and separation bubble, where the flow accelerates away from the wall at the leading edge of the separation bubble and decelerates towards the wall at the trailing edge. Similar to how streamwise deceleration generates P_k and acceleration decreases P_k in TKE budgets, these wall-normal velocity changes lead to different P_{22} signs for $\widetilde{v''v''}$ upstream and downstream of the separation. The negative P_{22} upstream may inhibit the amplification of $\widetilde{v''v''}$, while the positive P_{22} downstream appears to mitigate its decay.

https://doi.org/10.1017/jfm.2025.10616 Published online by Cambridge University Press

Summarising the discussion on normal stresses, the dominant component $\widetilde{u''u''}$ exhibits a streamwise budget evolution nearly identical to that of the total TKE. The wall-parallel components $\widetilde{u''u''}$ and $\widetilde{w''w''}$ behave similarly in terms of viscous diffusion (DV) and dissipation (ε), while the wall-normal component $\widetilde{v''v''}$ follows a completely distinct pattern. In regions where $y^+ > 7$, energy generation for $\widetilde{u''u''}$ is driven by the production term P_{11}, with partial energy transfer to $\widetilde{v''v''}$ and $\widetilde{w''w''}$ subsequently occurring through the pressure-strain term Π. This explains the earliest amplification of $\widetilde{u''u''}$ along the streamwise direction. However, $\widetilde{v''v''}$ amplifies downstream of $\widetilde{w''w''}$, likely influenced by the negative P_{22} near the separation shock foot. Near the wall, the energy transfer direction differs due to the 'splatting effect.' In the undisturbed region, $\widetilde{v''v''}$ transfers more energy to $\widetilde{w''w''}$, but downstream of the separation shock foot, the intensified inter-component energy transfer results in the development of double peaks in Π_{33} for $\widetilde{w''w''}$, with energy being transferred nearly equally to $\widetilde{u''u''}$ and $\widetilde{w''w''}$.

The budgets of the shear stress $-\widetilde{u''v''}$ in figure 14 reveal two distinct balance modes in the inner and outer peaks divided by $y^+ \approx 5$ throughout the flow evolution process. In the outer peak, $-\widetilde{u''v''}$ is produced by P_{12} and balanced by negative Π_{12}. In contrast, the inner region is dominated by a balance between Dp_{12} and Π_{12}, as these two terms collectively form the pressure term $(\overline{v''\partial p'/\partial x} + \overline{u''\partial p'/\partial y})$, which is zero at the wall. In the undisturbed region at $x_0 = -4$, Dp_{12} is positive and Π_{12} is negative in the inner region. Since Π_{12} balances different terms in the viscous sublayer and logarithmic region, this results in double peaks along the wall-normal direction. A significant change occurs upstream of the separation shock foot at $x_0 = -3.5$, where Dp_{12} shows its first negative peak at $y^+ \approx 5$, accompanied by a corresponding positive peak in Π_{12}. Near the separation shock foot at $x_0 = -3$, the signs of Dp_{12} and Π_{12} in the inner region reverse compared with the undisturbed region. A similar reversal occurs at $x_0 = -2.5$ in the interaction zone, returning to canonical turbulent conditions at $x_0 = -2$. During the flow through the separation compression waves, all budget terms experience significant amplification, reaching their maximum values near $x_0 = -2$. In the subsequent downstream evolution, these budget terms gradually dissipate, while their balance relationships remain unchanged. Notably, the peak position of P_{12} gradually increases downstream, consistent with the observations in figure 8(*a*). Although the P_{12} peak at $x_0 = -1$ has decayed compared with that at $x_0 = -2$, a slight increase is observed at $x_0 = 0$, possibly due to enhanced shear layer instability caused by the incident shock, which will be discussed in detail in § 4.4. This corresponds to the double-peak pattern of $-\widetilde{u''v''}$ in the streamwise evolution of weak interaction, as depicted in figure 8(*c*).

In conclusion, through budget analysis of TKE and Reynolds stresses under weak interaction, this study briefly identifies the primary energy sources and inter-component energy transfer relationships during turbulent amplification in SWTBLI. It is found that the dominant component $\widetilde{u''u''}$ and shear stress $-\widetilde{u''v''}$ are amplified by the production term P, while $\widetilde{v''v''}$ and $\widetilde{w''w''}$ derive energy from $\widetilde{u''u''}$ through the pressure-strain term Π. The differences in energy sources may explain the delayed initial amplification of $\widetilde{v''v''}$ and $\widetilde{w''w''}$ compared with $\widetilde{u''u''}$ and $-\widetilde{u''v''}$. Furthermore, the double-peak pattern of $-\widetilde{u''v''}$ and its production term in weak interaction, along with the variation in initial amplification rates, will be further explored in § 4.4.

https://doi.org/10.1017/jfm.2025.10616 Published online by Cambridge University Press

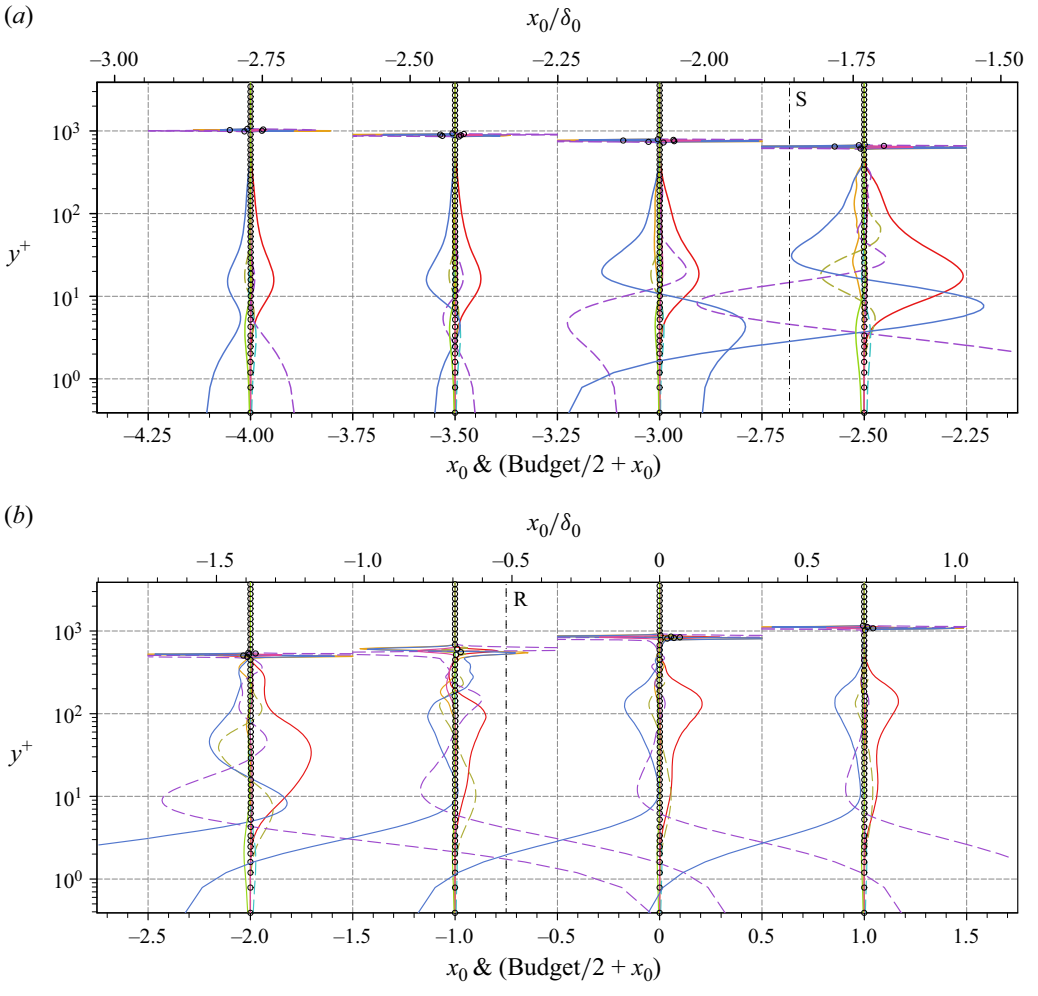


Figure 14. Streamwise evolution of $-\widetilde{u''v''}$ budget at different stations under the weak interaction: (*a*) $x_0 = -4$ to -2.5, (*b*) $x_0 = -2$ to 1. For the line legend, see figure 9.

4.3. *Streamwise evolution of budget terms in strong SWTBLI*

To explore the underlying physical mechanisms responsible for the 'slope platform' region and the 'secondary amplification' observed in strong interactions, the budgets of various Reynolds stresses are calculated at different streamwise stations. The results for TKE and individual stress components are presented in figures 15 and 17–20.

The streamwise evolution of the TKE budget for strong interaction, depicted in figure 15, reveals that the overall trends for each budget term largely align with those observed under weak interaction. The production term P_K, responsible for turbulence generation, still reaches its maximum downstream of the separation shock foot near $x_0 = -10$. At $x_0 = -8$, near the leading edge of the separation bubble, this P_K peak decays by approximately half, but the decay rate slows considerably at $x_0 = -6$ to -4 upstream of the incident shock foot. Throughout this process, the P_K peak height steadily moves away from the wall, corresponding to the first amplification of TKE observed in figure 8(*d*). The slow decay region for P_K, absent in weak interaction, arises from the larger separation zone in strong interaction, which extends the distance between the incident and separation shocks. This

https://doi.org/10.1017/jfm.2025.10616 Published online by Cambridge University Press

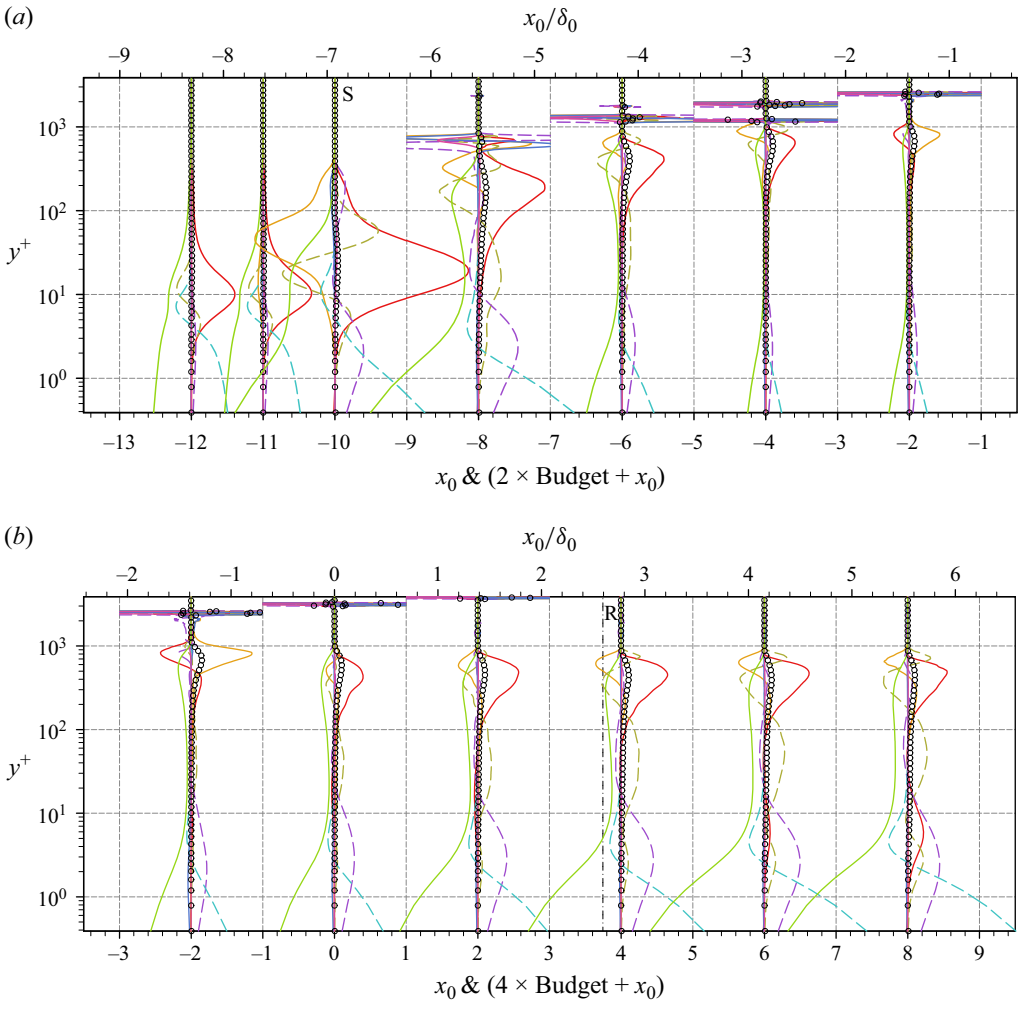


Figure 15. Streamwise evolution of TKE budget at different stations under the strong interaction: (*a*) $x_0 = -12$ to -2, (*b*) $x_0 = -2$ to 8. For the line legend, see figure 9.

elongated separation allows the flow more space to develop after the initial amplification near the separation shock foot. In addition, the absence of other energy amplification sources in this region, such as shocks, leads to slow dissipation behaviour similar to that of the recovery region. As the flow expands and accelerates downstream of the incident shock foot at $x_0 = -2$, the P_K peak intensity rapidly decays, similar to weak interaction. However, the larger wall-normal scale of the separation bubble in strong interaction causes a significant decrease in the P_K peak height as the bubble shrinks after crossing its upper vertex, a phenomenon nearly absent in weak interaction. In the downstream region at $x_0 = 0$ to 4, although the relationships among all budget terms remain consistent, a slight overall increase in their intensities is observed. This trend, also absent in weak interaction, suggests a potential new energy source, similar to a shock, located at the trailing edge of the reattachment point. This energy increase seems to result from flow compression induced by deflection at the trailing edge of the separation bubble in strong interaction. Supporting this hypothesis, figure 16 presents instantaneous snapshots of the density gradient magnitude for strong and weak interactions, which demonstrate that, although

https://doi.org/10.1017/jfm.2025.10616 Published online by Cambridge University Press

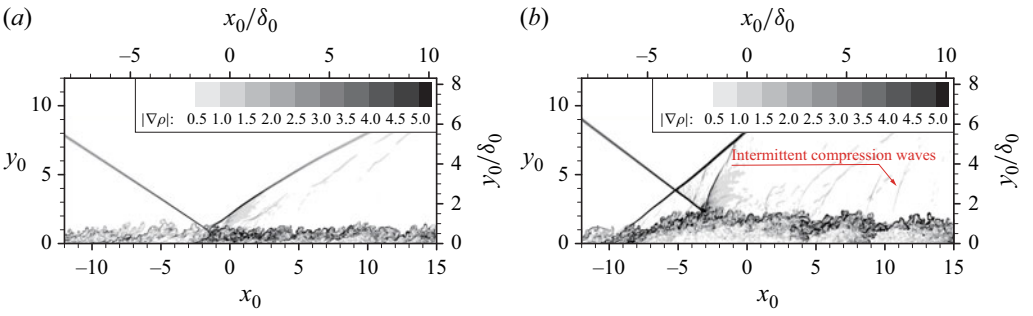


Figure 16. Contours of instantaneous density gradient magnitude fields under weak (*a*) and strong (*b*) interactions.

reattachment shocks are not discernible in the averaged results in figure 5, intermittent compression waves occur near the reattachment point. These downstream-propagating shocklets are stronger and more widespread in strong interaction and interact with the detached shear layer, enhancing flow compression and shear instability, ultimately causing the 'secondary amplification' of turbulence. This behaviour supports the findings of Kang & Lee (2024) for strong interaction at compression corners. After this compression, all budget terms are amplified until $x_0 = 6$. Downstream of this station, the budget pattern resembles that of the recovery region in weak interaction, with all budget terms slowly decaying except for a gradual increase in the inner peak of P_K.

The budget analysis for strong interaction reveals that P_K, as the primary production term of TKE, maintains a strong correlation with the streamwise evolution of TKE. Compared with weak interaction, strong interaction introduces two unique features: energy dissipation due to stable flow evolution downstream of the separation shock, and energy amplification caused by flow compression near the reattachment point. These correspond to the 'slope platform' region and the 'secondary amplification' process observed in TKE and Reynolds stresses, respectively. To better understand the energy transfer and amplification mechanisms within these regions, which exist only in strong interaction, a detailed budget analysis of each stress component is also performed.

Figures 17–20 show that the streamwise evolution of the stress components under strong interaction generally follows a pattern similar to that of weak interaction. However, distinct behaviours emerge in the 'slope platform' region between the separation and incident shocks. For the $\widetilde{u''u''}$ component, its maximum P_{11} occurs downstream of the separation shock foot at $x_0 \approx -10$. Here, the negative terms balancing P_{11}, mainly including the convective term C_{11}, the turbulent diffusion term DT_{11} and the pressure-strain term Π_{11}, reach their maximum negative values near $y^+ \approx 20{-}40$, with contributions stronger than those of the dissipation term ε_{11}. As the flow evolves downstream to $x_0 = -8$, the P_{11} peak rapidly decays, reducing its intensity by about half, similar to TKE. However, at this station, P_{11} is primarily balanced by Π_{11}, leading to a smaller relative decrease in Π_{11}. Further downstream at $x_0 = -6$ to -4 where upstream of the incident shock foot, budget terms such as P_{11} and Π_{11} gradually dissipate. As previously analysed, $\widetilde{u''u''}$ transfers energy to $\widetilde{v''v''}$ and $\widetilde{w''w''}$ through the pressure-strain term Π to amplify turbulence. Near the amplification peak at $x_0 = -10$ to -8, changes in the balance relationship of P_{11} contribute to a slower streamwise decay of Π_{11}. As confirmed in figures 18 and 19, the Π terms for $\widetilde{v''v''}$ and $\widetilde{w''w''}$ exhibit slight decreasing trends. This explains why $\widetilde{u''u''}$ displays a distinct peak near $x_0 = -9.6$ in the streamwise evolution plots of the

https://doi.org/10.1017/jfm.2025.10616 Published online by Cambridge University Press

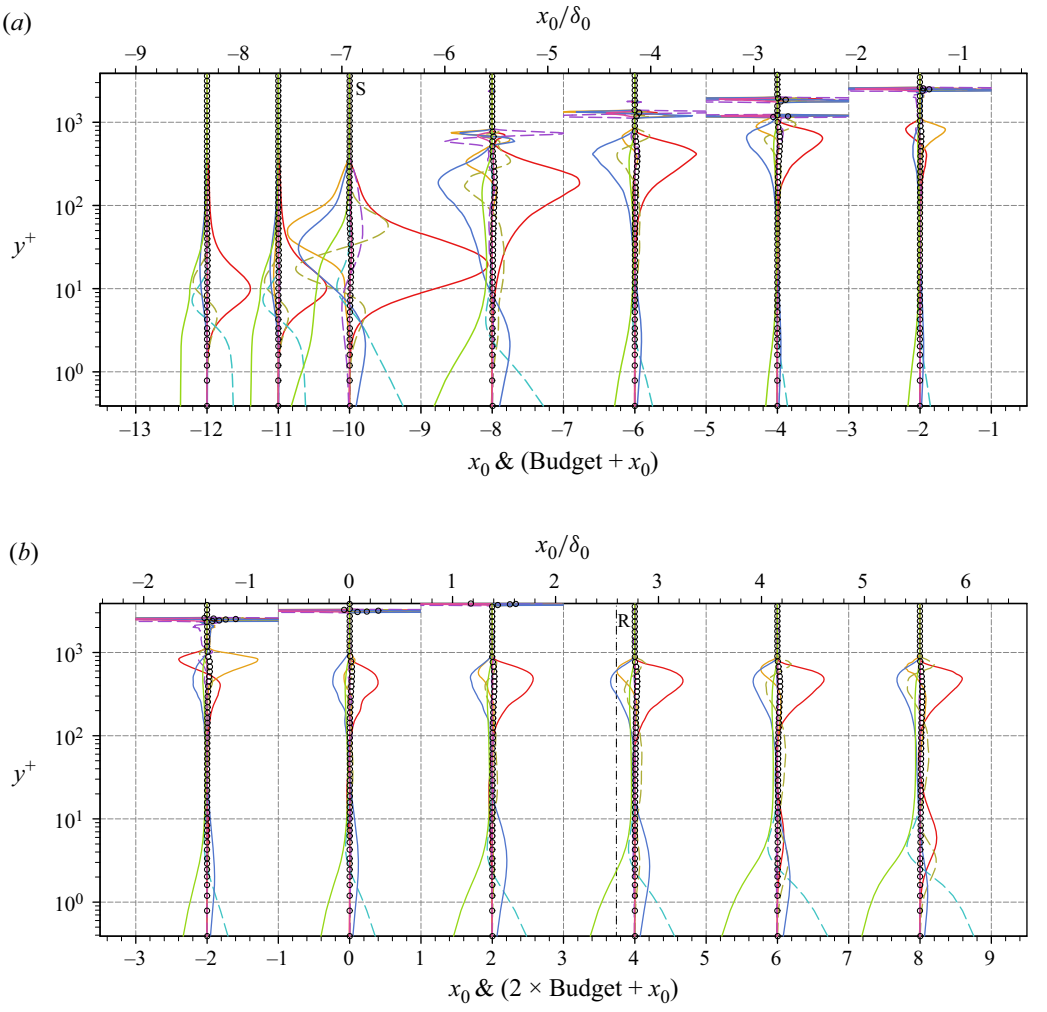


Figure 17. Streamwise evolution of $\widetilde{u''u''}$ budget at different stations under the strong interaction: (*a*) $x_0 = -12$ to -2, (*b*) $x_0 = -2$ to 8. For the line legend, see figure 9.

strong interaction in figures 8(*b*) and 8(*d*), while the $\widetilde{v''v''}$ and $\widetilde{w''w''}$ plots are smoother. Further downstream of the amplification peaks, the stable balance between P_{11} and Π_{11} in $\widetilde{u''u''}$ leads to the formation of the 'slope platform' region for all three normal stress components. Another notable distinction between strong and weak interactions lies in the recovery region downstream of the incident shock foot at $x_0 = -2$ to 8. Here, the emergence of reattachment compression waves significantly amplifies all budget terms, resulting in a 'secondary amplification' of P_{11} in the $\widetilde{u''u''}$ component and Π in the $\widetilde{v''v''}$ and $\widetilde{w''w''}$ components. Since the amplified energy primarily originates from P_{11} in $\widetilde{u''u''}$, and the balance between P_{11} and Π_{11} remains stable in the outer region by $y^+ > 100$, the amplification regions and rates of all three normal stress components appear relatively similar, as illustrated in figure 8(*d*).

As depicted in figure 19, the dominant energy production term for the $-\widetilde{u''v''}$ component is P_{12}, identical to that of the $\widetilde{u''u''}$ component. Consequently, the streamwise

https://doi.org/10.1017/jfm.2025.10616 Published online by Cambridge University Press

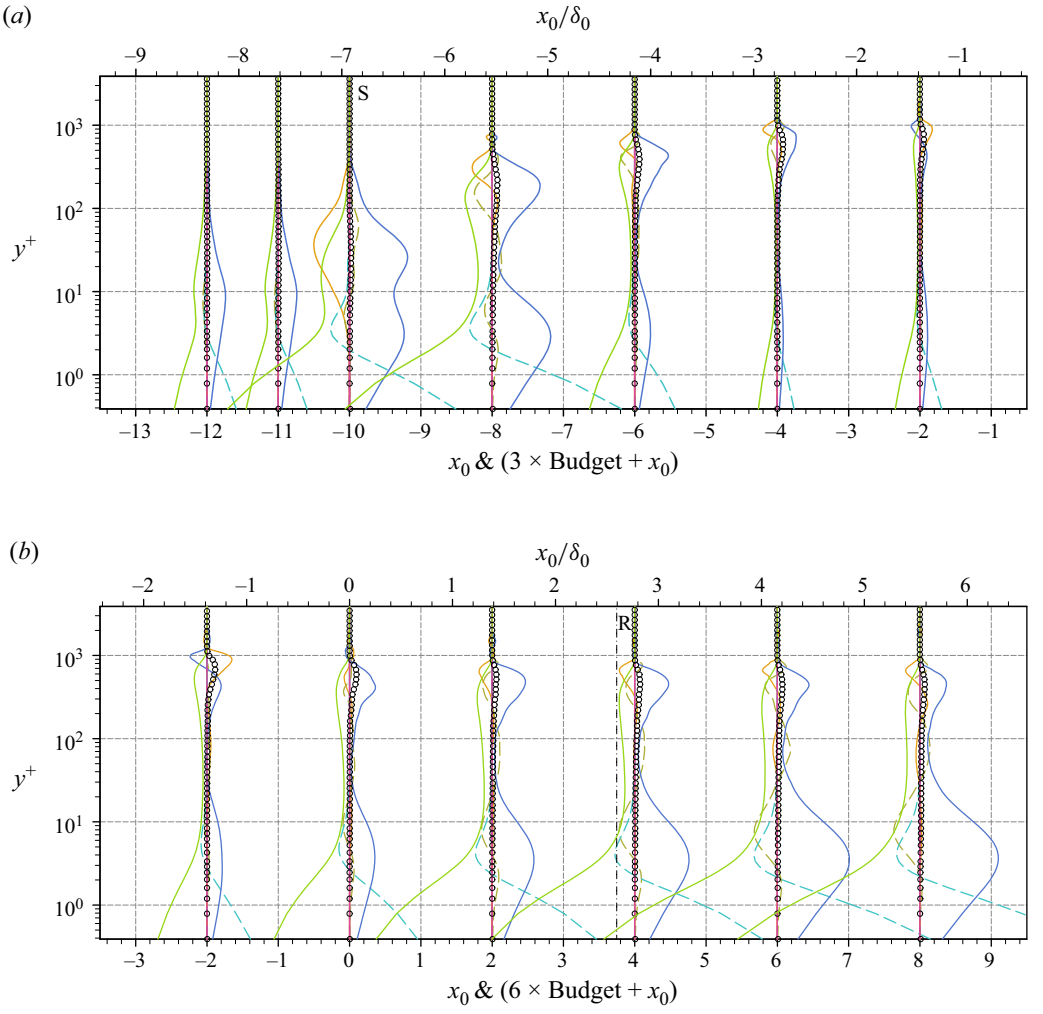


Figure 18. Streamwise evolution of $\widetilde{w''w''}$ budget at different stations under the strong interaction: (*a*) $x_0 = -12$ to -2, (*b*) $x_0 = -2$ to 8. For the line legend, see figure 9.

evolution of P_{12} in $-\widetilde{u''v''}$ is also similar to that of $\widetilde{u''u''}$ and TKE under strong interaction. Downstream of the separation shock foot at $x_0 = -11$, P_{12} experiences significant amplification, peaking at $x_0 = -10$ and then decaying to approximately half its strength by $x_0 = -8$, followed by a slow decay region between $x_0 = -6$ to -4. Similar to weak interaction, the weakest P_{12} peak appears near the incident shock foot at $x_0 = -4$ to -2. However, at downstream stations of $x_0 = -2$ to 2, despite the gradual decay of Dp_{12} and Π_{12} in the near-wall region, P_{12} begins to recover, potentially driven by enhanced shear instability induced by the incident shock. In contrast to weak interaction, further downstream at $x_0 = 4$ to 8 in strong interaction, intermittent reattachment compression waves amplify all major contributing terms, including Dp_{12} and Π_{12}, in the near-wall region. Simultaneously, the peak intensity of P_{12} undergoes an additional enhancement. Summarising this process, the streamwise evolution of P_{12} in $-\widetilde{u''v''}$ upstream of the incident shock foot follows a pattern nearly identical to that in $\widetilde{u''u''}$. During the initial

https://doi.org/10.1017/jfm.2025.10616 Published online by Cambridge University Press

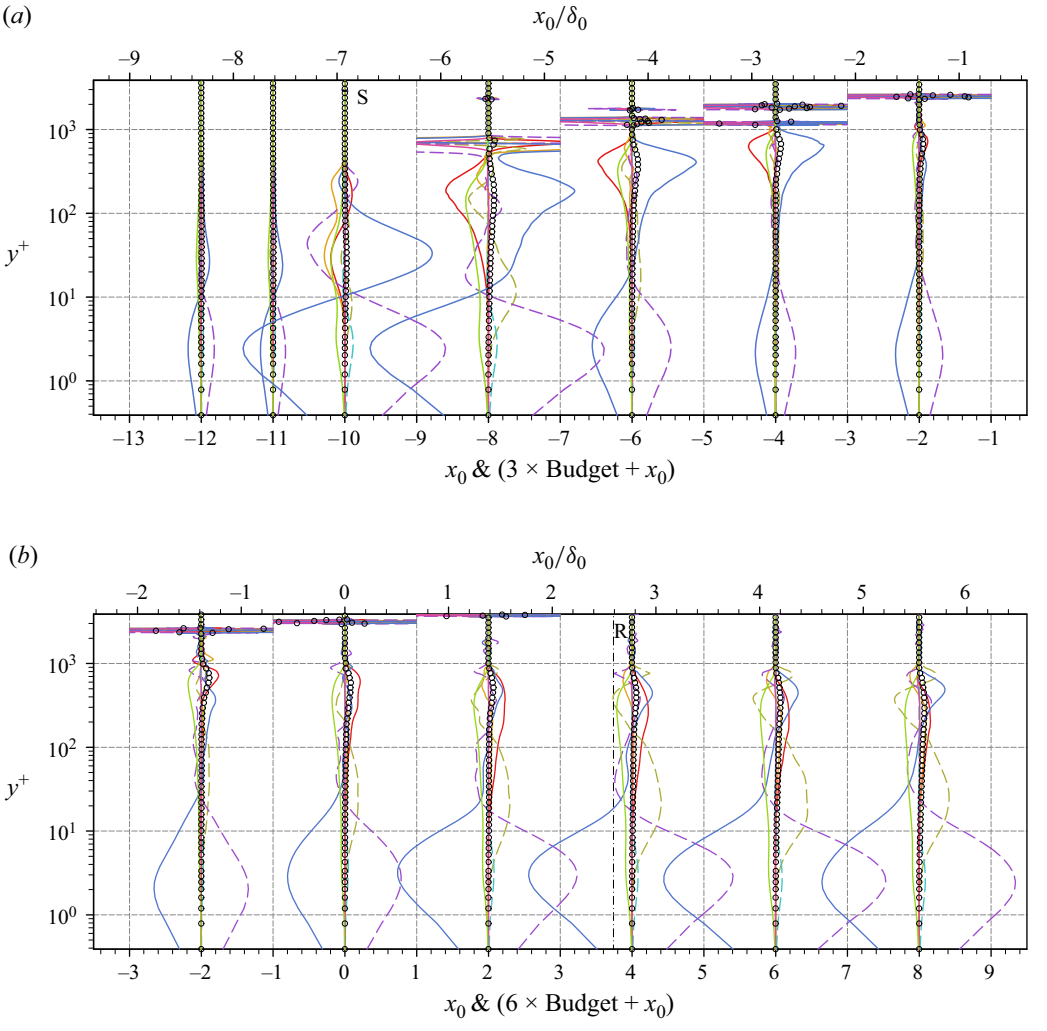


Figure 19. Streamwise evolution of $\widetilde{v''v''}$ budget at different stations under the strong interaction: (*a*) $x_0 = -12$ to -2, (*b*) $x_0 = -2$ to 8. For the line legend, see figure 9.

amplification stage, the amplification factors of $-\widetilde{u''v''}$ and $\widetilde{u''u''}$ exhibit comparable trends, as illustrated in figure 8(*d*). However, downstream of the incident shock foot, P_{12} in $-\widetilde{u''v''}$ experiences dual amplification, driven by both the incident shock and the reattachment compression waves. As a result, the downstream amplification of $-\widetilde{u''v''}$ under strong interaction is more pronounced than that of the normal stress components. This observation aligns with the higher amplification rate of $-\widetilde{u''v''}$ observed during the 'secondary amplification' process in the streamwise peak evolution plots of Reynolds stresses in figure 8(*d*).

In summary, this subsection reaffirms that the dominant contribution budgets and energy redistribution mechanisms established under weak interaction also hold for strong interaction, as demonstrated through budget term analysis. The streamwise evolution of these dominant terms shows a clear correlation with their corresponding stress components, exhibiting the unique 'slope platform' region upstream of the incident shock

https://doi.org/10.1017/jfm.2025.10616 Published online by Cambridge University Press

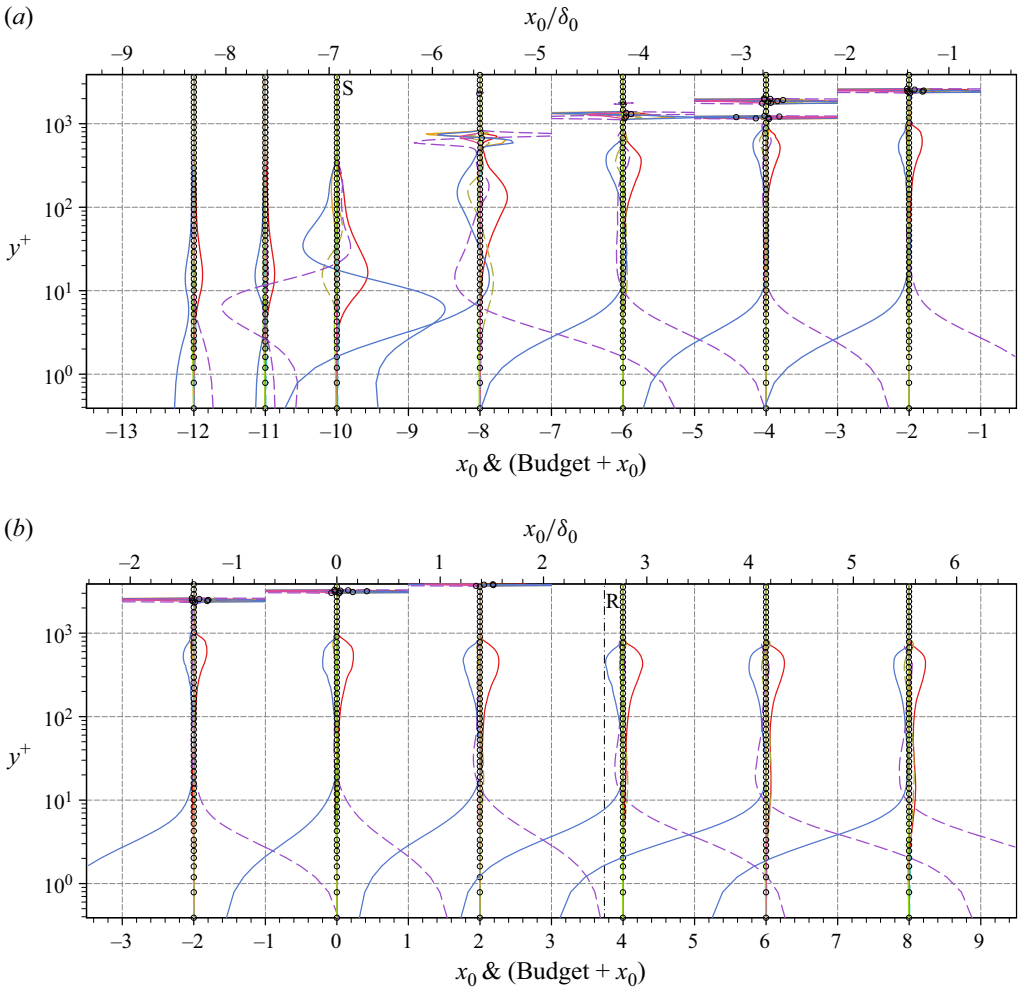


Figure 20. Streamwise evolution of $-\widetilde{u''v''}$ budget at different stations under the strong interaction: (*a*) $x_0 = -12$ to -2, (*b*) $x_0 = -2$ to 8. For the line legend, see figure 9.

and the 'secondary amplification' process downstream. This study concludes that during the initial amplification in strong interaction, the primary production term P_{11} of $\widetilde{u''u''}$ decays rapidly after peaking near the separation shock foot, followed by a slower and more stable decay downstream. In contrast, Π_{11}, which transfers energy to the $\widetilde{v''v''}$ and $\widetilde{w''w''}$ components, shows consistent dissipation in this region. The uniform decay of dominant budget terms responsible for stress amplification forms the 'slope platform' region, with $\widetilde{u''u''}$ displaying a sharp peak at its leading edge. Since TKE is dominated by $\widetilde{u''u''}$, it exhibits a similar behaviour. Additionally, the dominant production term for $-\widetilde{u''v''}$ is also P_{12}, leading to an initial amplification process resembling that of $\widetilde{u''u''}$. The 'secondary amplification' is likely caused by intermittent travelling reattachment compression waves, which amplify all normal stress components at comparable rates due to their shared energy source. However, $-\widetilde{u''v''}$ undergoes dual amplification by the

https://doi.org/10.1017/jfm.2025.10616 Published online by Cambridge University Press

incident and reattachment shocks, resulting in a greater intensity and a higher amplification rate during the 'secondary amplification' process.

4.4. *Budget decomposition and dominant amplification mechanisms for Reynolds stresses*

As discussed in the previous subsection, the production and transfer of energy are primarily governed by the P and Π terms. To analyse the dominant flow states and inter-component energy transfer mechanisms during stress amplification under varying strengths of SWTBLI, this subsection further decomposes the P and Π terms for different stress components. As expressed in (4.3), each normal stress component consists of two P sub-terms and one Π sub-term, while the shear stress component $-\widetilde{u''v''}$ is decomposed into four P sub-terms and two Π sub-terms

$$P_{11} = \underbrace{-2\overline{\rho}\widetilde{u''u''}\frac{\partial \widetilde{u}}{\partial x}}_{P_{11}^{x}} \underbrace{-2\overline{\rho}\widetilde{u''v''}\frac{\partial \widetilde{u}}{\partial y}}_{P_{11}^{y}}, \quad \Pi_{11} = 2\overline{p'\frac{\partial u''}{\partial x}},$$

$$P_{22} = \underbrace{-2\overline{\rho}\widetilde{v''u''}\frac{\partial \widetilde{v}}{\partial x}}_{P_{22}^{x}} \underbrace{-2\overline{\rho}\widetilde{v''v''}\frac{\partial \widetilde{v}}{\partial y}}_{P_{22}^{y}}, \quad \Pi_{22} = 2\overline{p'\frac{\partial v''}{\partial y}},$$

$$P_{33} = \underbrace{-2\overline{\rho}\widetilde{w''u''}\frac{\partial \widetilde{w}}{\partial x}}_{P_{33}^{x}} \underbrace{-2\overline{\rho}\widetilde{w''v''}\frac{\partial \widetilde{w}}{\partial y}}_{P_{33}^{y}}, \quad \Pi_{33} = 2\overline{p'\frac{\partial w''}{\partial z}},$$

$$P_{12} = \underbrace{\overline{\rho}\widetilde{u''u''}\frac{\partial \widetilde{v}}{\partial x}}_{P_{12}^{x1}} + \underbrace{\overline{\rho}\widetilde{u''v''}\frac{\partial \widetilde{v}}{\partial y}}_{P_{12}^{y1}} + \underbrace{\overline{\rho}\widetilde{v''u''}\frac{\partial \widetilde{u}}{\partial x}}_{P_{12}^{x2}} + \underbrace{\overline{\rho}\widetilde{v''v''}\frac{\partial \widetilde{u}}{\partial y}}_{P_{12}^{y2}}, \quad \Pi_{12} = \underbrace{-\overline{p'\frac{\partial v''}{\partial x}}}_{\Pi_{12}^{x}} \underbrace{-\overline{p'\frac{\partial u''}{\partial y}}}_{\Pi_{12}^{y}}. \tag{4.3}$$

Figures 21–25 display the mean results of P, Π and their sub-terms for $\widetilde{u''u''}$, $\widetilde{v''v''}$, $\widetilde{w''w''}$ and $-\widetilde{u''v''}$ under both strong and weak interactions. For brevity, the P_{33} term and its sub-terms are omitted, as they are nearly zero throughout the entire flow field.

The $\widetilde{u''u''}$ component is the dominant contributor to TKE in this SWTBLI problem, and its P_{11} term nearly represents turbulence production. As a result, the mean contours of P_{11} in figure 21(*a*,*b*) and TKE in figure 7(*a*,*b*) show strong consistency for both strong and weak interactions. The decomposition of P_{11} further supports the conclusion from Fang *et al.* (2020), stating that the P_{11}^{x} term ($-2\overline{\rho}\widetilde{u''u''}\partial\widetilde{u}/\partial x$), related to flow deceleration, dominates turbulence amplification upstream of the incident shock. Meanwhile, the P_{11}^{y} term ($-2\overline{\rho}\widetilde{u''v''}\partial\widetilde{u}/\partial y$), associated with shear, is comparatively weaker but begins to amplify near the separation shock foot, peaking along the shear layer and extending into the downstream recovery region. Although 'secondary amplification' regions are observed in the P_{11} contours for both strong and weak interactions, their underlying mechanisms differ significantly. In the weak interaction case, expansion waves downstream of the incident shock accelerate the flow, causing $\partial\widetilde{u}/\partial x$ to become positive and generating negative P_{11}^{x}. Additionally, an energy loss occurs in P_{11}^{y} at the incident shock foot, primarily due to the weaker local intensity of $-\widetilde{u''v''}$ in P_{11}^{y} relative to nearby regions, as illustrated in the

https://doi.org/10.1017/jfm.2025.10616 Published online by Cambridge University Press

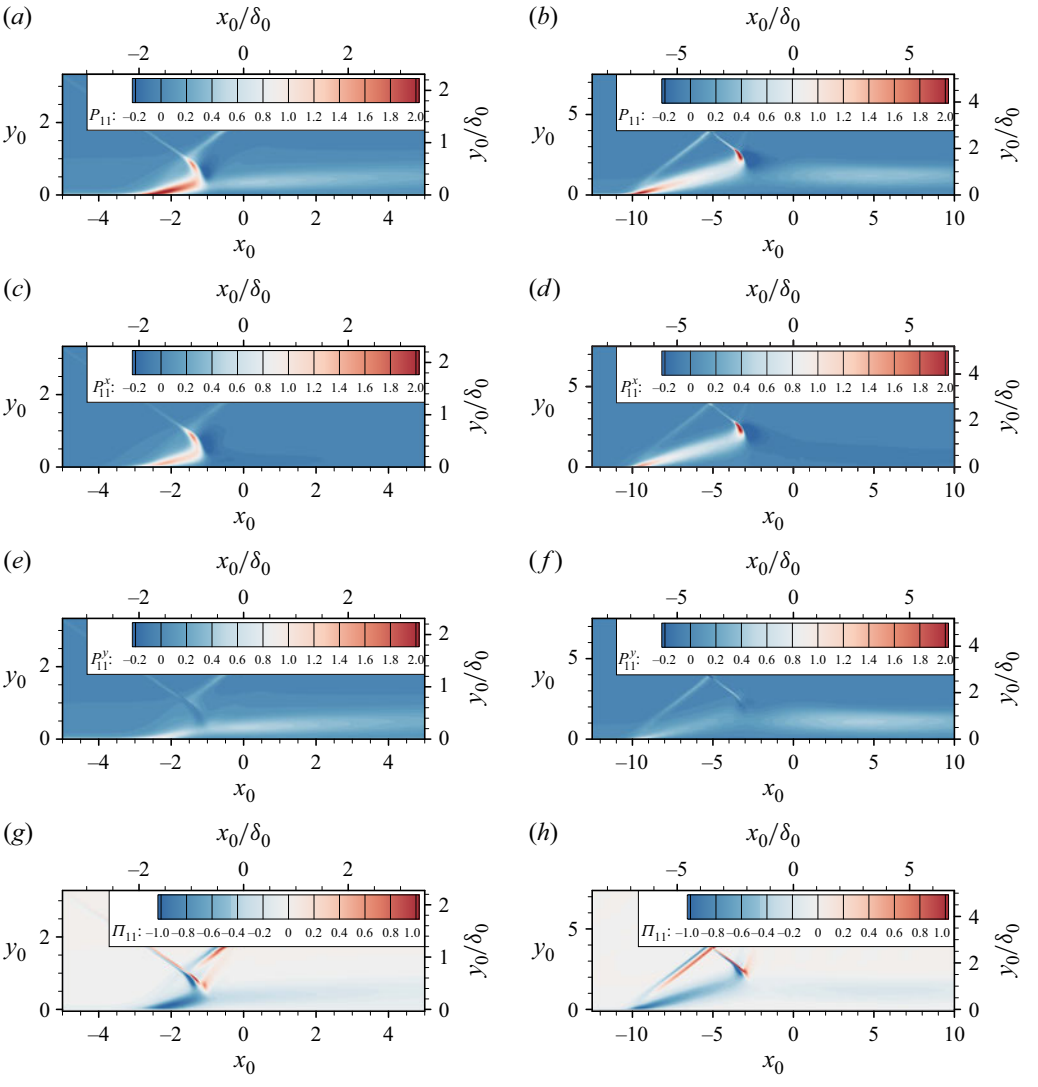


Figure 21. Contours of mean production terms P_{11} (a,b), their sub-terms P_{11}^x (c,d), P_{11}^y (e,f) and pressure-strain term Π_{11} (g,h) for $\widetilde{u''u''}$ component under weak (a,c,e,g) and strong (b,d,f,h) interactions.

averaged results of $-\widetilde{u''v''}$ and P_{12} in figures 7(g) and 24(a). A more detailed analysis of this $-\widetilde{u''v''}$ deficit will be provided in later discussions. Both P_{11}^x and P_{11}^y decrease near the incident shock foot, resulting in a local minimum of P_{11} at this station. However, as the flow develops downstream, the effects of flow acceleration from expansion waves and the $-\widetilde{u''v''}$ deficit diminish, enabling P_{11} to temporarily recover to its upstream P_{11}^y intensity before gradually dissipating. This recovery process explains the 'secondary amplification' observed in weak interaction. In strong interaction, while a similar process occurs, the larger distance between the separation and incident shocks leads to further dissipation of P_{11}^y before it reaches the incident shock foot. Consequently, P_{11} downstream of the incident shock cannot recover to a higher intensity. Figures 21(f) and 24(b) reveal that, despite the rapid recovery of $-\widetilde{u''v''}$ after the incident shock, the P_{11}^y in strong interaction

https://doi.org/10.1017/jfm.2025.10616 Published online by Cambridge University Press

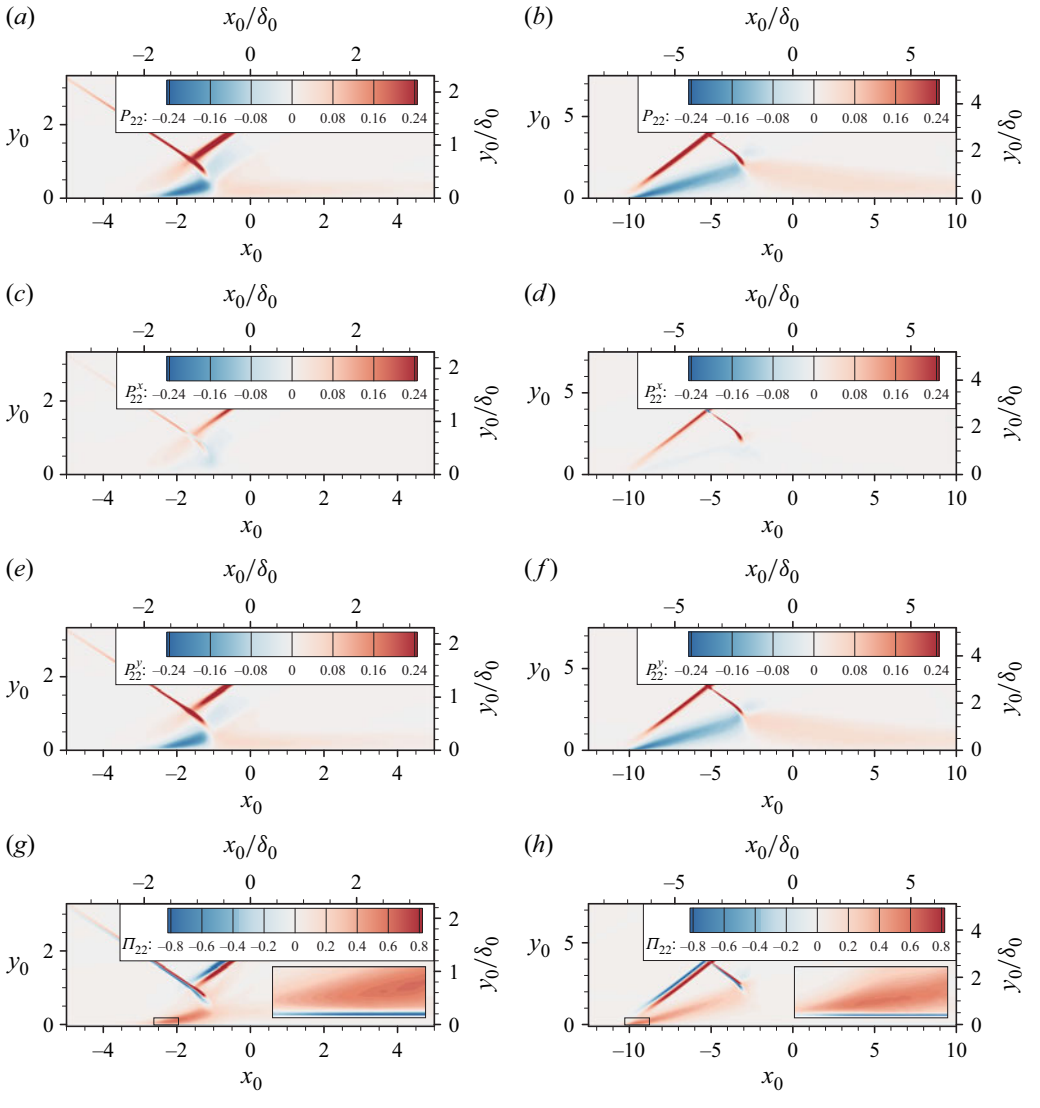


Figure 22. Contours of mean production terms P_{22} (*a*,*b*), their sub-terms P_{22}^x (*c*,*d*), P_{22}^y (*e*,*f*) and pressure-strain term Π_{22} (*g*,*h*) for $\widetilde{v''v''}$ component under weak (*a*,*c*,*e*,*g*) and strong (*b*,*d*,*f*,*h*) interactions.

only reaches the lower energy levels upstream of the incident shock foot. The 'secondary amplification' of P_{11}^y occurs further downstream, and as discussed in § 4.3, is likely driven by reattachment compression waves that enhance flow compression and shear instability.

As illustrated in figure 22, P_{22} is primarily contributed by P_{22}^y $(-2\widetilde{\rho v''v''}\partial\widetilde{v}/\partial y)$, and its trends for strong and weak interactions are not significantly different. Upstream of the incident shock, P_{22}^y is negative due to the wall-normal acceleration of $\widetilde{v}$, while downstream, it becomes positive as wall-normal velocity decelerates. The primary energy source for $\widetilde{v''v''}$ remains the transfer from $\widetilde{u''u''}$ via the Π term. In the weak interaction, the Π_{22} distribution in figure 22(*g*) consistently exhibits negative values near the wall, which intensify downstream of the separation shock. Although the same energy transfer mechanism occurs in strong interaction as discussed in § 4.3, the Π_{22} contour in

https://doi.org/10.1017/jfm.2025.10616 Published online by Cambridge University Press

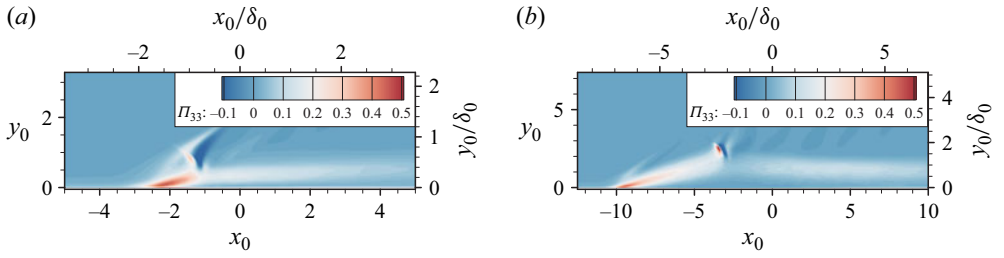


Figure 23. Contours of mean pressure-strain term Π_{33} for $\widetilde{w''w''}$ component under weak (*a*) and strong (*b*) interactions.

figure 22(*h*) appears less distinct due to the larger spatial scale of the strong interaction region. However, upon examining the enlarged view, similar negative Π_{22} patterns can be observed, which are related to the 'splatting effect.' Therefore, while strong interaction significantly affects the shape of the separation bubble and subsequently affects the turbulence amplification process, the overall scale of energy transfer and the corresponding dominant budget terms remain similar. Particularly near the separation shock foot, the behaviours under strong and weak interactions are nearly identical, with comparable initial amplification factors as shown in figure 8(*c*,*d*). This suggests that the primary difference in turbulence amplification between strong and weak interactions arises not from the gradient changes with the incident shock angle, but from differences in the size and shape of the separation zone, which influence the flow evolution and ultimately the amplification path.

In this SWTBLI problem, P_{33} is negligible due to the absence of spanwise shocks. Nonetheless, figure 23 reveals significant amplification of Π_{33} downstream of the separation shock, especially near the wall and within the detached shear layer.

Figure 24 presents the decomposition of the P_{12} term, revealing that the deficit in P_{12} at the incident shock foot results from the combined effects of P_{12}^{x1} ($\widetilde{\rho u''u''}\partial\widetilde{v}/\partial x$), which negatively contributes at the shock foot, and P_{12}^{y2} ($\widetilde{\rho v''v''}\partial\widetilde{u}/\partial y$), which remains positive in the shear layer but gradually weakens downstream after amplification. The other two sub-terms have negligible contributions. From the averaged normal velocity contour in figure 26(*a*,*b*), it is evident that after crossing the separation shock, the wall-normal velocity $\widetilde{v}$ steadily increases along the streamwise direction, reaching a maximum before the incident shock foot, and then rapidly decelerating with a steeper gradient. This deceleration near the incident shock foot explains the negative contribution of P_{12}^{x1}. In contrast, $\partial\widetilde{u}/\partial y$ stays positive along the shear layer with relatively small variations, and the peak of $\widetilde{v''v''}$ also remains stable in the interaction zone, ensuring a more uniform amplification of P_{12}^{y2}. During the initial turbulence amplification stage, P_{12}^{y2} serves as the dominant production sub-term for $-\widetilde{u''v''}$. The APG in the interaction zone alters the upstream velocity profile, slowing the streamwise velocity and weakening its wall-normal gradient near the wall. However, the peak position of $-\widetilde{u''v''}$ is higher than that of $\widetilde{u''u''}$ in the canonical turbulent boundary layer. As shown in figure 26(*c*,*d*), $\partial\widetilde{u}/\partial y$ not only remains positive at the height of the $-\widetilde{u''v''}$ peak but also increases along the streamwise direction due to velocity profile changes induced by the APG. Therefore, the initial amplification position of $-\widetilde{u''v''}$ is close to that of $\widetilde{u''u''}$. However, since $\widetilde{v''v''}$ does not amplify at this station, $-\widetilde{u''v''}$ initially grows at a slower rate. Once $\widetilde{v''v''}$ begins to amplify, $-\widetilde{u''v''}$ exhibits amplification rates comparable to those of the other normal stresses.

https://doi.org/10.1017/jfm.2025.10616 Published online by Cambridge University Press

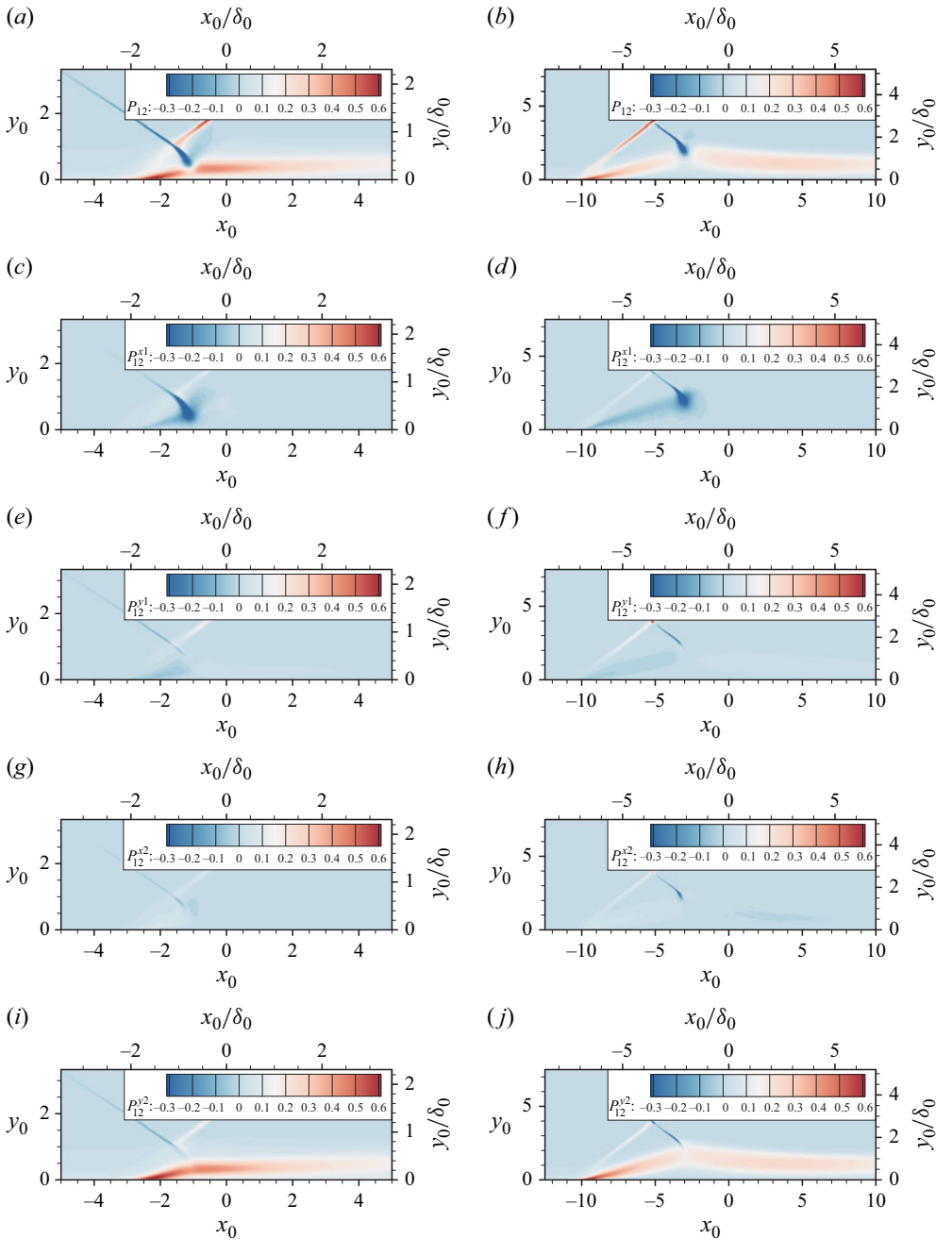


Figure 24. Contours of mean production terms P_{12} (*a*,*b*) and their sub-terms P_{12}^{x1} (*c*,*d*), P_{12}^{y1} (*e*,*f*), P_{12}^{x2} (*g*,*h*), P_{12}^{y2} (*i*,*j*) for $-\widetilde{u''v''}$ component under weak (*a*,*c*,*e*,*g*,*i*) and strong (*b*,*d*,*f*,*h*,*j*) interactions.

In addition, as demonstrated in figure 25, the distinct behaviour of Π_{12} between the near-wall region and the shear layer arises from the combined effects of Π_{12}^{x} $(-\overline{p'\partial v''/\partial x})$ and Π_{12}^{y} $(-\overline{p'\partial u''/\partial y})$. Enlarged contours for strong interaction reveal that Π_{12}^{y} dominates near the wall, while Π_{12}^{x} prevails in the outer region. The sign change of Π_{12} along the

https://doi.org/10.1017/jfm.2025.10616 Published online by Cambridge University Press

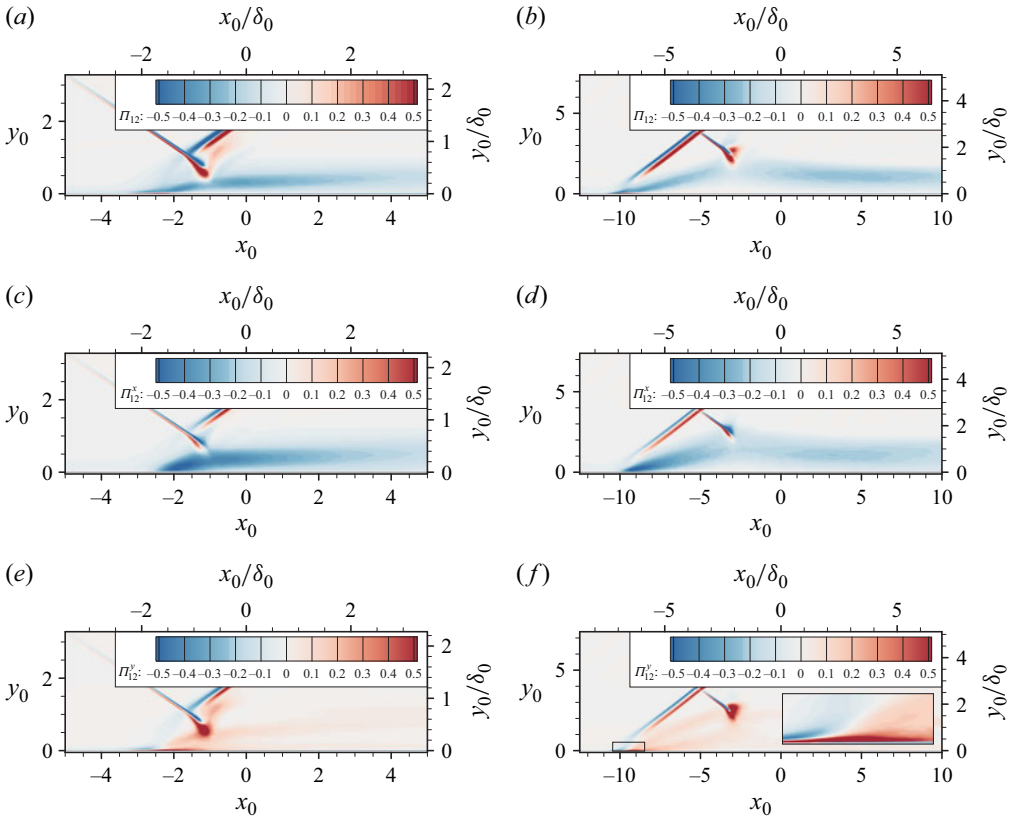


Figure 25. Contours of mean pressure-strain terms Π_{12} (*a*,*b*) and their sub-terms Π_{12}^x (*c*,*d*), Π_{12}^y (*e*,*f*) for $-\widetilde{u''v''}$ component under weak (*a*,*c*,*e*) and strong (*b*,*d*,*f*) interactions.

wall near the separation shock foot, as revealed in § 4.2, is also observed in figure 25(*e*,*f*). According to the balance relationship discussed in § 4.2, the pressure diffusion term at the wall should be dominated by Dp_{12}^y ($\partial\overline{p'u''}/\partial y$), consistent with findings by Chan, Schlatter & Chin (2021). To further analyse energy transfer changes at the wall, figure 27 presents the $\overline{p'u''}$ contours under strong and weak interactions. It is evident from figure 27 that $\overline{p'u''}$ is positive near the wall upstream of the shocks but exhibits significant negative values in regions with large gradients, such as shocks and slip lines. Therefore, this sign change in $\overline{p'u''}$ and its wall-normal gradient near the wall is likely due to the incomplete detachment of the shear layer originating from the separation shock foot. Additionally, streamwise velocity reversal and destruction of canonical wall-bounded turbulent structures induced by flow separation near the separation shock foot may further alter the wall-normal energy transfer described by Dp_{12}^y term, ultimately resulting in a positive–negative–positive pattern of Dp_{12}^y along the streamwise direction near the wall, with its balance term Π_{12}^y exhibiting an opposite negative–positive–negative pattern.

This section has identified and compared the key factors responsible for producing and amplifying different stress components, as well as the mechanisms of inter-component energy transfer under both strong and weak interactions. The findings reveal that P_{11}^x and P_{11}^y in $\widetilde{u''u''}$ primarily drive TKE amplification, with excess energy redistributed to other normal stress components via Π. In the $\widetilde{v''v''}$ component, P_{22}^y dominates P_{22}, contributing

https://doi.org/10.1017/jfm.2025.10616 Published online by Cambridge University Press

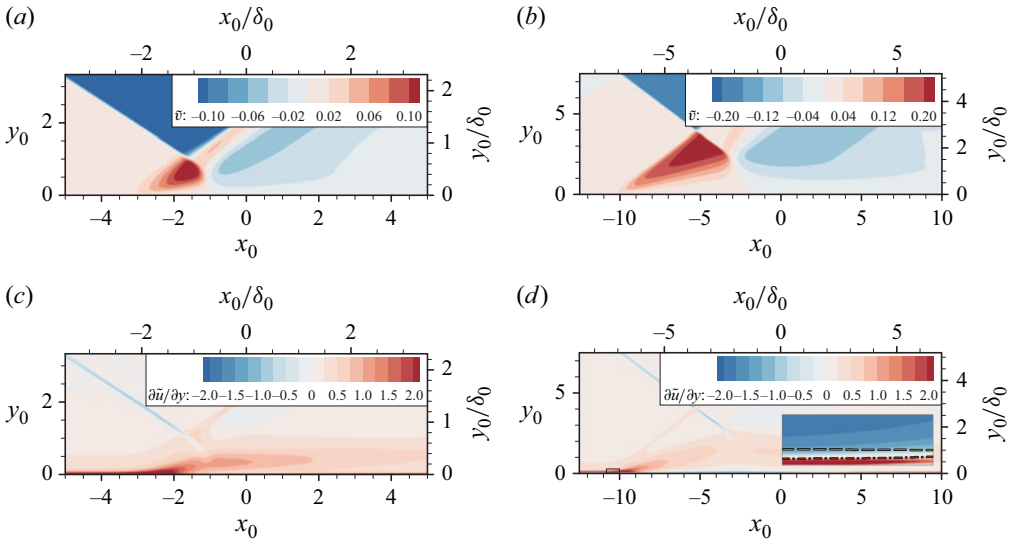


Figure 26. Contours of mean wall-normal velocity (*a*,*b*) and wall-normal gradient of mean streamwise velocity (*c*,*d*) under weak (*a*,*c*) and strong (*b*,*d*) interactions. The enlarged view is redrawn at different level range (0–11) with the $\widetilde{u''u''}$ (-·- dash-dotted line) and $-\widetilde{u''v''}$ (- - - dashed line) peak positions.

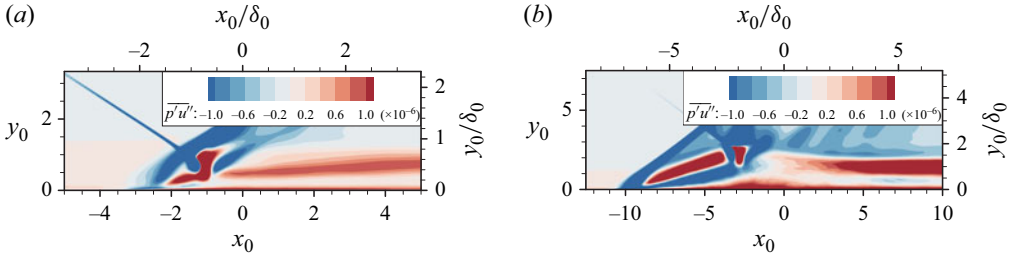


Figure 27. Contours of mean pressure–velocity fluctuation correlation $\overline{p'u''}$ under weak (*a*) and strong (*b*) interactions.

negatively upstream of the incident shock and positively downstream. Meanwhile, P_{33} is negligible. For the $-\widetilde{u''v''}$ component, P_{12} is primarily determined by the negative P_{12}^{x1} and positive P_{12}^{y2}, resulting in a local valley in $-\widetilde{u''v''}$ stress near the incident shock foot. The initial turbulence amplification near the separation shock foot exhibits little difference between strong and weak interactions. The redistribution mechanism allows $\widetilde{u''u''}$ to amplify first, followed by $\widetilde{w''w''}$, while $\widetilde{v''v''}$ amplifies last, possibly due to negative P_{22}^{y}. The amplification of $-\widetilde{u''v''}$ and $\widetilde{u''u''}$ occurs simultaneously due to velocity profile changes induced by the APG, though $-\widetilde{u''v''}$ exhibits a slower initial amplification rate, influenced by $\widetilde{v''v''}$. Additionally, inter-component energy transfer in the inner layer under $y^+ = 10$, as reflected by the Π terms, is almost unaffected by the strength of the incident shock. Instead, the differences between strong and weak interactions primarily stem from the distinct flow evolution processes caused by changes in the scale of the separation zone. In strong interaction, the larger distance between the incident and separation shocks enhances flow dissipation, resulting in the formation of the

https://doi.org/10.1017/jfm.2025.10616 Published online by Cambridge University Press

'oblique platform' and differences in the amplification mechanism for P_{11}^{y}. Furthermore, the increased height of the separation bubble in the wall-normal direction under strong interaction leads to greater flow deflection downstream of the incident shock foot. This deflection promotes a gradual reattachment process downstream, influencing the evolution of the peak height of dominant production terms and Reynolds stresses in the recovery region, resulting in different trends between strong and weak interactions in figure 8. In addition, the enhanced flow deflection near the reattachment point also likely generates compression waves, contributing to the 'secondary amplification' process observed in strong interaction.

5. Spectrum analysis and inter-component energy transfer mechanism

In § 4, the dominant budget terms and associated flow mechanisms responsible for amplifying Reynolds stress components were identified through budget decomposition. While this analysis provides valuable energy information, spectral analysis offers an additional perspective on scale structures, enabling a more comprehensive understanding of the mechanisms driving changes in the scales of inter-component energy transfer during turbulent amplification. Therefore, in this section, spanwise spectra of Reynolds stresses and key budget terms, including production P and pressure-strain Π terms, are computed for both strong and weak interactions. Using the unaveraged Reynolds stress transport equations (4.1), the spanwise spectra of the relevant variables are simply obtained, as expressed in (5.1)

$$\begin{gathered}
\phi_{11}=\frac{\mathrm{Re}\left(\widehat{\sqrt{\rho}u''}\,\widehat{\sqrt{\rho}u''}^{*}\right)}{\overline{\rho}},\quad \phi_{22}=\frac{\mathrm{Re}\left(\widehat{\sqrt{\rho}v''}\,\widehat{\sqrt{\rho}v''}^{*}\right)}{\overline{\rho}},\\
\phi_{33}=\frac{\mathrm{Re}\left(\widehat{\sqrt{\rho}w''}\,\widehat{\sqrt{\rho}w''}^{*}\right)}{\overline{\rho}},\quad \phi_{12}=-\frac{\mathrm{Re}\left(\widehat{\sqrt{\rho}u''}\,\widehat{\sqrt{\rho}v''}^{*}\right)}{\overline{\rho}},\\
\phi_{P_{11}^{x}}=-2\overline{\rho}\phi_{11}\frac{\partial\widetilde{u}}{\partial x},\quad \phi_{P_{11}^{y}}=2\overline{\rho}\phi_{12}\frac{\partial\widetilde{u}}{\partial y},\quad \phi_{P_{22}^{x}}=2\overline{\rho}\phi_{12}\frac{\partial\widetilde{v}}{\partial x},\quad \phi_{P_{22}^{y}}=-2\overline{\rho}\phi_{22}\frac{\partial\widetilde{v}}{\partial y},\\
\phi_{P_{12}^{x1}}=\overline{\rho}\phi_{11}\frac{\partial\widetilde{v}}{\partial x},\quad \phi_{P_{12}^{y1}}=-\overline{\rho}\phi_{12}\frac{\partial\widetilde{v}}{\partial y},\quad \phi_{P_{12}^{x2}}=-\overline{\rho}\phi_{12}\frac{\partial\widetilde{u}}{\partial x},\quad \phi_{P_{12}^{y2}}=\overline{\rho}\phi_{22}\frac{\partial\widetilde{u}}{\partial y},\\
\phi_{\Pi_{11}}=2\mathrm{Re}\left(\widehat{p'}\frac{\widehat{\partial u''}}{\partial x}^{*}\right),\quad \phi_{\Pi_{22}}=2\mathrm{Re}\left(\widehat{p'}\frac{\widehat{\partial v''}}{\partial y}^{*}\right),\quad \phi_{\Pi_{33}}=2\mathrm{Re}\left(\widehat{p'}\frac{\widehat{\partial w''}}{\partial z}^{*}\right),\\
\phi_{\Pi_{12}^{x}}=\mathrm{Re}\left(\widehat{p'}\frac{\widehat{\partial v''}}{\partial x}^{*}\right),\quad \phi_{\Pi_{12}^{y}}=\mathrm{Re}\left(\widehat{p'}\frac{\widehat{\partial u''}}{\partial y}^{*}\right),
\end{gathered}\tag{5.1}$$

where Re denotes the real part, $*$ represents complex conjugation, and $\wedge$ indicates the Fourier transform. Notably, it can be derived from (5.1) that the wavenumber-averaged spectrum over the entire wavenumber space is fully consistent with the time-averaged value of the corresponding variable in physical space.

5.1. *Spectra of Reynolds stresses*

The weighted spanwise spectra of various Reynolds stresses at different streamwise stations during the initial turbulence amplification stage for both strong and weak interactions are calculated using (5.1) and presented in figures 28–31. For clarity, all spectra are normalised by the absolute values of their respective local peaks.

https://doi.org/10.1017/jfm.2025.10616 Published online by Cambridge University Press

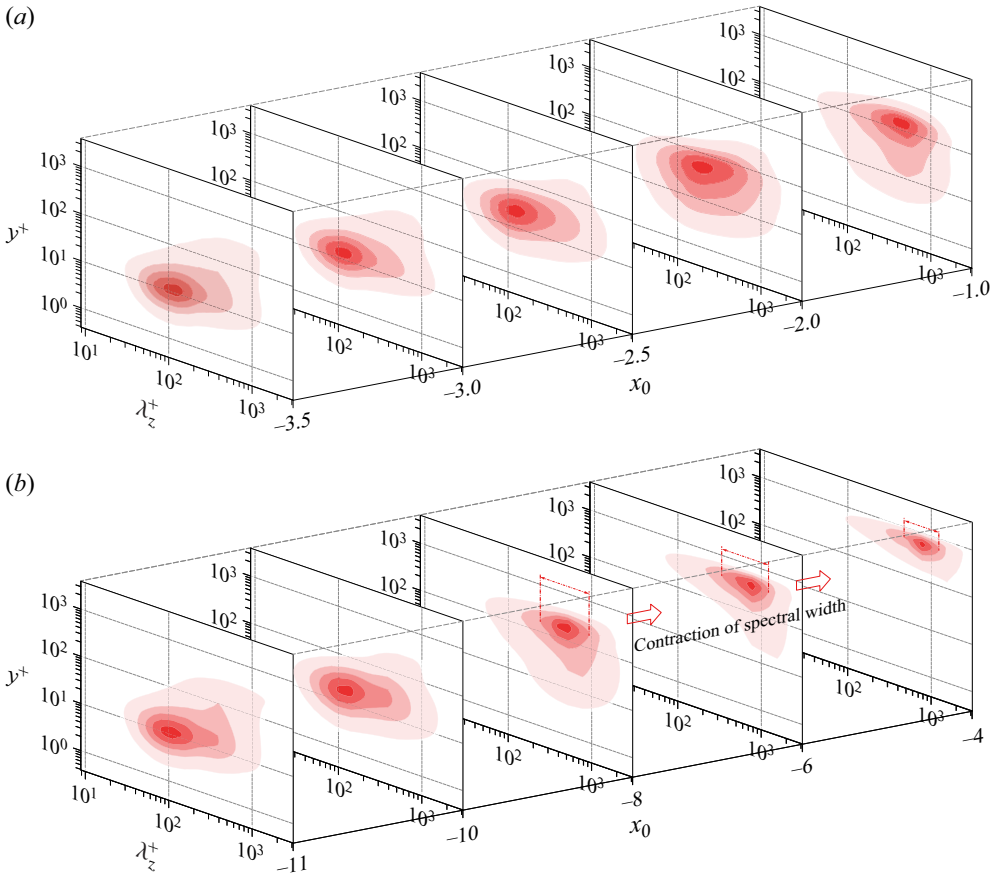


Figure 28. Streamwise evolution of $\widetilde{u''u''}$ weighted spanwise spectra at different stations under weak (*a*) and strong (*b*) interactions. The contour colours, from light to dark, represent 10 %, 30 %, 50 %, 70 % and 90 % of the local peak value.

To further analyse the scale evolution of different stress components during turbulence amplification, figure 32 summarises the streamwise evolution of energy, height and scale at the spectral peaks in figures 28–31.

Upstream of the separation shock, figure 28 reveals that both strong and weak interactions retain the spanwise spectral characteristics of canonical turbulent boundary layers. Specifically, the spectral peak of $\widetilde{u''u''}$ at $\lambda_z^+ \approx 100$ corresponds to the characteristic streaks of wall-bounded turbulence. As the flow crosses the separation shock, turbulence amplification begins, with each stress component exhibiting distinct changes in amplification magnitude, spanwise scale and peak height. For the weak interaction shown in figure 32(*a*,*c*,*e*), the energy, height and scale at the spectral peak of $\widetilde{u''u''}$ increase monotonically along the streamwise direction. In contrast, consistent with the stress peak height evolutions discussed in § 3.2, the spectral peak height of $\widetilde{v''v''}$ decreases significantly after the separation point, accompanied by a reduction in its spectral peak scale. For $\widetilde{w''w''}$, another wall-parallel component the same as $\widetilde{u''u''}$, the spectral peak scale decreases notably upstream of the separation point, while its peak height also slightly decreases. Downstream of the separation point, $\widetilde{w''w''}$ closely follows

https://doi.org/10.1017/jfm.2025.10616 Published online by Cambridge University Press

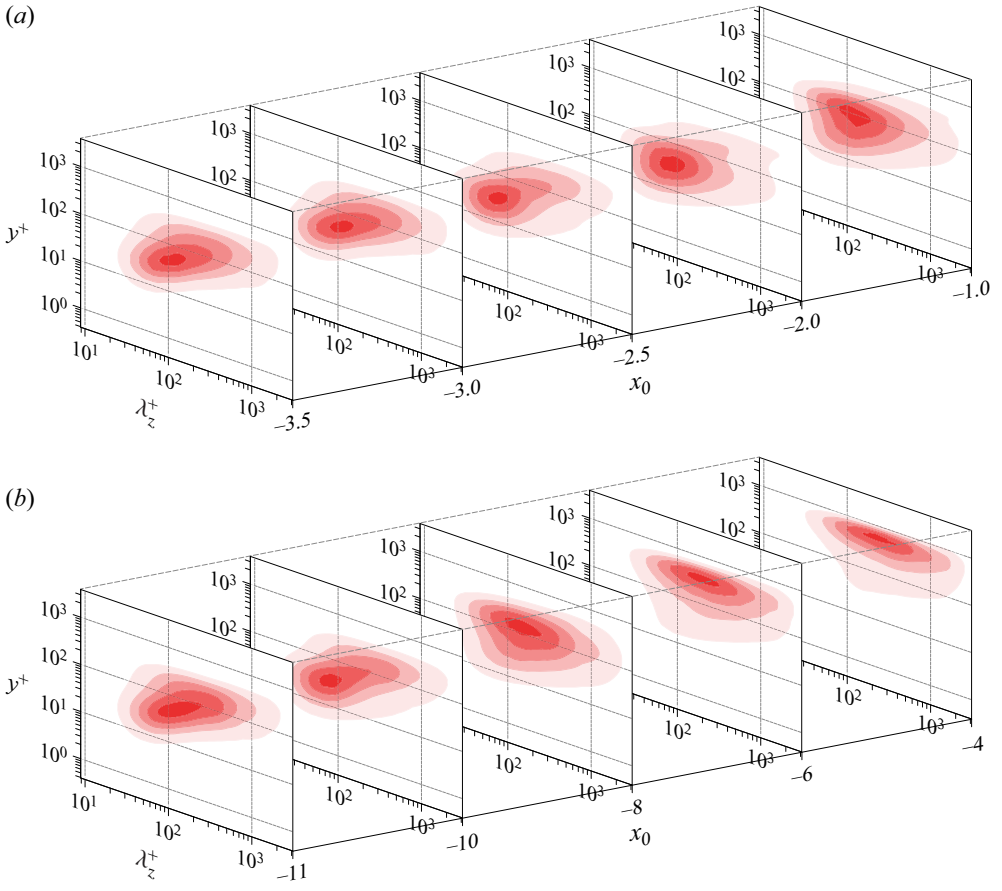


Figure 29. Streamwise evolution of $\widetilde{v''v''}$ weighted spanwise spectra at different stations under weak (*a*) and strong (*b*) interactions. For the legend, see caption of figure 28.

the behaviour of $\widetilde{u''u''}$, with energy, height and scale increasing uniformly, and its plots are closest to those of $\widetilde{u''u''}$ in figure 32(*c*,*e*). As concluded in § 4.4, the amplification of $-\widetilde{u''v''}$ is closely associated with $\widetilde{u''u''}$, and $-\widetilde{u''v''}$ is also an important part of the production term in $\widetilde{u''u''}$. Consequently, as illustrated in figure 32(*a*,*e*), although $-\widetilde{u''v''}$ exhibits smaller energy and scale amplification compared with $\widetilde{u''u''}$, its overall trend remains similar to $\widetilde{u''u''}$, showing monotonic scale amplification.

In strong interaction, the spectral peak energy, scale and height evolve similarly to those in weak interaction, with noticeable decreases in the spectral peak height of $\widetilde{v''v''}$ and the scale of $\widetilde{w''w''}$ near the separation point. This streamwise evolution appears to equalise the height and scale of all stress components during turbulence amplification, potentially related to inter-component energy transfer mechanisms. A more detailed analysis of this phenomenon, incorporating the pressure-strain spectrum, will be presented in § 5.3. Compared with the weak interaction, the strong interaction spectra exhibit larger scales and higher peak heights during turbulence amplification, consistent with the peak value and height evolution trends of stresses in figure 8(*b*). Upstream of the separation shock, the larger spanwise scales in strong interaction may result from the more pronounced unsteady

https://doi.org/10.1017/jfm.2025.10616 Published online by Cambridge University Press

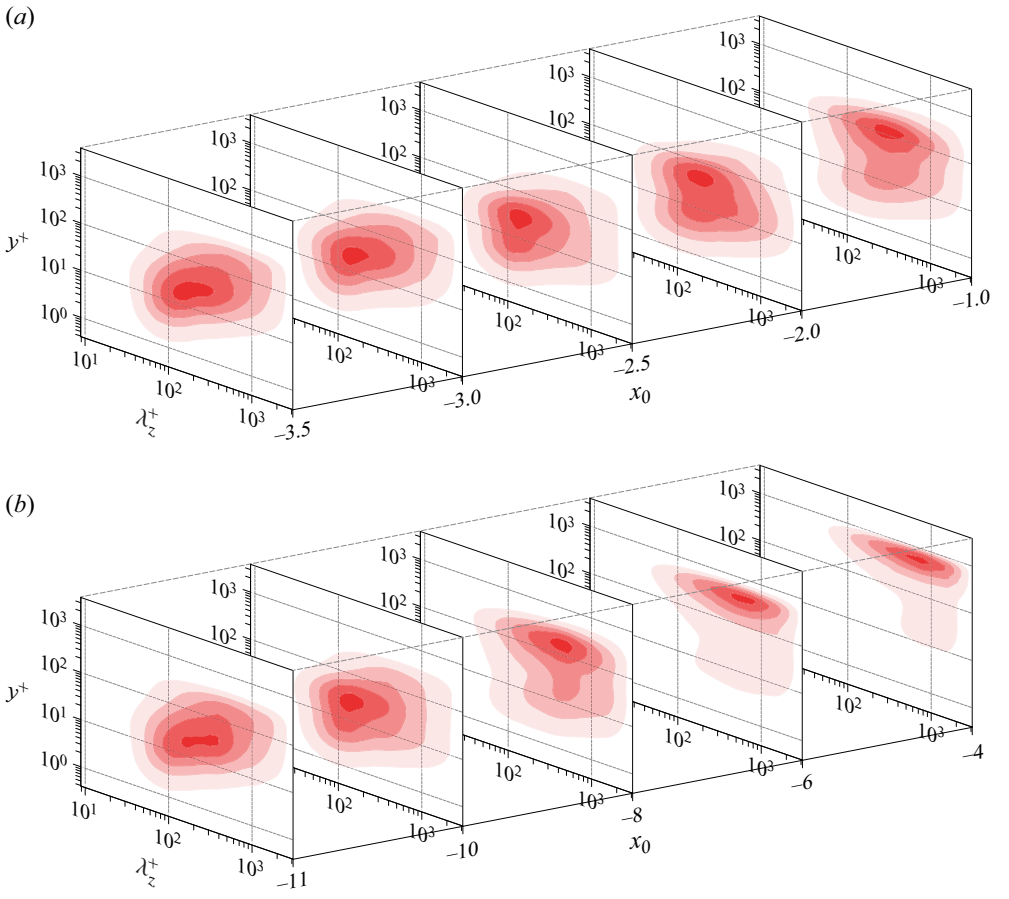


Figure 30. Streamwise evolution of $\widetilde{w''w''}$ weighted spanwise spectra at different stations under weak (*a*) and strong (*b*) interactions. For the legend, see caption of figure 28.

effects of shocks. Unlike the turbulent amplification evolutions shown in figure 8(*d*) of § 3.2, the spectral peak energy does not exhibit a typical 'slope platform' region. This is particularly evident for $\widetilde{v''v''}$ and $\widetilde{u''u''}$, where the spectral peak energy remains nearly constant or even increases in this area. Examining the $\widetilde{u''u''}$ spectrum in figure 28 within the 'slope platform' region reveals that the width of energy above 50 %, 70 % or 90 % of the peak value narrows as the flow evolves downstream. This suggests that, although the peak energy remains relatively unchanged, the overall energy continues to decay, consistent with the turbulence amplification trends discussed in § 3.2. Furthermore, this narrowing of energy width implies that in the 'slope platform' region, where the flow remains undisturbed by shocks, the scales become more concentrated as the flow evolves, promoting the formation of large-scale structures.

Figure 33 presents instantaneous snapshots of streamwise velocity near the peak of TKE. Figure 33(*a*) illustrates that, under weak interaction, velocity streaks of canonical wall-bounded turbulence are observed upstream of the separation shock. The scale of velocity streaks increases noticeably downstream of the separation shock and becomes fully amplified in the downstream recovery zone. In contrast, figure 33(*b*) reveals a slightly different scale evolution of streaks under strong interaction. While canonical velocity

https://doi.org/10.1017/jfm.2025.10616 Published online by Cambridge University Press

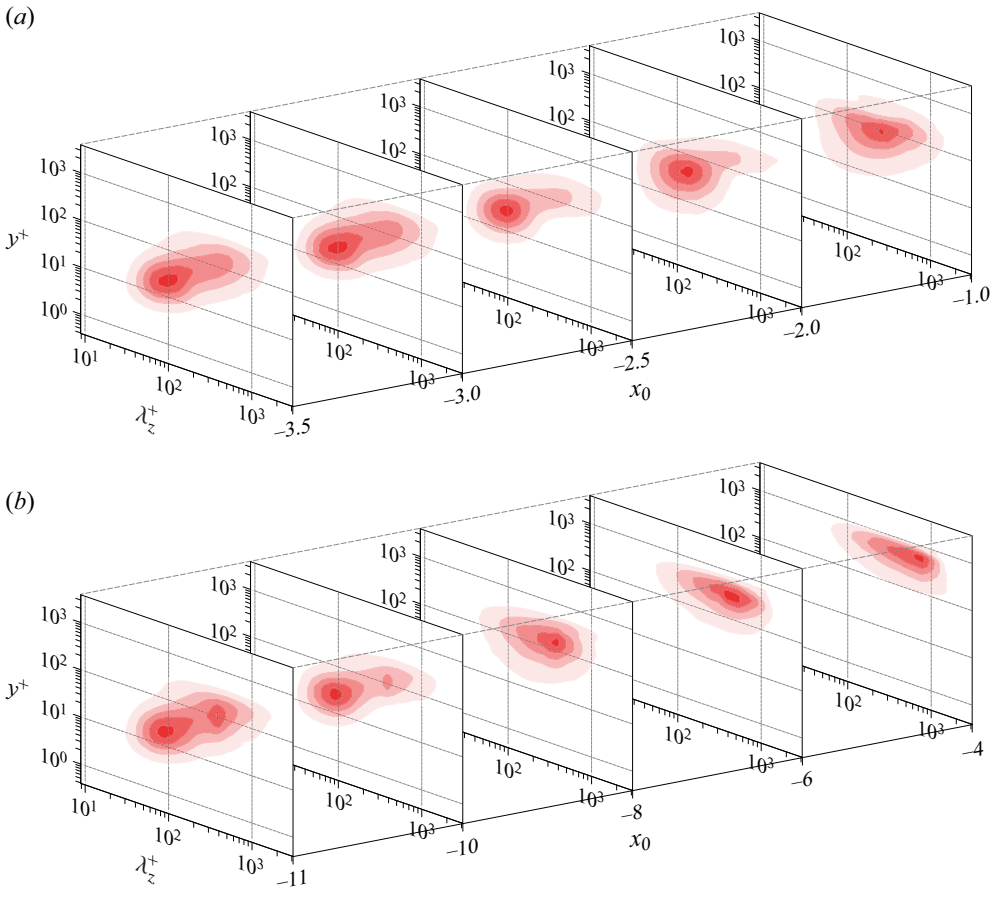


Figure 31. Streamwise evolution of $-\widetilde{u''v''}$ weighted spanwise spectra at different stations under weak (a) and strong (b) interactions. For the legend, see caption of figure 28.

streaks also amplify at the separation shock foot, small-scale structures emerge within the 'slope platform' region, eventually developing into large-scale streaks at the tail of this region. This evolution of velocity streaks confirms the conclusions drawn from the spanwise spectrum analysis. The presence of large-scale streaks upstream of the incident shock may arise from the shock-free, elongated 'slope platform' region, which provides the necessary space for the formation and concentration of large-scale structures.

5.2. *Spectra of production terms*

Building on the Reynolds stress spectra analysis, this study highlights the differences in the evolution of scale structures between strong and weak interactions. Extending this analysis, the spanwise spectra of the dominant production terms are examined in this subsection. The results indicate that, consistent with the findings in § 5.1, the scale of production terms in strong interaction remains larger than in weak interaction. However, the spectral peak evolution trends exhibit no significant differences between the two cases. In both interactions, the scales of the main production terms and their dominant sub-terms exhibit a consistent increasing trend in the streamwise direction, and the energy and height at spectral peaks evolve similarly to the time-averaged results presented in figures 21–24 of § 4.4. For simplicity, only results that deviate from the time-averaged peak value evolution

https://doi.org/10.1017/jfm.2025.10616 Published online by Cambridge University Press

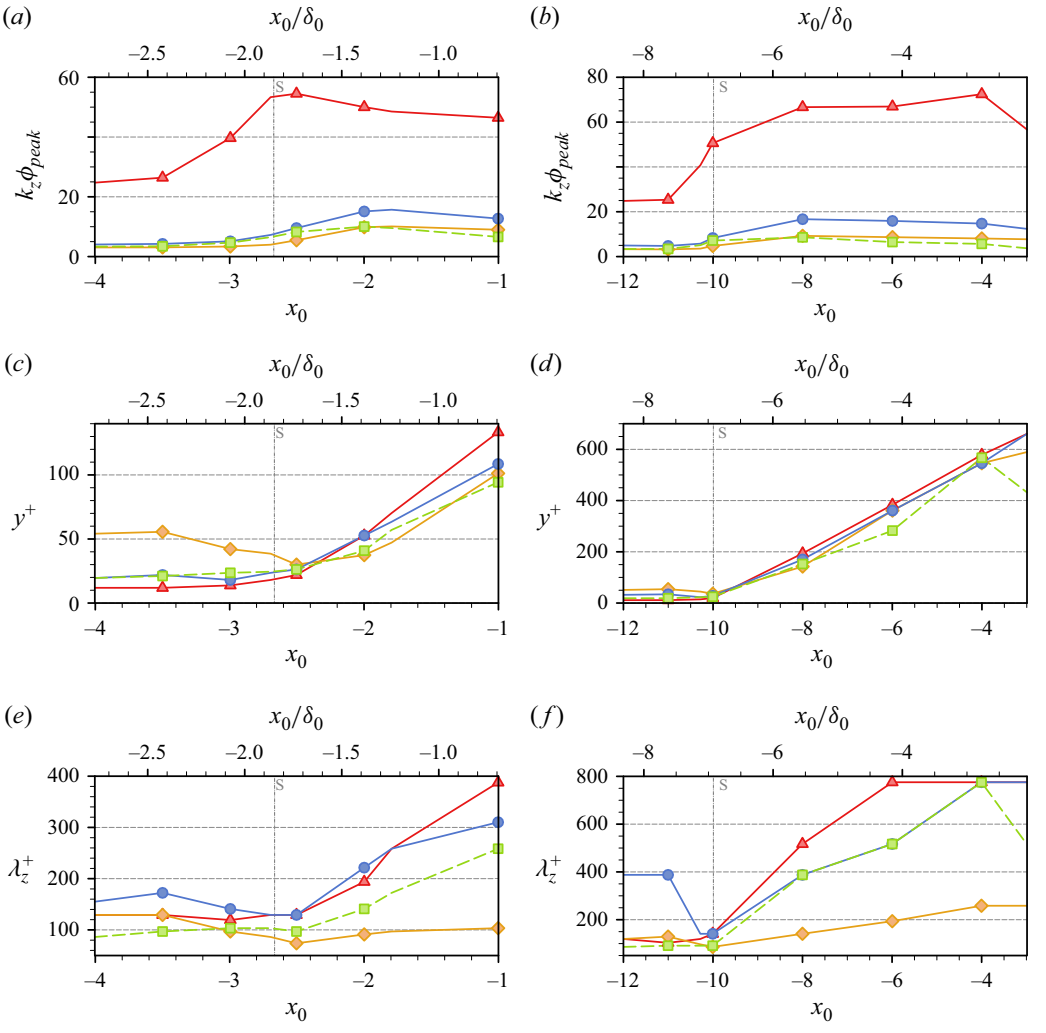


Figure 32. Streamwise evolutions of energy (*a*,*b*), height (*c*,*d*) and scale (*e*,*f*) at spectral peaks for Reynolds stresses $\widetilde{u''u''}$ (—), $\widetilde{v''v''}$ (—), $\widetilde{w''w''}$ (—) and $-\widetilde{u''v''}$ (—) under weak (*a*,*c*,*e*) and strong (*b*,*d*,*f*) interactions. The symbols represent the spectra depicted in figures 28–31.

are provided. Figure 34 illustrates the streamwise evolution of energy, height and scale at the spectral peaks of the principal P_{11} term and its two components, P_{11}^x and P_{11}^y, for both strong and weak interactions.

A comprehensive analysis of figure 34 indicates that both strong and weak interactions share similar evolution trends. During turbulence amplification, the scale and height of P_{11} terms in figure 34(*c–f*) steadily increase along the streamwise direction. However, the distinct production mechanisms of the sub-terms P_{11}^x and P_{11}^y lead to differences in their evolution patterns for height and scale. Downstream of the separation shock, P_{11} evolves closer to P_{11}^y in weak interaction and closer to P_{11}^x in strong interaction. This divergence may stem from the stronger shock in the strong interaction, which intensifies the deceleration effect and enhances the contribution of P_{11}^x. Despite this, spectral peak energy plots in figure 34(*a*, *b*) reveal that P_{11} peaks appear downstream of the separation shock for both interactions, with P_{11}^y dominating this spectral peak. This observation

https://doi.org/10.1017/jfm.2025.10616 Published online by Cambridge University Press

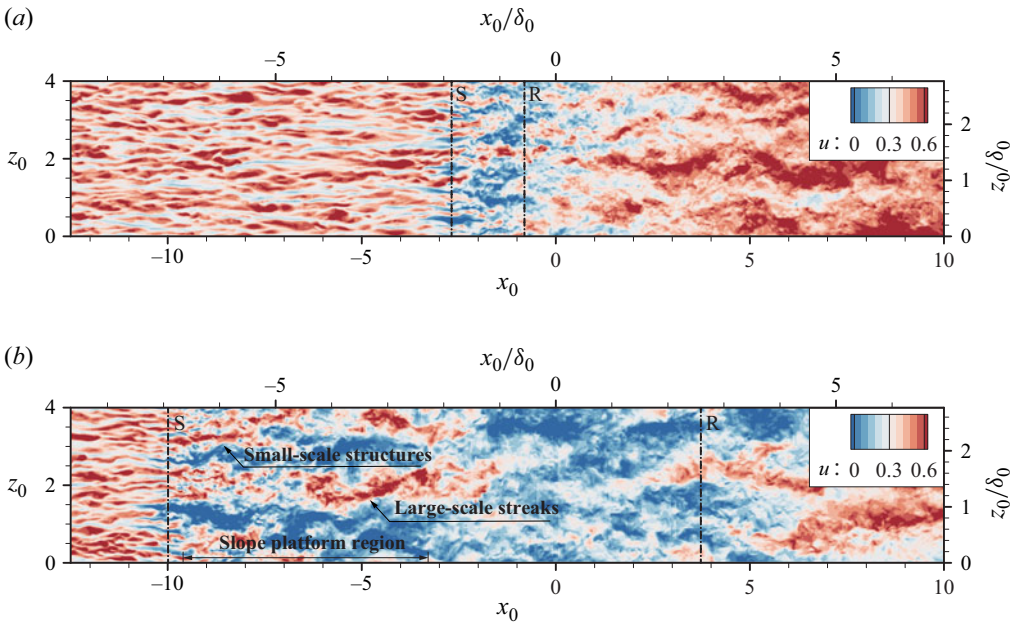


Figure 33. Instantaneous streamwise velocity flow fields near the peak position of TKE under weak (*a*) and strong (*b*) interactions.

appears inconsistent with § 4.4 and Fang *et al.* (2020), which suggest that deceleration primarily drives initial turbulence amplification in low-Reynolds-number simulations. A closer inspection of the flow near the spectral peak of P at $x_0 = -2.5$ in weak interaction provides insight into this discrepancy. As shown in figure 32(*a*), the spectral peak energy of $\widetilde{u''u''}$ at this station is approximately six times that of $-\widetilde{u''v''}$. Although the leading-edge separation shock induces significant deceleration, the streamwise gradient of velocity $\widetilde{u}$ remains more than an order of magnitude smaller than its wall-normal gradient near the boundary layer, numerically explaining the dominance of P_{11}^{y} in spectral peak energy. Further examination of P spectra at the peak station in figure 35 reveals that, while P_{11}^{y} exhibits a higher spectral peak energy, P_{11}^{x} covers a broader range, making P_{11}^{x} more prominent in time-averaged results at the current Reynolds number. Consequently, the total P_{11} spectrum integrates features of both sub-terms, with a peak position resembling P_{11}^{y} and a broader distribution similar to P_{11}^{x}. The sharp peak of P_{11}^{y} and the broader range of P_{11}^{x} stem partially from differences in the spectra of $\widetilde{u''u''}$ and $-\widetilde{u''v''}$, suggesting that turbulence amplification driven by shear effects is more efficient within specific scale ranges, while amplification driven by deceleration has a broader influence across multiple scales. In the self-sustaining cycles of wall-bounded turbulence, mechanisms such as the Orr mechanism, which regenerates streamwise vortices from meandering streaks (Jiménez 2013, 2015; Hwang & Bengana 2016), and the 'lift-up' mechanism, which forms streaks through linear advection of streamwise vortices (Farrell & Ioannou 2012; de Giovanetti *et al.* 2017; Kawata & Tsukahara 2021), both rely on the contribution of mean shear. This close relationship between velocity streaks and shear effects leads this study to conclude that shear-driven amplification, represented by P_{11}^{y}, primarily influences streamwise-elongated streaky structures, while deceleration-driven amplification, represented by P_{11}^{x}, amplifies multi-scale structures within wall-bounded turbulence.

https://doi.org/10.1017/jfm.2025.10616 Published online by Cambridge University Press

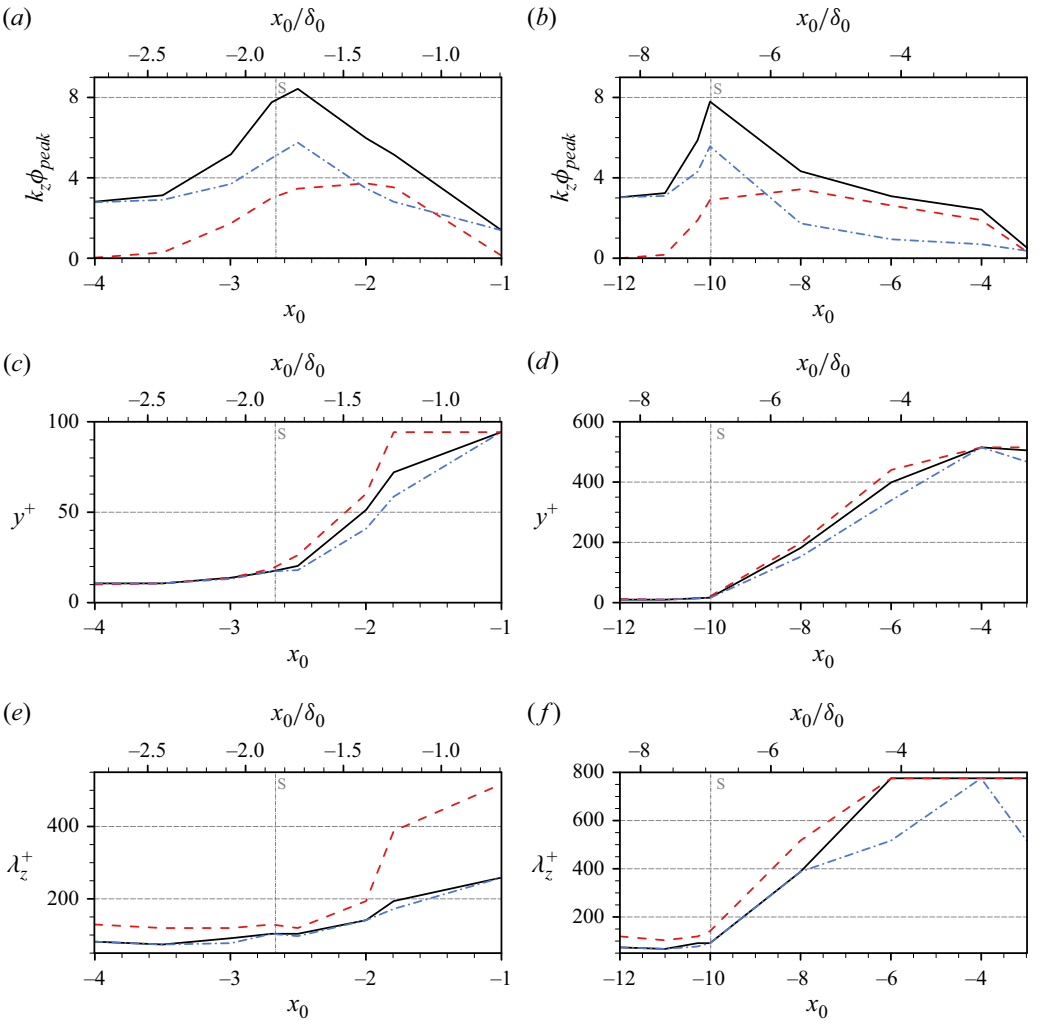


Figure 34. Streamwise evolutions of energy (*a*,*b*), height (*c*,*d*) and scale (*e*,*f*) at spectral peaks for production terms P_{11} (black solid line), P_{11}^x (- - - dashed line) and P_{11}^y (–·– dash-dotted line) under weak (*a*,*c*,*e*) and strong (*b*,*d*,*f*) interactions.

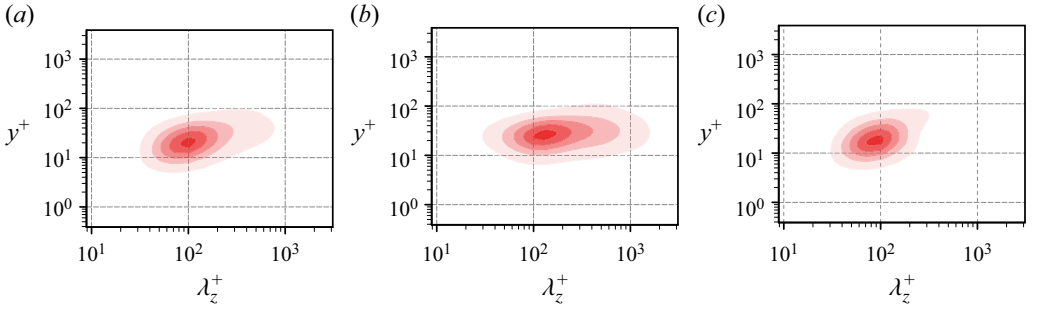


Figure 35. Weighted spanwise spectra of production terms P_{11} (*a*), P_{11}^x (*b*) and P_{11}^y (*c*) at $x_0 = -2.5$ under weak interactions. For the legend, see caption of figure 28.

https://doi.org/10.1017/jfm.2025.10616 Published online by Cambridge University Press

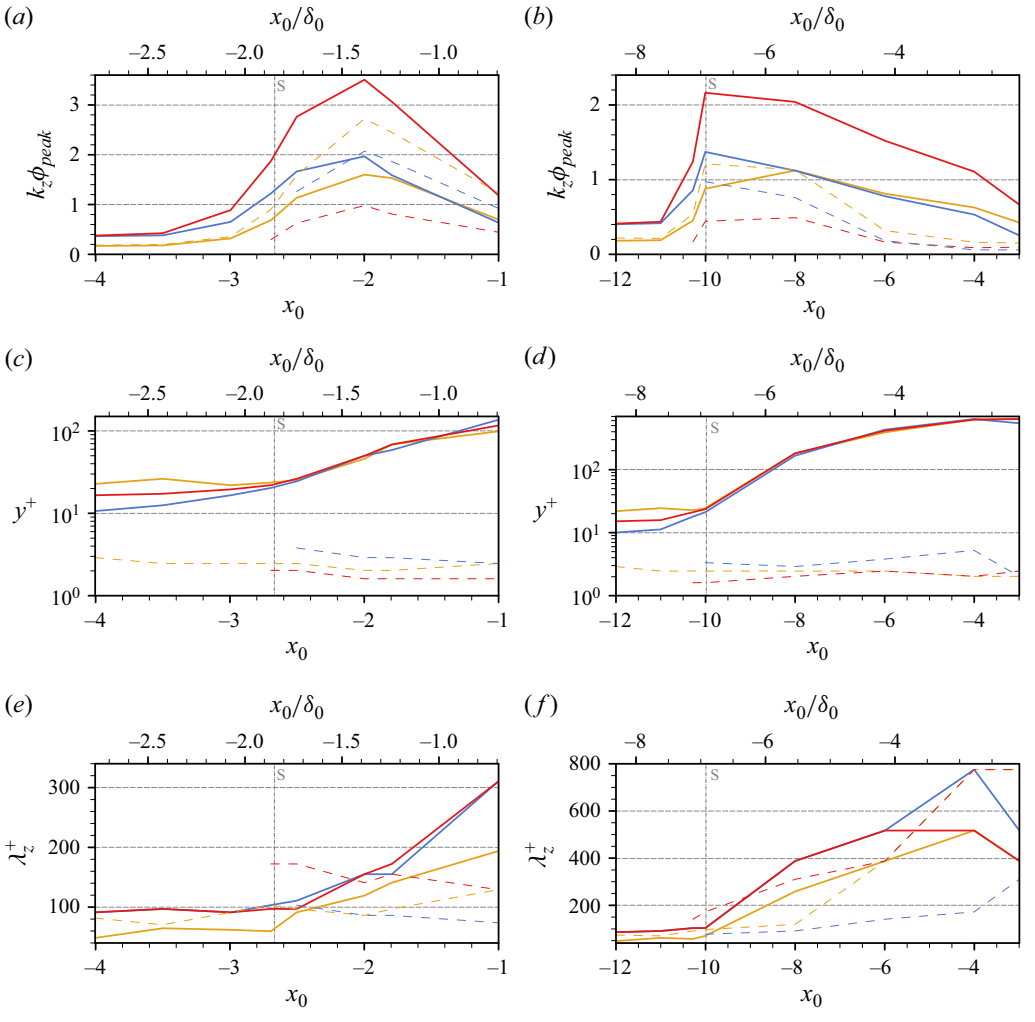


Figure 36. Streamwise evolutions of energy (*a*,*b*), height (*c*,*d*) and scale (*e*,*f*) at spectral peaks for pressure-strain terms Π_{11} (- - -), Π_{22} (- - -) and Π_{33} (- - -) under weak (*a*,*c*,*e*) and strong (*b*,*d*,*f*) interactions. Solid lines represent the outer peak, while dashed lines denote the inner peak.

5.3. *Spectra of pressure-strain term*

The pressure-strain term governs the energy transfer between normal stresses and serves as the amplification source for some stress components. Therefore, unlike the previously discussed Reynolds stresses and production terms, the spectra of the pressure-strain term can exhibit opposing signs at different heights within the same streamwise station, leading to the emergence of double peaks. Figure 36 presents the evolution of energy, height and scale at the spectral peaks of each pressure-strain term under strong and weak interactions during the initial amplification stage. Solid lines indicate the outer peak, while dashed lines represent the inner peak. To ensure consistency in comparison, the peak energy values are presented as absolute magnitudes, regardless of their original sign.

According to the analysis in § 4.1, the energy of the pressure-strain terms for normal stresses originates from the P_{11} of $\widetilde{u''u''}$. Figure 36 reveals that the evolution of the outer peaks of the pressure-strain terms follows a similar pattern to the P terms, with

https://doi.org/10.1017/jfm.2025.10616 Published online by Cambridge University Press

both strong and weak interactions exhibiting gradual increases in height and scale during the initial amplification stage. Although the inner peak height remains nearly identical between strong and weak interactions, the inner peak scale increases steadily under strong interaction, in contrast to weak interaction, where the inner peak scale remains nearly constant along the streamwise direction. This discrepancy may result from the extended plateau in strong interaction allowing for more sufficient development of inner-layer structures, the larger separation zone leading to an increase in inner-layer scale or the influence of larger-scale structures in the outer region under strong interaction leaving 'footprints' on the inner region. Nonetheless, the pressure-strain spectra during the initial amplification near the separation shock foot still behave similarly for both interactions. Given that the peak evolution trends of the mean Reynolds stresses in § 3.2 align completely during the initial amplification stages of strong and weak interactions, figure 37 presents the spanwise pressure-strain spectra of the normal stress components at several representative stations under weak interaction for clarity and conciseness.

Comparing the pressure-strain spectra of various stress components in figure 37 reveals that at $x_0 = -2.5$ for weak interaction, an inner peak gradually emerges in Π_{33}, with its height and scale closely matching those of Π_{22} at $x_0 = -2.5$ to -2. This indicates that energy is primarily transferred from $\widetilde{v''v''}$ to $\widetilde{w''w''}$ in the inner region at the initial amplification process, consistent with the conclusions drawn from the stress component budgets in § 4.2. For the outer peaks, the peak heights, scales and overall shapes of Π_{33} and Π_{11} are relatively consistent, but Π_{22} shows a noticeable difference in scale compared with Π_{11}. This suggests that during the initial turbulence amplification stage, $\widetilde{u''u''}$ primarily transfers energy to $\widetilde{w''w''}$ through the pressure-strain term, which explains the earlier amplification of $\widetilde{w''w''}$ relative to $\widetilde{v''v''}$ from a scale perspective.

Based on the spectral contours in figure 37 and the preceding analysis, it can be concluded that energy transfer is characterised by consistency in height and scale. Moreover, the streamwise evolution of the pressure-strain spectra, along with the spanwise spectra of production terms and Reynolds stresses in figures 32, 34 and 36, demonstrates a delay in scale amplification relative to energy amplification, consistent with the results in Yu *et al.* (2022). Therefore, employing the evolution of stress spectra under weak interaction in figure 32 for illustration, the inter-component energy transfer mechanism during the initial turbulence amplification of SWTBLI can be revealed from a scale perspective. Specifically, although the energy of $\widetilde{u''u''}$ is initially amplified due to the continuous deceleration effect of the separation shock or compression waves at $x_0 = -3.5$, its spectral height and scale remain consistent with those of canonical turbulence due to the delayed amplification of these characteristics. Until approximately $x_0 = -3$, to achieve energy balance, $\widetilde{u''u''}$ transfers its excessively amplified energy to other components through the pressure-strain term, leading to subsequent amplifications in spectral height and scale. Downstream of this station, the wall-normal and spanwise stresses are influenced by the energy transfer from $\widetilde{u''u''}$, resulting in changes in their spectral peak heights. The peak height of $\widetilde{w''w''}$ decreases to approach that of $\widetilde{u''u''}$, accompanied by a reduction in scale. Since the characteristic scale of $\widetilde{w''w''}$ in canonical turbulence is larger than $\widetilde{u''u''}$, this reduction aligns their scales. Meanwhile, $\widetilde{v''v''}$ also experiences a similar decrease in spectral peak height and scale. However, the scale reduction in $\widetilde{v''v''}$ increases the scale disparity between $\widetilde{u''u''}$ and $\widetilde{v''v''}$, since their characteristic scales are naturally closer in canonical turbulence. Therefore, during the

https://doi.org/10.1017/jfm.2025.10616 Published online by Cambridge University Press

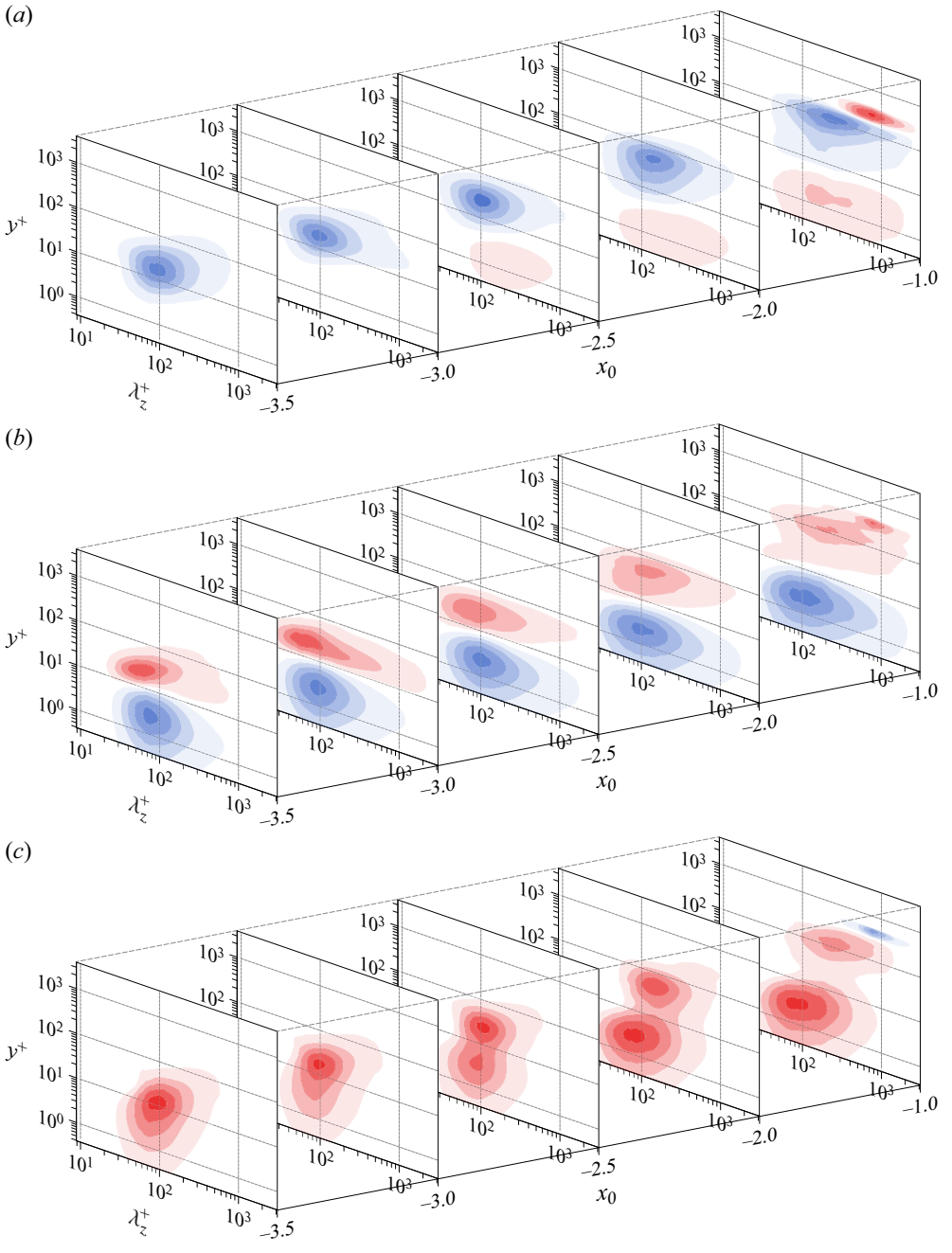


Figure 37. Streamwise evolution of Π_{11} (*a*), Π_{22} (*b*) and Π_{33} (*c*) weighted spanwise spectra at different stations under weak interaction. The contour colours, from light to dark, represent 10 %, 30 %, 50 %, 70 % and 90 % of the local peak value, with — for positive and — for negative peaks.

initial turbulence amplification near the separation shock foot, the spectral peak height and scale of $\widetilde{w''w''}$ become more aligned with those of $\widetilde{u''u''}$, while $\widetilde{v''v''}$ diverges further in characteristic scale from $\widetilde{u''u''}$. This suggests that energy from $\widetilde{u''u''}$ is primarily

https://doi.org/10.1017/jfm.2025.10616 Published online by Cambridge University Press

transferred to $\widetilde{w''w''}$ first from a scale perspective, resulting in the earlier amplification of $\widetilde{w''w''}$ compared with $\widetilde{v''v''}$.

To summarise the discussion in this section, spanwise spectrum analysis reveals that under strong interaction, the streamwise stress spectrum becomes progressively concentrated along the 'slope platform' region, corresponding to the gradual formation of uniform large-scale streaks. In addition, deceleration effects influence structures across a broader range of scales, whereas shear effects primarily act on specific scales, amplifying particular structures such as velocity streaks more effectively. Furthermore, it is found that the characteristic of energy transfer necessitates the consistency of height and scale. As energy is redistributed from $\widetilde{u''u''}$, the peak heights of $\widetilde{w''w''}$ and $\widetilde{v''v''}$ gradually approach that of $\widetilde{u''u''}$. However, this height decrease leads to a corresponding reduction in scale, increasing the scale disparity between $\widetilde{u''u''}$ and $\widetilde{v''v''}$. This process facilitates the transfer of more energy to $\widetilde{w''w''}$ through the pressure-strain term, explaining its upstream amplification relative to $\widetilde{v''v''}$ from a scale perspective.

6. Conclusion

This study conducts a comparative DNS analysis of OSWTBLI at strong (37°) and weak (33.2°) incident angles to investigate turbulence amplification and inter-component energy transfer in SWTBLI. Time-averaged results indicate that strong interactions significantly enlarge the separation bubble, particularly in the wall-normal direction, increasing the distance between the incident and separation shocks. This expansion allows the detached shear layer to develop more fully, leading to a distinct streamwise turbulence evolution path compared with weak interactions.

Analysis of Reynolds stress contours and peak evolution reveals key differences in amplification mechanisms. Under weak interaction, normal stresses peak sharply downstream of the separation shock foot before rapidly decaying. In contrast, strong interaction exhibits a 'slope platform' region with a nearly uniform decay rate, followed by a stepped decay near the incident shock foot and a unique 'secondary amplification' in the recovery region. However, during the initial amplification stage, where the influence of the separation bubble is negligible, the initial amplifications near the separation shock foot follow an identical sequence in both cases: $\widetilde{u''u''}$, $\widetilde{w''w''}$ then $\widetilde{v''v''}$. The shear stress $-\widetilde{u''v''}$ amplifies alongside $\widetilde{u''u''}$ at a lower rate initially but accelerates later when $\widetilde{v''v''}$ begins to amplify.

The TKE budget and spanwise spectrum analyses clarify these mechanisms. The budget analysis identifies the production term of $\widetilde{u''u''}$ as the primary driver of turbulence amplification, with the deceleration effect dominating upstream of the incident shock and the shear effect contributing along the shear layer. In strong interaction, the increased distance between the separation and incident shocks creates a shock-free region where the dominant contribution terms of each stress component exhibit stable dissipation, forming the 'slope platform.' Downstream, amplification patterns resemble those near the separation shock, with intensified diffusion, dissipation and production terms, validating that 'secondary amplification' may arise from increased shear layer instability and deceleration effect caused by intermittently travelling reattachment compression waves. The budget analysis further confirms that $\widetilde{u''u''}$ and $-\widetilde{u''v''}$ amplification is driven by their production terms, while $\widetilde{w''w''}$ and $\widetilde{v''v''}$ rely on energy transfer from $\widetilde{u''u''}$ via the pressure-strain term, causing $\widetilde{u''u''}$ and $-\widetilde{u''v''}$ to amplify upstream. The production term

https://doi.org/10.1017/jfm.2025.10616 Published online by Cambridge University Press

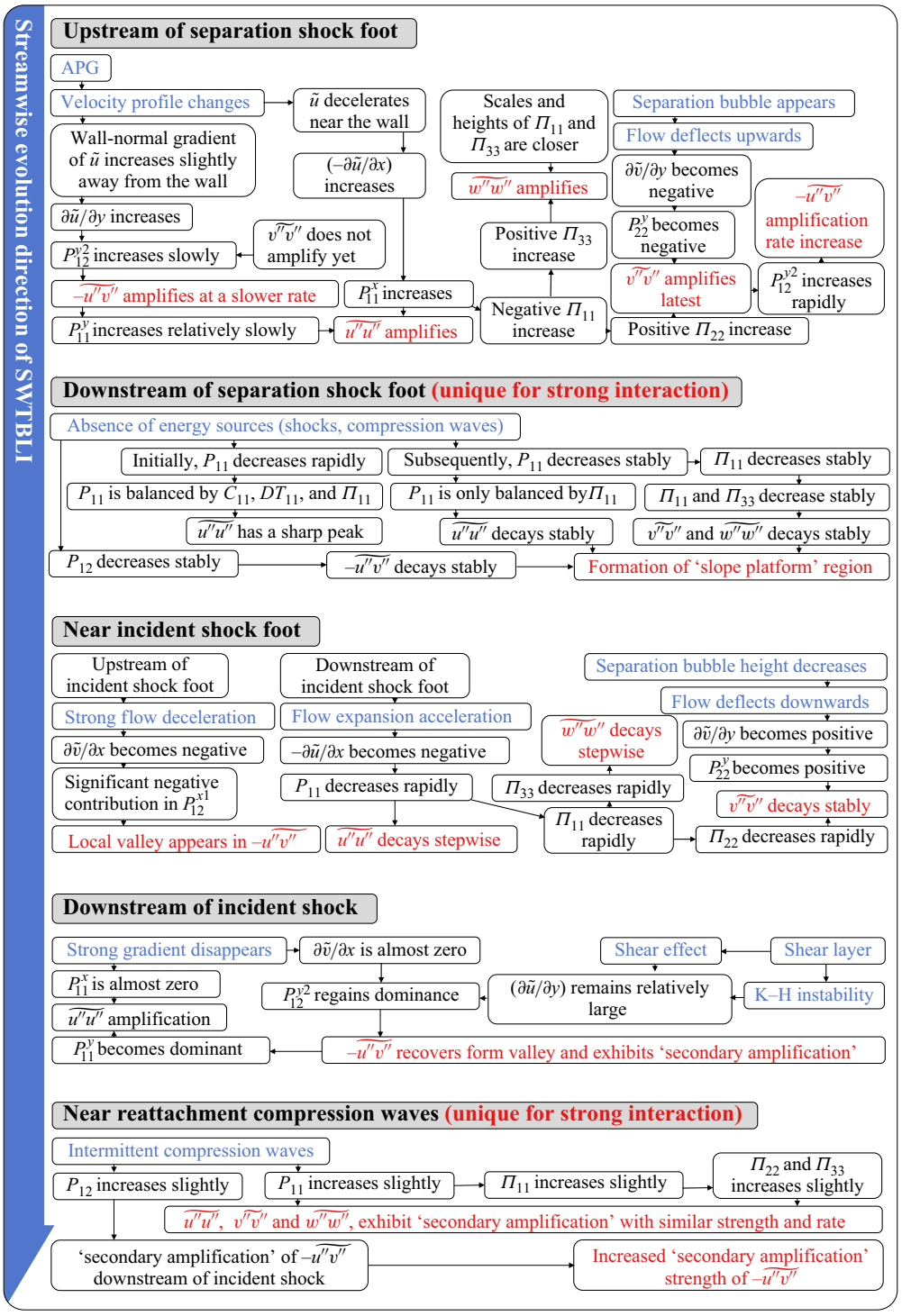


Figure 38. Schematic of detailed turbulence amplification mechanism in SWTBLI.

https://doi.org/10.1017/jfm.2025.10616 Published online by Cambridge University Press

of $\widetilde{v''v''}$ contributes positively downstream of the incident shock foot due to deceleration of wall-normal velocity, reducing its decay rate in peak evolution. Upstream, acceleration of wall-normal velocity acts as a negative contribution, delaying amplification, which partially explain why $\widetilde{v''v''}$ amplifies later than $\widetilde{w''w''}$. For $-\widetilde{u''v''}$, whose production term includes the $\widetilde{v''v''}$ term, amplification is initially slow due to delayed $\widetilde{v''v''}$, accelerating only after $\widetilde{v''v''}$ increases.

Spanwise spectra further clarify inter-component energy transfer and scale evolution in turbulence amplification. In strong interactions, the 'slope platform' region exhibits stable spectral peak energy for each stress component, with the decay of their total energy reflected in spectral width contraction. This suggests that the scale of flow structures becomes increasingly uniform as the flow develops, corresponding to the gradual formation of large-scale velocity streaks. In addition, the spectral peak of the production term is dominated by the shear effect, while the deceleration effect influences a broader spectrum and contributes more to total energy. This indicates that the shear effect primarily targets specific scale structures, such as streaks, whereas the deceleration effect affects a wider range of multi-scale wall-bounded turbulence structures. The evolution of pressure-strain and stress spectra further reveals that energy amplification often precedes scale amplification, and the energy transfer process requires consistency in both height and scale of different components. During the initial turbulence amplification stage, influenced by energy transferred from the $\widetilde{u''u''}$ component, the peak heights of the other normal stresses $\widetilde{v''v''}$ and $\widetilde{w''w''}$, which are originally higher than $\widetilde{u''u''}$ in canonical boundary layers, exhibit varying degrees of decrease. This reduction in peak heights leads to contractions of local scales for $\widetilde{v''v''}$ and $\widetilde{w''w''}$, bringing the scales of $\widetilde{w''w''}$ and $\widetilde{u''u''}$ closer while increasing the scale disparity between $\widetilde{v''v''}$ and $\widetilde{u''u''}$. Ultimately, $\widetilde{u''u''}$ transfers more energy to $\widetilde{w''w''}$ via the pressure-strain term, which may fundamentally explain why $\widetilde{w''w''}$ amplifies earlier than $\widetilde{v''v''}$.

In conclusion, by comparing strong and weak interactions, this study offers a comprehensive analysis of initial turbulence amplification near the separation shock foot, the stepped turbulence decay at the incident shock foot as well as the unique 'slope platform' region and 'secondary amplification' process in strong interactions. These novel findings provide a detailed depiction of the turbulence amplification mechanism in SWTBLI, as illustrated in figure 38. Nevertheless, further investigations are necessary to incorporate additional influences, such as wall temperature and Reynolds-number effects. Furthermore, this study examines the influence range of shear and deceleration effects in space and scale, and innovatively uncovers the inter-component energy transfer during the initial turbulence amplification stage from the perspectives of energy, position and scale, which may provide theoretical support for developing advanced flow control strategies.

Acknowledgements. The authors would like to acknowledge Professor X. Li (Institute of Mechanics, Chinese Academy of Sciences) for the DNS code OpenCFD-SC. All authors are thankful to the anonymous reviewers for the constructive comments.

Funding. This research study is supported by the National Natural Science Foundation of China (Nos. 92252201, 52272378 and 11972308) and the Academic Excellence Foundation of BUAA for PhD Students.

Declaration of interests. The authors report no conflict of interest.

https://doi.org/10.1017/jfm.2025.10616 Published online by Cambridge University Press

References

Adams, N.A. 1998 Direct numerical simulation of turbulent compression ramp flow. *Theor. Comput. Fluid Dyn.* **12** (2), 109–129.

Adams, N.A. 2000 Direct simulation of the turbulent boundary layer along a compression ramp at M = 3 and $Re_\theta = 1685$. *J. Fluid Mech.* **420**, 47–83.

Andreopoulos, Y., Agui, J.H. & Briassulis, G. 2000 Shock wave—turbulence interactions. *Annu. Rev. Fluid Mech.* **32** (2000), 309–345.

Aubard, G., Gloerfelt, X. & Robinet, J.C. 2013 Large-eddy simulation of broadband unsteadiness in a shock/Boundary-layer interaction. *AIAA J.* **51** (10), 2395–2409.

Babinsky, H. & Harvey, J.K. 2011 *Shock Wave-Boundary-Layer Interactions*. Cambridge University Press.

Bernardini, M., Asproulias, I., Larsson, J., Pirozzoli, S. & Grasso, F. 2016 Heat transfer and wall temperature effects in shock wave turbulent boundary layer interactions. *Phys. Rev. Fluids* **1** (8), 084403.

Bernardini, M., Della Posta, G., Salvadore, F. & Martelli, E. 2023 Unsteadiness characterisation of shock wave/turbulent boundary-layer interaction at moderate Reynolds number. *J. Fluid Mech.* **954**, A43.

Chan, C.I., Schlatter, P. & Chin, R.C. 2021 Interscale transport mechanisms in turbulent boundary layers. *J. Fluid Mech.* **921**, A13.

Cho, M., Hwang, Y. & Choi, H. 2018 Scale interactions and spectral energy transfer in turbulent channel flow. *J. Fluid Mech.* **854**, 474–504.

Clark, T.T. 2020 Two-point evolution equations for incompressible variable density turbulence. arXiv:2011.03345

Dolling, D.S. 2001 Fifty years of shock-wave/Boundary-layer interaction research: what next? *AIAA J.* **39** (8), 1517–1531.

Dolling, D.S. & Murphy, M.T. 1983 Unsteadiness of the separation shock wave structure in a supersonic compression ramp flowfield. *AIAA J.* **21** (12), 1628–1634.

Dupont, P., Piponniau, S. & Dussauge, J.P. 2019 Compressible mixing layer in shock-induced separation. *J. Fluid Mech.* **863**, 620–643.

Dupont, P., Piponniau, S., Sidorenko, A. & Debiève, J.F. 2008 Investigation by particle image velocimetry measurements of oblique shock reflection with separation. *AIAA J.* **46** (6), 1365–1370.

Délery, J. & Dussauge, J.-P. 2009 Some physical aspects of shock wave/boundary layer interactions. *Shock Waves* **19** (6), 453–468.

Elsberry, K., Loeffler, J., Zhou, M.D. & Wygnanski, I. 2000 An experimental study of a boundary layer that is maintained on the verge of separation. *J. Fluid Mech.* **423**, 227–261.

Fang, J., Zheltovodov, A.A., Yao, Y., Moulinec, C. & Emerson, D.R. 2020 On the turbulence amplification in shock-wave/turbulent boundary layer interaction. *J. Fluid Mech.* **897**, A32.

Farrell, B.F. & Ioannou, P.J. 2012 Dynamics of streamwise rolls and streaks in turbulent wall-bounded shear flow. *J. Fluid Mech.* **708**, 149–196.

Gadd, G.E., Holder, D.W., Regan, J.D. & Bullard, E.C. 1954 An experimental investigation of the interaction between shock waves and boundary layers. *Proc. R. Soc. Lond. A* **226** (1165), 227–253.

Gaitonde, D.V. 2015 Progress in shock wave/boundary layer interactions. *Prog. Aerosp. Sci.* **72**, 80–99.

de Giovanetti, M., Sung, H.J. & Hwang, Y. 2017 Streak instability in turbulent channel flow: the seeding mechanism of large-scale motions. *J. Fluid Mech.* **832**, 483–513.

Gross, A., Little, J. & Fasel, H.F. 2022 Numerical investigation of unswept and swept turbulent shock-wave boundary layer interactions. *Aerosp. Sci. Technol.* **123**, 107455.

Gungor, T.R., Maciel, Y. & Gungor, A.G. 2022 Energy transfer mechanisms in adverse pressure gradient turbulent boundary layers: production and inter-component redistribution. *J. Fluid Mech.* **948**, A5.

Hamilton, J.M., Kim, J. & Waleffe, F. 1995 Regeneration mechanisms of near-wall turbulence structures. *J. Fluid Mech.* **287**, 317–348.

Helm, C.M., Martín, M.P. & Williams, O.J.H. 2021 Characterization of the shear layer in separated shock/turbulent boundary layer interactions. *J. Fluid Mech.* **912**, A7.

Huang, W., Wu, H., Yang, Y.-G., Yan, L. & Li, S.-B. 2020 Recent advances in the shock wave/boundary layer interaction and its control in internal and external flows. *Acta Astronaut.* **174**, 103–122.

Hung, F.T., Greenschlag, S.N. & Scottoline, C.A. 1977 Shock-wave-boundary-layer interaction effects on aerodynamic heating. *J. Spacecr. Rockets* **14** (1), 25–31.

Hwang, Y. & Bengana, Y. 2016 Self-sustaining process of minimal attached eddies in turbulent channel flow. *J. Fluid Mech.* **795**, 708–738.

Hwang, Y. & Cossu, C. 2010 Self-sustained process at large scales in turbulent channel flow. *Phys. Rev. Lett.* **105** (4), 044505.

Hwang Y. & Cossu C. 2011 Self-sustained processes in the logarithmic layer of turbulent channel flows. *Phys. Fluids* **23** (6), 061702.

https://doi.org/10.1017/jfm.2025.10616 Published online by Cambridge University Press

JIMÉNEZ J. 2013 How linear is wall-bounded turbulence? *Phys. Fluids* **25** (11), 110814.
JIMÉNEZ J. 2015 Direct detection of linearized bursts in turbulence. *Phys. Fluids* **27** (6), 065102.
JIMÉNEZ, J. & PINELLI, A. 1999 The autonomous cycle of near-wall turbulence. *J. Fluid Mech.* **389**, 335–359.
KANG Y. & LEE S. 2024 Direct numerical simulation of turbulence amplification in a strong shock-wave/turbulent boundary layer interaction. *Phys. Fluids* **36** (1), 016127.
KAWATA, T. & TSUKAHARA, T. 2021 Scale interactions in turbulent plane couette flows in minimal domains. *J. Fluid Mech.* **911**, A55.
KIM, H.T., KLINE, S.J. & REYNOLDS, W.C. 1971 The production of turbulence near a smooth wall in a turbulent boundary layer. *J. Fluid Mech.* **50** (1), 133–160.
KLINE, S.J., REYNOLDS, W.C., SCHRAUB, F.A. & RUNSTADLER, P.W. 1967 The structure of turbulent boundary layers. *J. Fluid Mech.* **30** (4), 741–773.
KLINE, S.J. & RUNSTADLER, P.W. 1959 Some preliminary results of visual studies of the flow model of the wall layers of the turbulent boundary layer. *J. Appl. Mech.* **26** (2), 166–170.
LAGUARDA, L., HICKEL, S., SCHRIJER, F.F.J. & VAN OUDHEUSDEN, B.W. 2024 Reynolds number effects in shock-wave/turbulent boundary-layer interactions. *J. Fluid Mech.* **989**, A20.
LEE, J.-H. & SUNG, H.J. 2009 Structures in turbulent boundary layers subjected to adverse pressure gradients. *J. Fluid Mech.* **639**, 101–131.
LEE, M. & MOSER, R.D. 2019 Spectral analysis of the budget equation in turbulent channel flows at high Reynolds number. *J. Fluid Mech.* **860**, 886–938.
LI, X., FU, D. & MA, Y. 2008 Direct numerical simulation of hypersonic boundary layer transition over a blunt cone. *AIAA J.* **46** (11), 2899–2913.
LI, X.-L., FU, D.-X., MA, Y.-W. & LIANG, X. 2010 Direct numerical simulation of compressible turbulent flows. *Acta Mechanica Sin.* **26** (6), 795–806.
LIANG, X.& LI, X.L. 2013 DNS of a spatially evolving hypersonic turbulent boundary layer at Mach 8. *Sci. China Phys. Mech. Astron.* **56** (7), 1408–1418.
LONGO, J.M.A. 2003 Aerothermodynamics – a critical review at DLR. *Aerosp. Sci. Technol.* **7** (6), 429–438.
MANSOUR, N.N., KIM, J. & MOIN, P. 1988 Reynolds-stress and dissipation-rate budgets in a turbulent channel flow. *J. Fluid Mech.* **194**, 15–44.
MOIN, P. & KIM, J. 1982 Numerical investigation of turbulent channel flow. *J. Fluid Mech.* **118**, 341–377.
PANTON, R.L. 2001 Overview of the self-sustaining mechanisms of wall turbulence. *Prog. Aerosp. Sci.* **37** (4), 341–383.
PASQUARIELLO, V., HICKEL, S. & ADAMS, N.A. 2017 Unsteady effects of strong shock-wave/boundary-layer interaction at high Reynolds number. *J. Fluid Mech.* **823**, 617–657.
PIROZZOLI, S. & BERNARDINI, M. 2011*a* Direct numerical simulation database for impinging shock wave/turbulent boundary-layer interaction. *AIAA J.* **49** (6), 1307–1312.
PIROZZOLI, S. & BERNARDINI, M. 2011*b*, Turbulence in supersonic boundary layers at moderate Reynolds number. *J. Fluid Mech.* **688**, 120–168.
PIROZZOLI, S., BERNARDINI, M. & GRASSO, F. 2010 Direct numerical simulation of transonic shock/boundary layer interaction under conditions of incipient separation. *J. Fluid Mech.* **657**, 361–393.
PIROZZOLI S. & GRASSO F. 2006 Direct numerical simulation of impinging shock wave/turbulent boundary layer interaction at M = 2.25. *Phys. Fluids* **18** (6), 065113.
PIROZZOLI, S., GRASSO, F. & GATSKI, T.B. 2004 Direct numerical simulation and analysis of a spatially evolving supersonic turbulent boundary layer at M = 2.25. *Phys. Fluids* **16** (3), 530–545.
PRIEBE, S., WU, M. & MARTÍN, M.P. 2009 Direct numerical simulation of a reflected-shock-wave/Turbulent-boundary-layer interaction. *AIAA J.* **47** (5), 1173–1185.
RAHGOZAR, S. & MACIEL, Y. 2012 Statistical analysis of low- and high-speed large-scale structures in the outer region of an adverse pressure gradient turbulent boundary layer. *J. Turbul.* **13**, N46.
RINGUETTE, M., WU, M. & MARTÍN, M.P. 2008 Low Reynolds number effects in a Mach 3 shock/Turbulent-boundary-layer interaction. *AIAA J.* **46** (7), 1883–1886.
ROBINSON, S.K. 1991 Coherent motions in the turbulent boundary layer. *Annu. Rev. Fluid Mech.* **23** (1991), 601–639.
SABNIS, K. & BABINSKY, H. 2023 A review of three-dimensional shock wave–boundary-layer interactions. *Prog. Aerosp. Sci.* **143**, 100953.
SCHOPPA, W. & HUSSAIN, F. 2002 Coherent structure generation in near-wall turbulence. *J. Fluid Mech.* **453**, 57–108.
SELIG, M.S., ANDREOPOULOS, J., MUCK, K.C., DUSSAUGE, J.P. & SMITS, A.J. 1989 Turbulence structure in a shock wave/turbulent boundary-layer interaction. *AIAA J.* **27** (7), 862–869.
SHI J. & YAN H. 2023 Turbulence amplification in the shock wave/turbulent boundary layer interaction over compression ramp by the flux reconstruction method. *Phys. Fluids* **35** (1), 016122.

https://doi.org/10.1017/jfm.2025.10616 Published online by Cambridge University Press

SKOTE, M. & HENNINGSON, D.S. 2002 Direct numerical simulation of a separated turbulent boundary layer. *J. Fluid Mech.* **471**, 107–136.

SMITS, A.J. & MUCK, K.-C. 1987 Experimental study of three shock wave/turbulent boundary layer interactions. *J. Fluid Mech.* **182**, 291–314.

TONG F., DONG S., LAI J., YUAN X. & LI X. 2022*a* Wall shear stress and wall heat flux in a supersonic turbulent boundary layer. *Phys. Fluids* **34** (1), 015127.

TONG F., LAI J., DUAN J., DONG S., YUAN X. & LI X. 2022*b* Effect of interaction strength on recovery downstream of incident shock interactions. *Phys. Fluids* **34** (12), 125127.

TONG, F., YU, C., TANG, Z. & LI, X. 2017 Numerical studies of shock wave interactions with a supersonic turbulent boundary layer in compression corner: turning angle effects. *Comput. Fluids* **149**, 56–69.

TONG F., YUAN X., LAI J., DUAN J., SUN D. & DONG S. 2022*c* Wall heat flux in a supersonic shock wave/turbulent boundary layer interaction. *Phys. Fluids* **34** (6), 065104.

VYAS, M.A., YODER, D.A. & GAITONDE, D.V. 2019 Reynolds-stress budgets in an impinging shock-wave/Boundary-layer interaction. *AIAA J.* **57** (11), 4698–4714.

WU, G., WANG, Z., SHI, T., ZHANG, Z., JIANG, W., QUAN, F. & CHANG, J. 2024 Effect of expansion waves on cowl shock wave and boundary layer interaction in hypersonic inlet. *Propul. Power Res.* **13** (1), 80–97.

WU, M. & MARTIN, M.P. 2007 Direct numerical simulation of supersonic turbulent boundary layer over a compression ramp. *AIAA J.* **45** (4), 879–889.

WU X. & MOIN P. 2010 Transitional and turbulent boundary layer with heat transfer. *Phys. Fluids* **22** (8), 085105.

XIANG, G., WANG, C., TENG, H. & JIANG, Z. 2018 Shock/shock interactions between bodies and wings. *Chinese J. Aeronaut.* **31** (2), 255–261.

YU, M., DONG, S.W., LIU, P.X., TANG, Z.G., YUAN, X.X. & XU, C.X. 2023 Post-shock turbulence recovery in oblique-shock/turbulent boundary layer interaction flows. *J. Fluid Mech.* **961**, A26.

YU, M., ZHAO, M.X., TANG, Z.G., YUAN, X.X. & XU, C.X. 2022 A spectral inspection for turbulence amplification in oblique shock wave/turbulent boundary layer interaction. *J. Fluid Mech.* **951**, A2.

ZHANG, X., JIANG, Z., QIN, X., QU, F. & YAN, C. 2024 A finite difference scale-adaptive TENO scheme for turbulence simulations. *J. Comput. Phys.* **502**, 112793.

ZHU, X.-K., YU, C.-P., TONG, F.-L. & LI, X.-L. 2016 Numerical study on wall temperature effects on shock wave/Turbulent boundary-layer interaction. *AIAA J.* **55** (1), 131–140.

ZUO, F.-Y. & PIROZZOLI, S. 2024 Recent progress in conical shock wave/boundary layer interaction with spanwise pressure gradient. *Propul. Power Res.* **13** (3), 295–318.

https://doi.org/10.1017/jfm.2025.10616 Published online by Cambridge University Press